博士論文（要約）

Stimuli-responsive mesoporous membranes using block copolymer

(ブロックコポリマーを用いた刺激応答性メゾポーラス膜)

唐 彦春

Content

1. Introduction

1.1 Background and motivation

Membrane technology had been dramatically developed after the membrane first commercialized for water purification in 1930s. Nowadays, membranes are not only provided to solve the problems of water scarcity and energy shortage, but also supported medical application like hemodialysis, drug delivery, microfluidics, micro-analysis and reactions. Among them, the stimuli-responsive membranes which can change their chemical, physical and barrier properties by responding to the environmental conditions have attracted large attention and shown tremendous development in last two decades. Multiple types of stimuli were applied to induce responses, including the direct stimulants such as temperature, pH, specific ions, and newly emerged remote triggers such as light, electric and magnetic fields.

However, preparing stimuli-responsive membranes with nano-scale pore size is still in challenge. The common stimuli-responsive membrane preparation methods are separated into post-modification and pre-modification approaches depending on the time for introducing stimuli-responsive gates into the membrane substrate. In the post-modification approach, stimuli-responsive polymers are usually immobilized on commercial membrane substrate by "grafting to" and "grafting form" methods. But with those methods, the diffusion of polymer chain or monomers is strongly inhibited by narrow membrane pore size, especially for those smaller than 100 nm, leading to inhomogeneous grafting and pore plugging.[1, 2] The pre-modification approach uses stimuli-responsive copolymers or micro-gels as additives of blend during membrane formation. Almost all the pre-modification type membrane are fabricated using the nonsolvent induced phase separation (NIPS) method. While, those membranes typically have a rather pore size broad distribution, which obviously limited their application. Moreover, instead of the NIPS, it is quite rare to see the pre-modification type membranes prepared via other method.

1.2 Scope of the research

In this study, we utilized a completely new method to develop three kinds of pre-modification type stimuli-responsive mesoporous membranes. Those membranes not only have excellent and unique stimuli-responsivities but also are with narrow size distribution. The detail information of those three types of membranes, like the preparation processes and filtration properties, will be described in three chapters respectively.

The first type is **thermo-responsive mesoporous block copolymer membrane** prepared by introducing nanopores into poly(oligoethylene glycol methyl ether methacrylate)-b-polystyrene-b-poly(oligoethylene glycol methyl ether methacrylate) ($PMEO_nMA$-*b*-PS-*b*-$PMEO_nMA$) templates via selective swelling the

$PMEO_nMA$ domains. The membrane with PS being the mechanical stable part of the matrix and thermo-responsive $PMEO_nMA$ covered the mesopores interiors. The lower critical solution temperature (LCST) of $PMEO_nMA$ is tunable by changing the average number of ethylene glycol repeating units in the side group, *n*, thus providing the membrane a tuning the thermos-responsivity.[3]

The second type is **magneto-responsive mesoporous block copolymer membrane** constructed by embedding iron oxide nanoparticles (IONPs) as local heaters into the PS matrix of the foresaid porous block copolymer membrane. The swollen/shrunken state of $PMEO_nMA$ brushes on the pore walls were triggered by the heat generated by the nearby IONPs within alternate magnetic field (AMF), leading to adjustable molecular sieving performance of the membrane.[4]

The third type is **uncoupled thermo- and pH-responsive mesoporous block copolymer membrane** fabricated with poly(N,N-dimethylaminoethyl methacrylate)-*b*- poly(diethyleneglycol methyl ether methacrylate)-*b*-polystyrene (PDMAEMA-*b*-$PMEO_2MA$-*b*-PS) using selective swelling PDMAEMA-b-$PMEO_2MA$ domains. $PMEO_2MA$ has LCST at 26 °C. PDMAEMA is a typical weak polyelectrolyte with pK_a value at 7.0-7.5 and also a thermo-responsive polymer revealed a LCST of 20-80 °C in aqueous solution. With combination of the properties of $PMEO_2MA$ and PDMAEMA, such membrane pore size can be varied into 4 different barrier dimension as function of the combination of temperature and pH.

2. Theory and literature review

2.1. Stimuli-responsive polymers

Stimuli-responsive polymers are capable of chemical and/or physical property change on receiving an external stimulus.[5-8] The typical stimuli include the direct stimulants such as temperature, pH, mechanical force,[9] specific ions and molecules, and newly emerged remote triggers such as light, electric and magnetic fields.[10, 11] The responses are also manifold, including dissolution/precipitation, degradation, drug release, and changes in hydration state, swelling/collapsing, hydrophobic/hydrophilic surface, conformation and micellisation (Figure 2.1).[12] Among all the stimuli, the temperature and pH are most important and predominantly studied. In this section, I will focus on displaying the theory and recent development of thermo-responsive and pH-responsive polymers.

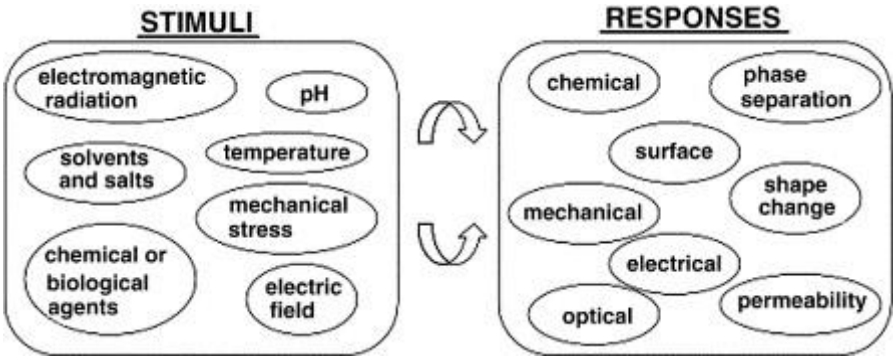

Figure 2.1. Stimuli and responses of stimuli-responsive polymers.[12]

2.1.1 Thermo-responsive polymer

2.1.1.1 Upper and lower critical solution temperature

Mixture is a system consisted of different chemical species. In a homogeneous mixture, all components are uniform and intermixed in molecular scale, for example, a polymer in a good solvent. A heterogeneous mixture has several phases with regions of different compositions, for instants, the oil and water mixture.

An ideal mixture is with no difference in interaction energy between components. An ideal mixture is always homogeneous because the free energy of mixing per site of it is purely entropic and the mixing entropy always being positive. Consider the binary ideal mixture of component A and B (A and B can be solvent molecules, monomers or large molecules) which have N_A and N_B molecules respectively. $\varphi_A=\varphi$ denote the volume fraction of component A and $\varphi_B=1-\varphi$ is the corresponding volume fraction of component B. The free energy of mixing component A and B is shown as following equation:

$$\Delta F_{mix} = -T\Delta S_{mix} = kT\left[\frac{\phi}{N_A} In\phi + \frac{1-\phi}{N_B} In(1-\phi)\right] \quad (2.1)$$

ΔF_{mix} is always negative as a result of always positive ΔS_{mix}.

When we take the interaction energy (U) between components into account, the free energy of mixing per lattice site is written as:

$$\Delta F_{mix} = \Delta U_{mix} - T\Delta S_{mix} = kT\left[\frac{\phi}{N_A} In\phi + \frac{1-\phi}{N_B} In(1-\phi) + \chi\phi(1-\phi)\right] \quad (2.2)$$

In where, χ is the flory interaction parameter defined as the difference of interaction energies of each chemical species. Equation (2.2) was first calculated by Huggins and later independently derived by Flory, so it is commonly referred as the Flory-Huggins equation. For polymer solution, $N_A = N$ and $N_B = 1$, therefore the Flory-Huggins equation for polymer solutions is:

$$\Delta F_{mix} = \Delta U_{mix} - T\Delta S_{mix} = kT\left[\frac{\phi}{N} In\phi + (1-\phi) In(1-\phi) + \chi\phi(1-\phi)\right] \quad (2.3)$$

Flory-Huggins theory assumes that there is no volume change with mixing. However, in most real polymer mixture, the volume changes. Because of the local packing effects, the Flory interaction parameter (χ) is with a temperature-dependent additive constant and often written as the sum of two terms empirically:

$$\chi(\mathrm{T}) \cong \mathrm{A} + {}^{B}/_{T} \quad (2.4)$$

Term A is the 'entropic part' of χ, and B/T is referred to the 'enthalpic part'. In practice, the local packing effects are not fully understood. All deviations from the lattice model are lumped into χ which displays dependences on composition, chain length, and temperature.

The local stability of a homogeneous mixture of composition ϕ_0 with free energy $F_{mix}(\phi_0)$ is determined by whether the $F_{mix}(\phi_0)$ is higher or lower than that of a phase separated state $F_{\alpha\beta}(\phi_0)$. Figure 2.2 is the free energy versus composition profile. When $F_{mix}(\phi_0) > F_{\alpha\beta}(\phi_0)$, as shown in Figure 2.2a, the system can lower its free energy by phase separating into two phases. While, when $F_{mix}(\phi_0) < F_{\alpha\beta}(\phi_0)$ (Figure 2.2b), the mixed state is locally stable. The criterion for local stability is written in terms of the second derivative of the free energy:

$$\frac{\partial^2 F_{mix}}{\partial^2 \phi^2} < 0 \quad unstable,$$

$$\frac{\partial^2 F_{mix}}{\partial^2 \phi^2} > 0 \quad stable$$

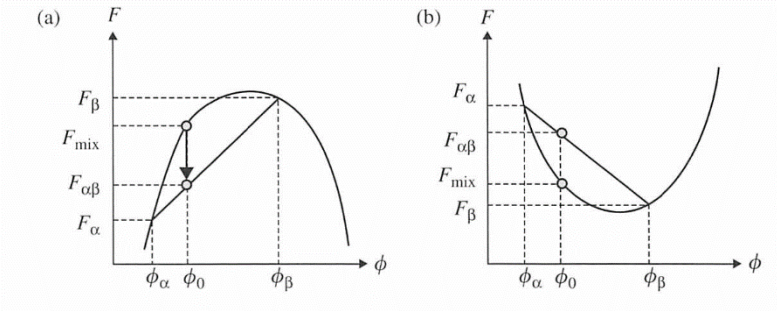

Figure 2.2. Composition dependence of free energy, with examples of system that are (a) unstable and (b) locally stable.[13]

A phase diagram can be constructed to summarize the temperature dependent phase behavior of the mixture, showing stability, instability, and meta-stability regions (Figure 2.3). The binodal (solid line in the phase diagram, Figure 2.3) is the interaction parameter corresponding to the phase boundary, which can be obtained by solving following equation:

$$\left(\frac{\partial \Delta F_{mix}}{\partial \phi}\right)_{\emptyset=\emptyset'} = \left(\frac{\partial \Delta F_{mix}}{\partial \phi}\right)_{\emptyset=\emptyset''} = kT\left[\frac{In\phi}{N} - \frac{In(1-\phi)}{N} - \chi(1-2\phi)\right] = 0 \qquad (2.5)$$

The spinodal curve (the dashed line in the bottom part of Figure 2.3) is the boundary between unstable and metastable regions.[13] Because of the temperature dependence of χ (see Equation 2.4), the phase diagram also can be transformed into temperature and composition profile. When the χ of a polymer blend linearly increases with 1/T (B > 0), the increasing temperature in this blend leads to increased miscibility (Figure 2.4). The highest temperature of the two-phase region is the upper critical solution temperature (UCST), and a large number of polymer blends exhibit this UCST behavior. On the other hand, as shown in Figure 2.5, the increasing temperature leads to an increase of the χ (B <0), and hence lower the miscibility of blend. The lowest temperature of the two-phase region is the lower critical solution temperature (LCST).[14] Note that, only the minimum and maximum points of the binodal/spinodal in the phase diagram are LSCT and UCST points, respectively, any other point along the respective curve is referred to as a cloud point (T_{cp}) or a demixing (T_{dem}) point.[15]

When consider the polymers in aqueous solution, the interactions between polymers and water became stronger and more complex other than the sample van der Waals interactions in organic environment. The polar groups in the polymer can interact with water by dipole-dipole interactions and hyderogen bonding (enthalpy) thereby avoiding the strong hydrophobic interactions in water (entropy).[16] But using Flory-Huggins equation (Equation 2.3), the experimental data still can be fairly accurate fitted. Thermo-responsive polymers are separated into LCST-type (undergoing a demixing phase transition upon heating)

and UCST-type (undergoing a demixing phase transition upon cooling) based on the phase separation occurred above or below a specific temperature. The solvent plays an important role in the solution behavior for a thermo-responsive polymer. One thermo-responsive polymer can exhibit LCST behavior in one solvent and UCST behavior in another. For example, the poly(N-isopropyl acrylamide) (PNIPAM) shows LCST behavior in water but display UCST behavior in water/alcohol binary solvent.[16-18] Thermo-responsive polymers are almost applied in an aqueous solvent environment.[19]

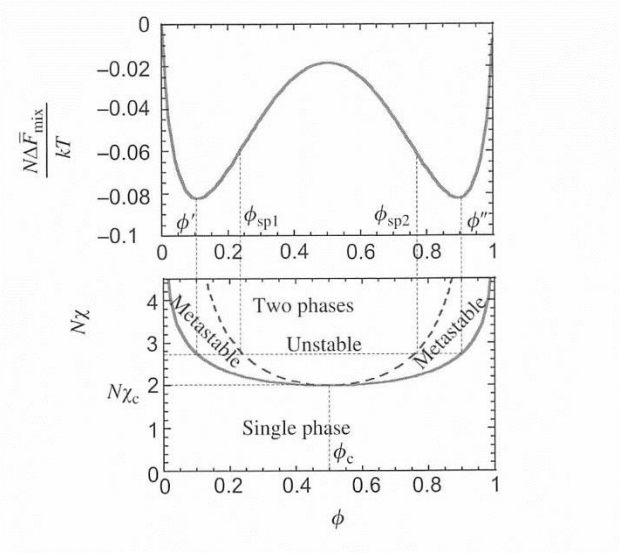

Figure 2.3. Free energy of a symmetric polymer blend (χN=2.1, top figure) and the corresponding phase diagram (bottom). The solid curve is binodal and dashed curve is spinodal.[13]

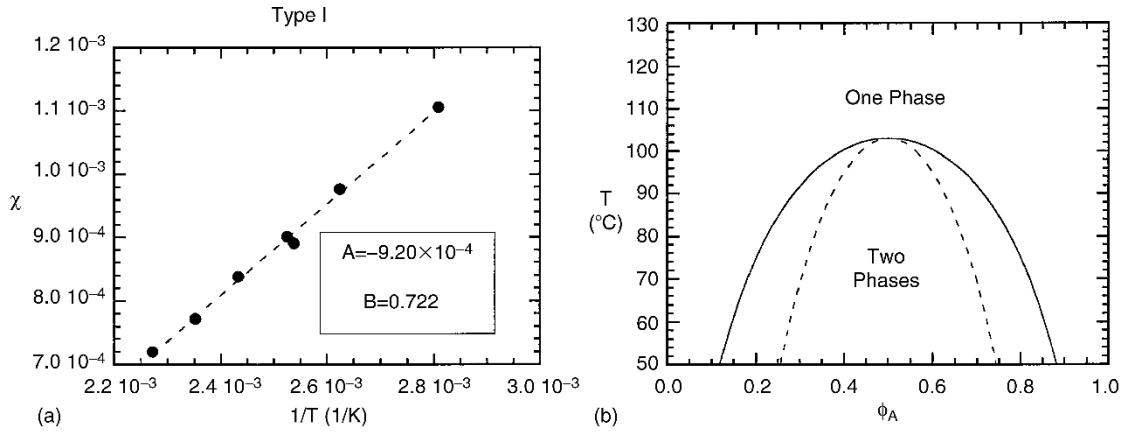

Figure 2.4. Temperature dependence of χ (a) and phase diagram (b) of the hydrogenated polybutadiene (88% vinyl) and deuterated polybutadiene (78% vinyl) blend .[14]

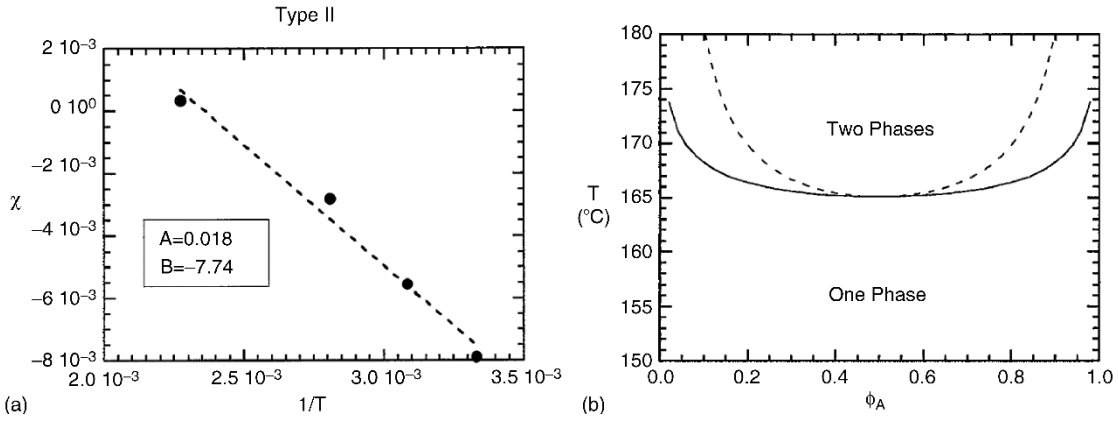

Figure 2.5. Temperature dependence of χ (a) and phase diagram (b) of the hydrogenated polyisobutylene and deuterated head-to-head polypropylene blend.[14]

2.1.1.2 LCST-type thermo-responsive polymers

LCST-type thermo-responsive polymers exhibit a phase transition from a clear to a cloudy state as the environment temperature increases about LCST. The common characteristic of temperature-responsive polymers is the presence of hydrophilic part together with hydrophobic groups, like methyl, ethyl and propyl groups, as show in Figure 2.6-2.9.[8] The discontinuous transition of thermo-responsive polymer can be mainly attributed to hydrogen bonds and hydrophobic interactions. A small change of the balance between those two interactions is responsible for the interconversion of polymers between two different phases. In the case of aqueous solution, hydrogen bonds between hydrophilic groups of thermo-responsive polymer and already somewhat arranged water molecules convert the polymer chains in specific orientations. Accompanying with exothermic enthalpy of hydrogen bonds, the water molecules structured around the nonpolar regions of polymers cause hydrophobic effect resulting in a decreased entropy upon mixing (negative ΔS). At low temperatures, the strong hydrogen bonding outweighs the unfavorable free energy related to the exposure of hydrophobic groups to water, leading to good solubility of the polymer in water. As the temperature rises, the attractive forces weaken upon heating, entropy term dominates the otherwise exothermic enthalpy of the hydrogen bonds which is the initial driving force for dissolution.[20]

The most famous and intensively studied thermo-responsive polymers are PNIPAM and its derivatives. PNIPAM has a LCST in the range of 30-35 °C which is very close to the human physiological temperature, therefore PNIPAM products have been found very promising for pulsatile drug delivery.[6, 7, 21, 22] By copolymerizing NIPAM and a second monomers, the shifting hydrophilic/hydrophobic balance can decrease/increase the LCST of PNIPAM.[23-25] Further, the LCST also can be turned by replacing the isopropyl group by a carboxyl group, an amide group or a hydroxyl group.[24, 26-28]

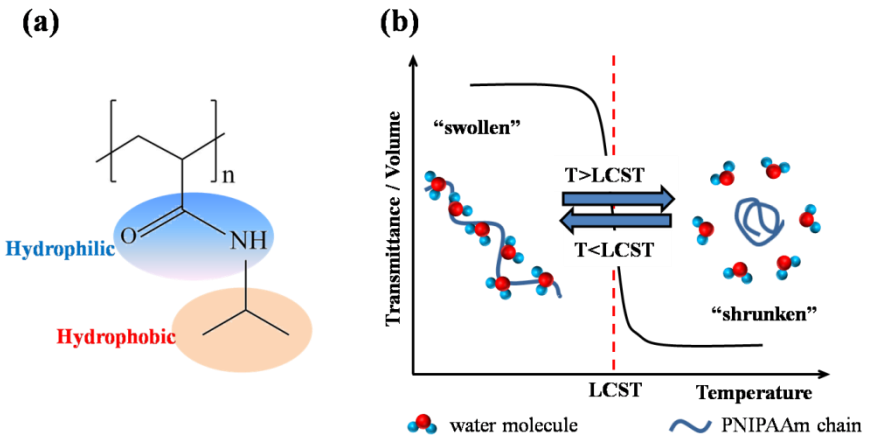

Figure 2.6. (a) Chemical structure of PNIPAM and (b) temperature dependent swelling/deswelling transition.[29]

The thermo-responsive polyamides (namely poly(2-oxazoline)s, polypeptoids and polypeptides, Figure 2.7) is other thermo-responsive polymer family which is intensively studied for the developing drug delivery system.[12, 30, 31] They are synthesized by living cationic ring-opening polymerization of the 2-oxazolines or the corresponding amino acid N-carboxyanhydrides.[31-33] The main chains consisting of the repeating amide groups are hydrophilic. The hydrophilic-hydrophobic balance of could be tuned by introducing hydrophobic side chains to obtain thermo-responsive. For example, poly(2-ethyl-2-oxazoline) (PEtOx) has a concentration-dependent cloud point in 61-64 °C, poly(2-isopropyl-2-oxazoline) (PiPrOx) has a cloud point in the range of 36-39 °C, poly(2-n-propyl-2-oxazoline) (PnPrOx) also exhibits thermo-responsivity in water with a cloud point in 25 °C (Figure 2.8).[34-36]

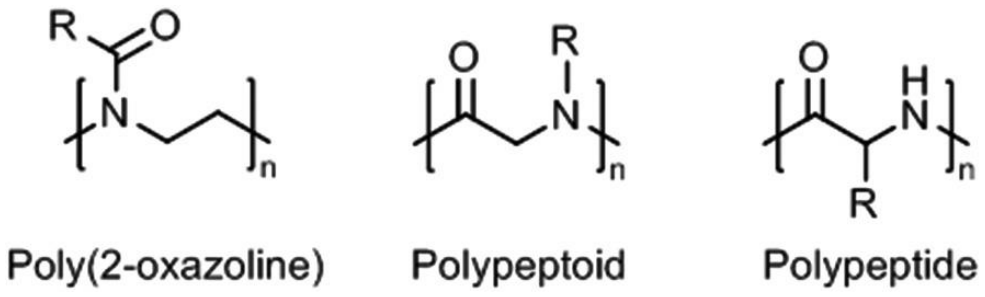

Figure 2.7. General chemical structures of (partially) main-chain polyamides: poly(2-oxazoline), polypeptoid, and polypeptide; R = organic substituent (usually alkyl).[31]

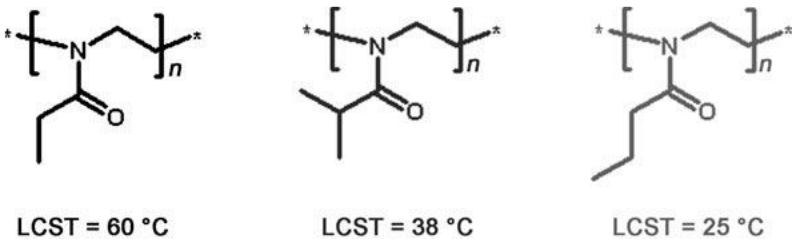

Figure 2.8. PEtOx (left), PiPrOx (middle), and PnPrOx (right) with their corresponding LCST values.[37]

PEG (polyethylene glycol)-based (co)polymers (Figure 2.9) are recently emerged thermo-responsive polymers that can compete with or even surpass PNIPAM. These polymers are easily accessible via polymerization of oligo ethylene glycol macro-monomers that consist of an oligo ethylene glycol chain with a polymerizable group, e.g., acrylate, methacrylate or styrene, and a methylether, ethyl ether or hydroxy-group. The most common type of backbone are methacrylates and acrylates (Figure 2.9). Ether of them can by polymerized by the three popular controlled radical polymerization (CRP) methods, only the nitroxide mediated polymerization (NMP) of the oligo ethylene glycol methacrylates is not possible without adding small amount of styrenic comonomers.[38-40] The thermoresponsive oligo(ethylene glycol)-based polymers have wonderful bio-compatibility and a wide range of LCST, from 5 to 94 ^{O}C, obtained by carefully control of the hydrophilic/hydrophobic balance of the polymers. Increasing hydrophilicity of the polymer will increase the LCST, because of the enthalpic. On the other hand, increasing hydrophobicity will decrease the LCST.[41-48] Ishizone group have used living anionic polymerizations to synthesize a serious oligo(ethylene glycol) methacrylate homopolymers and copolymers. [44, 49, 50] They found both side chain length and ω-alkyl group of side chain would affect the LCST of polymer. Further, the LCST also could finely tuned by copolymerizing two oligo(ethylene glycol) methacrylates with different side chain length, for example, the di(ethylene glycol) methyl ether methacrylate (ME2MA) (80 mol%) and tri(ethylene glycol) methyl ether methacrylate (ME3MA) (20 mol%) random copolymer shown a cloud point in 37 °C (Figure 2.10).[50] Lutz et al. have intensively studied on the synthesis and the physicochemical properties of thermoresponsive oligo(ethylene glycol)-based polymers. In 2006, they synthesized the random copolymers of 2-(2-methoxyethoxy)ethyl methacrylate (MEO_2MA) and oligo(ethylene glycol) methacrylate (OEGMA, Mn = 475 g,mol-1) by atom transfer radical polymerization (ATRP). By precisely adjusting the comonomers composition, the LCST was finely tuned from 28 to 90 °C. By comparing with PNIPAM which is the "gold standard" of thermo-responsive polymers, they found that the oligo(ethylene glycol)-based polymers have fewer hysteresis between cooling and heating curves, and have less infect from the polymer dispersity and concentration. Because the monomer structure is the main influencing factor, the difference of the LCST for a certain oligo(ethylene glycol)-based polymer caused by the molecular weight, polymer end group and polymer concentration have rarely been reported .[38, 42, 43, 46, 47, 51-55]

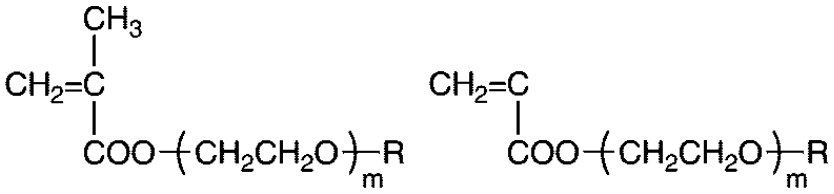

Figure 2.9. Molecular structures of oligo(ethylene glycol) methacrylates, R=Me or Et.

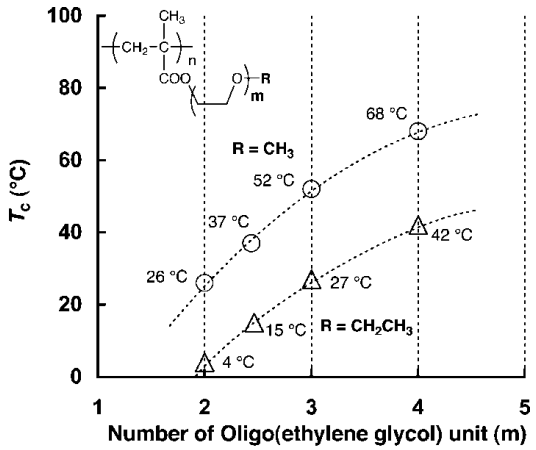

Figure 2.10. Cloud point changes as function of the number of oligo(ethylene glycol) unit (m). O and Δ represent the data of methyl and ethyl ethers, respectively.[50]

Other LCST-type thermo-responsive polymers include: (1) natural thermo-responsive polymers, like methyl cellulose has a LCST of 40 °C, hydroxypropyl cellulose has a LCST of 45 °C and hydroxypropyl cellulose has a LCST of 69 °C;[56] (2) Amphiphilic poly(asparagine) derivatives which are with controllable sol-gel-sol phase transition;[57, 58] (3) Poly(methyl vinyl ether) PMVE (LCST = 37 °C); (4) Poly(N-vinyl caprolactam) PVCa (LCST = 33 °C); (5) poly(N-vinylcaprolactam) (PVCL) (LCST = 32 °C).[12, 17]

2.1.1.3 UCST-type thermo-responsive polymers

Comparing the large number of LCST-type thermo-responsive polymers, there are a few of UCST-type thermo-responsive were developed. Figure 2.11 shows the poly(N-acryloyl glycinamide) (PNAGA) and poly(N,N'-dimethyl(methacryloylethyl)ammonium propanesulfonate) (PDMAPS) which are two typical UCST-type thermo-responsive polymers. The interactions from hydrogen bonds in non-ionic polymers or electrostatic bonds occurring in zwitterionic polymers make the UCST-type thermo-responsive polymers phase separate in aqueous solution. Upon dissolution of PNAGA in water, the hydrogen bonds between the carbonyl and amine groups are broken in an endothermic process and replaced by hydrogen bonds with water in an exothermic process. The UCSTs are highly depend on the concentration, molecular weight.[16]

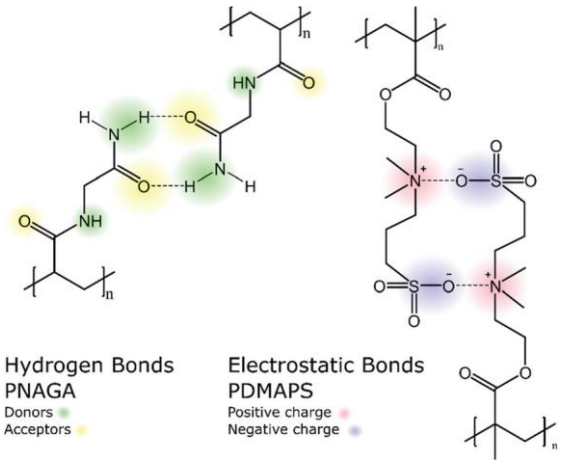

Figure 2.11. Schematic representation of hydrogen bonds of PNAGA (left) and electrostatic bonds of PDMAPS (right).[15]

2.1.2 pH-responsive polymers

The pH-responsive polymers are defined as polyelectrolytes that include in their structure weak basic or acidic groups that can accept or release protons in response to a change in the environmental pH.[59] The pH-responsive basic polymers contain basic groups like tertiary amine, morpholino, pyrrolidine, imidazole, piperazine and pyridine groups, as shown in Figure 2.12.

These basic groups accept protons at low pH by forming polyelectrolytes and release them at high pH, leading to the transition of ionic to non-ionic pH-responsive basic polymers (Figure 2.14, bottom). This transition, which usually occurred in pH 7-11, makes polymer chains stretch at low pH and collapse at high pH in aqueous solution.[60] Poly(N,N-dimethylaminoethyl methacrylate) (PDMAEMA or PDMA) which has applied for the design of gene-delivery system and biomedical surface modification is the most popular weak basic polymer (pKa = 7.0-7.5). PDMAEMA exhibits LCST behavior in water and combination of LCST and UCST behavior in the presence of small quantities of trivalent counter ions. The LCST of PDMAEMA reported in the literatures is range from 20 to 80 ^{O}C. It is varied with molecular weight (especially in basic solution) and increases with decreasing of pH (increasing degree of charge), mainly due to the backbone/carbonyl interactions. The LCST also can be tuned by copolymerizing DMAEMA wuth a second hydrophobic/hydrophilic monomors.[61-66]

The pH-responsive acidic polymers have acidic groups like carboxylic, sulfonic acid, phosphoric acid and boronic acid groups (Figure 2.13). They also accept protons at low pH and release them at high pH, but the polyelectrolytes are formed at acidic condition. Therefore, the pH-responsive acidic polymers are collapsed in acidic or neutral solution and stretched in basic condition. Among the pH-responsive acidic

polymers, poly(acrylic acide) (PAAc) and poly(methacrylic acid) (PMAAc) have been most frequently reported, because of the easy polymerization method.

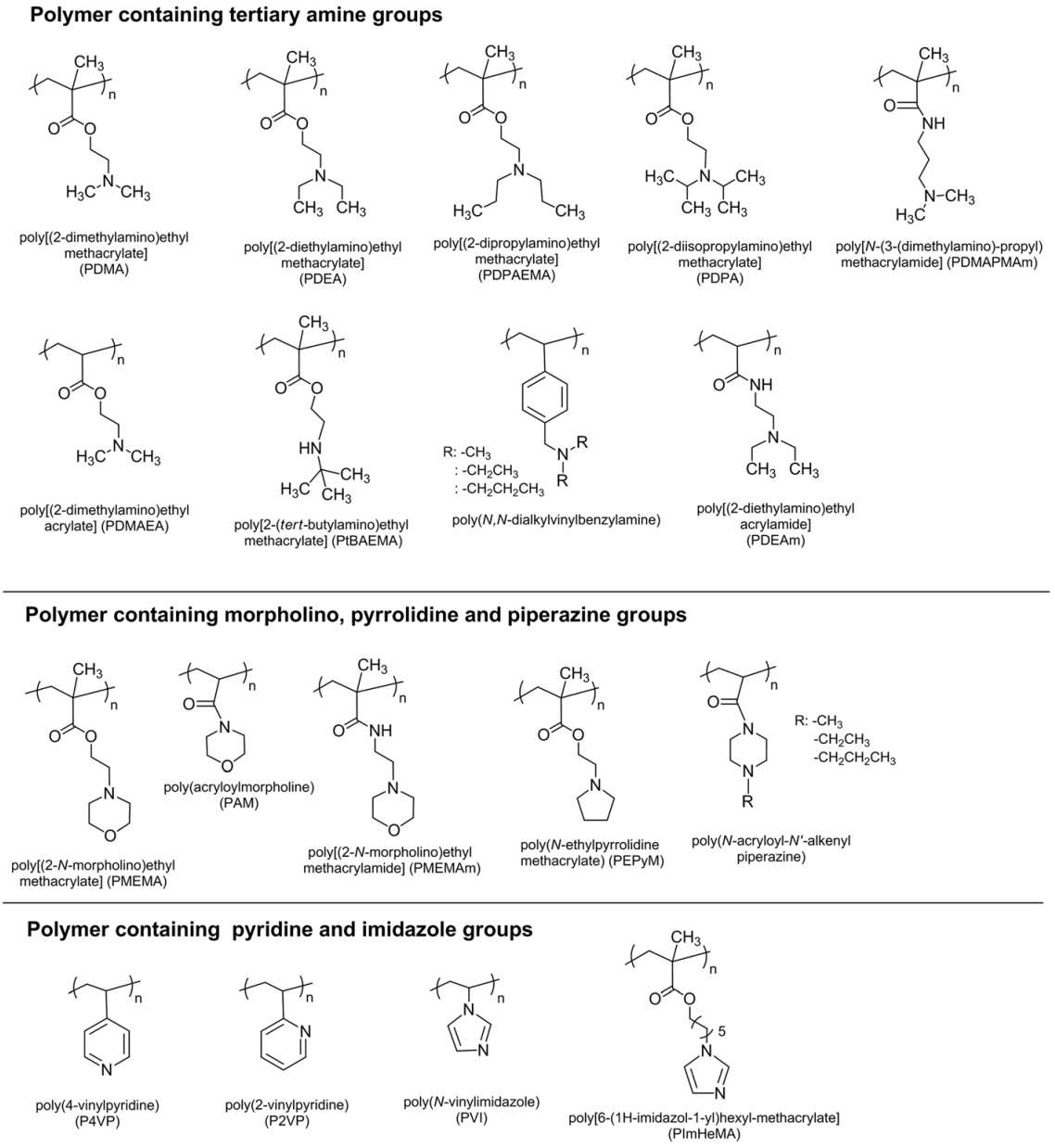

Figure 2.12. Chemical structures of typical pH-responsive basic polymers.[59]

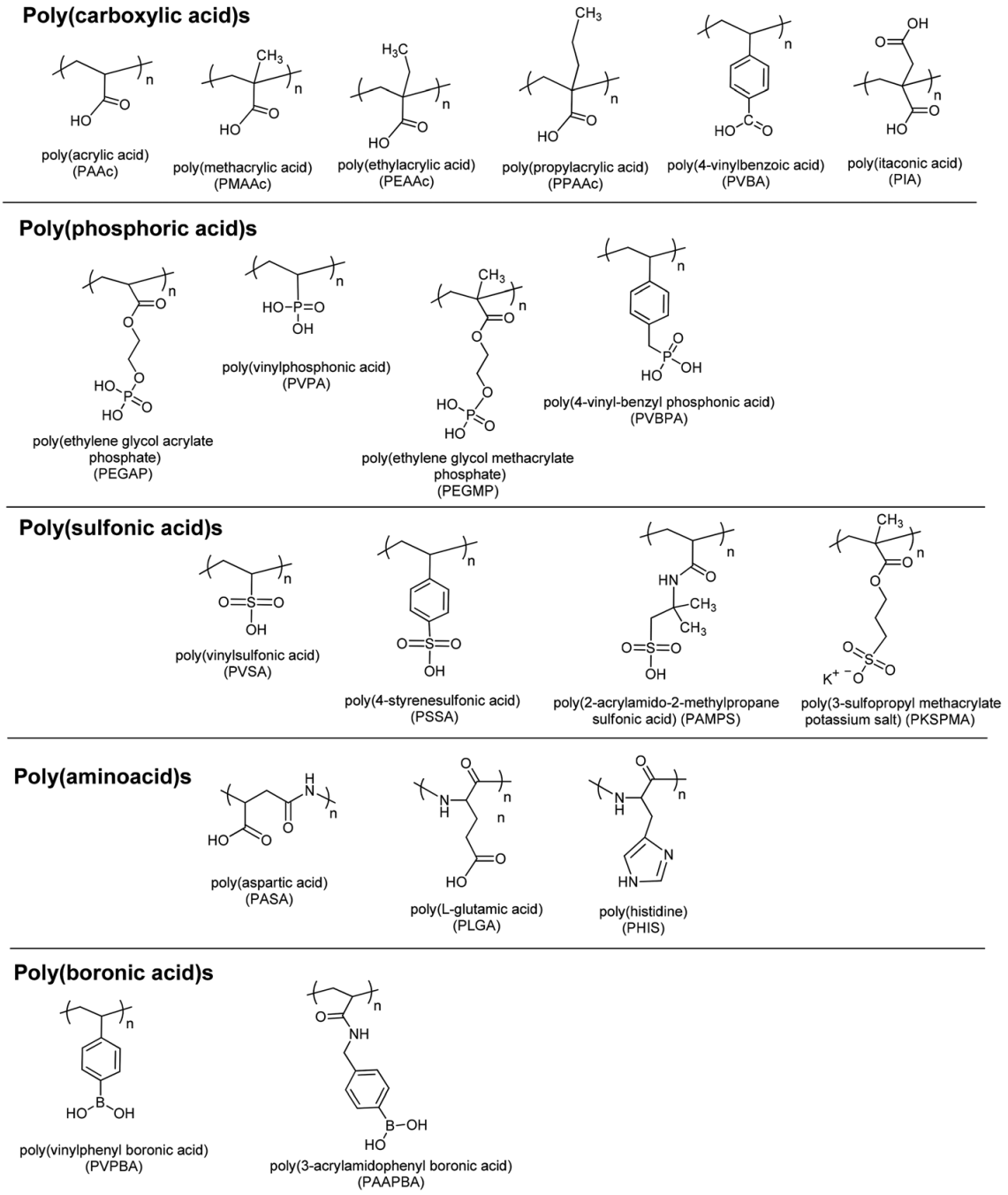

Figure 2.13. Chemical structures of typical pH-responsive acidic polymers.[59]

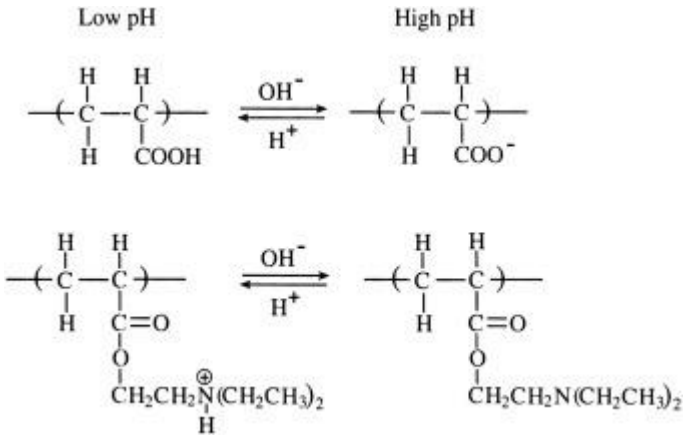

Figure 2.14. The ionic/non-ionic transition of typical acidic (Poly(acrylic acid), top) and basic (poly(N,N-dimethylaminoethyl methacrylate), bottom) polyelectrolytes. [8]

2.2 Block copolymers

Block copolymers (BCPs) are macromolecules composed of two or more polymeric chains (blocks) of chemically distinct repeat units.[67] Various architectures of block copolymer (Figure 2.15) are all possible to be synthesized by controllable/living polymerization, in connection with suitable purification method for all the employed reagents (monomers, initiators, solvents, additives and so on. Take the synthesis of simplest AB-type block copolymers as example, two synthesis strategies were taken: (1) sequential addition of monomers; and (2) coupling of two appropriately end-functional chains. Among those two methods, the former one is much more common to be used. To successfully achieve well-defined block copolymers, two considerations should be taken: (1) the order of monomers addition, the first block must be able to efficiently initiate the polymerization of the monomers of second block; (2) the quantitative conversion of the first monomers.[68]

The common used living polymerization for block copolymer synthesis are anionic polymerization, cationic polymerization and reversible deactivation radial polymerization (RDRP).[69] The RDRP method will be described in detail in Section 2.4.

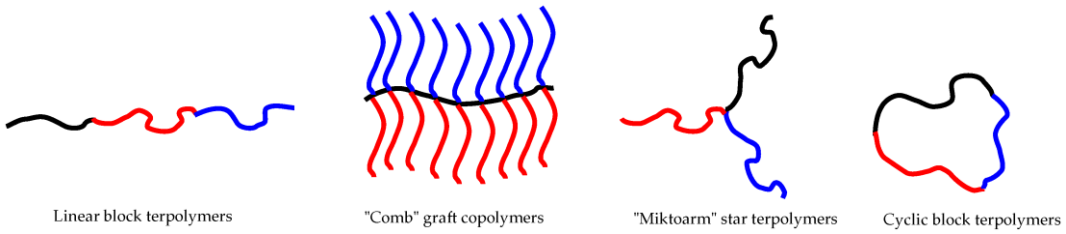

Figure 2.15. Schematic illustration of several types of block copolymer architectures.[70]

The most remarkable property of block copolymers is their self-assemble ability in the melt into a variety of ordered structure with nanoscale periodicities. In the melt, the repulsion of the immiscible components of block copolymers drives a phase separation, whilst the existence of the chemical links between the blocks prevent the complete separation. The block copolymer chains organize to put the different portions on the opposite sides of an interface. To avoid the over-stretching of the blocks, the separation is limited in nanoscale [71].

According to the mean-field theory (MFT), the phase separation behavior of block copolymer is dictated by Flory–Huggins theory (Equation 2.2) and governed by three experimental controllable factors: the copolymer degree of polymerization (N), the composition of copolymer (φ) and the block-block interaction parameter (χ). The first two factors which influence the translational and configurational entropy can be regulated by polymerization stoichiometry. χ contains a significant enthalpic contribution and is determined by the incompatibility of each block and has the temperature dependence, as given by

$$\chi_{AB}(\mathrm{T}) \cong \frac{Z}{k_B T} \cdot \left[\varepsilon_{AB} - \frac{(\varepsilon_{AA} + \varepsilon_{BB})}{2} \right] \tag{2.6}$$

where ε_{AB} is the interaction energy between monomer units of A and B blocks of a AB-type diblock copolymer, ε_{AA} and ε_{BB} are interaction energy of A and B monomers themselves, respectively. Z is the number of nearest neighbor monomers to a copolymer configuration cell. A positive χ_{AB} shows repulsion of the A and B monomers, and a negative χ_{AB} indicates the mixing tendency of those two kind of monomers.[69]

In general, at high temperature, the block chains are mixed homogeneously. On the lowing temperature, the energy parameter χ is increased, blocks of copolymer with sufficient large N tend to segregate and process microphase separation. The transition from a homogenous melt of chains to a heterogeneous melt of ordered microphase-separated domains is called the order-disorder transition (ODT),[72] as shown in Figure 2.16.

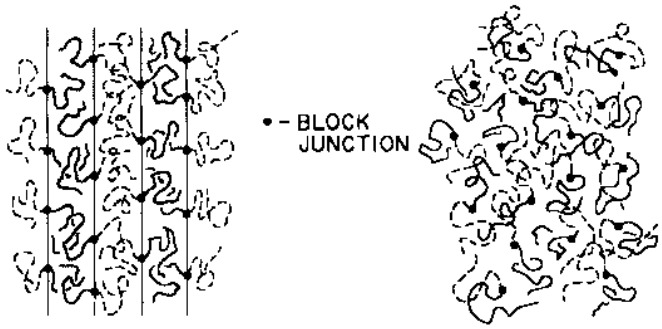

Figure 2.16. Schematic representation of order-disorder transition [73].

According to the self-consistent mean field theory (SCFT), the structure of a AB-type diblock copolymer is predictable with a given χ_{AB}, N, f and segment length. Figure 2.17 shows the phase diagram for a conformational-symmetric copolymer calculated using SCFT and proven experimentally. The ODT occurs at a critical value of $\chi_{AB}N$, depending on the composition of the copolymer (φ_A or f_A). Symmetric diblock copolymers are predicted to disorder when $\chi_{AB}N < (\chi_{AB}N)_{ODT}$, where $(\chi_{AB}N)_{ODT}$ = 10.5. When $\chi_{AB}N > 10.5$, they form a lamellar phase, with alternating layers of the constituent blocks. As composition, f_A, varies further from 0.5, the following sequence of phases can be obtained: a bicontinuous cubic "gyroid" phase, a hexagonal-packed cylinders and a body-centered cubic phase. The size and periodicity of the nanodomains are also affected by the N and χ_{AB}. [74]

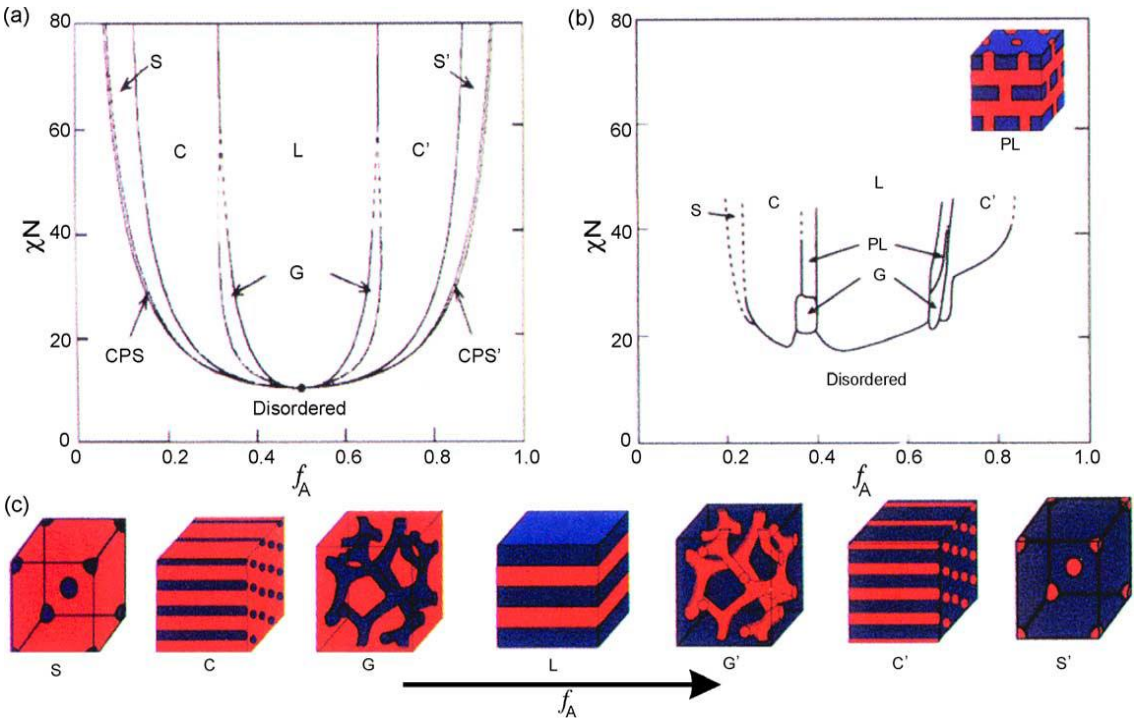

Figure 2.17. Diblock copolymers are predicted to self-assemble according to a phase diagram predicted by self-consistent mean field theory (a) and proven experimentally (b). A variety of constant-radius geometries are observed as a function of relative lengths of the two blocks (c). [71]

2.3. Stimuli-responsive membranes

Membrane technology had been dramatically developed after the membrane first commercialized for water purification in 1930s and play paramount roles in myriad fields. The membranes are not only provided to solve the problems of water scarcity and energy shortage, but also supported medical application like hemodialysis, drug delivery, microfluidics, micro-analysis and reactions. However, the traditional

membranes have inert physical/chemical structure and pore to fouling, which restrict their efficient application and do not satisfy the requirements in real life.[12, 75-89] Therefore, stimuli-responsive membranes were developed, they can change their chemical, physical and barrier properties by responding to the changes in external stimuli, including the direct stimulants such as temperature, pH, and specific ions[3, 90-94], and newly emerged remote triggers such as light and electric and magnetic fields.[95-98] They have highly potential for various applications. The drug delivery is able to be realized based on the controllable molecular release from capsule membranes. The physical/chemical structure change can play an important role in water purification and biomolecular separation. Moreover, stimuli-responsive membranes are expected to overcome the membrane fouling which is one of the major issues hounding the long-term stability performance of membrane. [79, 87, 89, 94, 99, 100]

Membranes can be divided into organic (polymer) and inorganic membranes based on membrane materials; and also into non-porous and porous membrane. The porous membranes were further separated into reverse osmosis, nanofiltration, ultrafiltration, and microfiltration membranes (Figure 2.18). Among them, ultrafiltration membranes play an important role, they have average pore diameter in the 1-100 nm range and are used for separation, concentration and removal of macromolecules (e.g. proteins, plasmid DNA and endotoxin) particles (e.g. bacterial and viruses). The separation mechanism ultrafiltration membranes is based on size exclusion, e.i. solutes larger than the membrane pore size are rejected and those smaller than the membrane pore size can pass through the pore structure.[101-103] Although in the past decades, stimuli-responsive membrane have attracted a large attention and developed dramatically, there are a few achievements for the stimuli-responsive membranes in ultrafiltration range. This section briefly reviews the polymer made ultrafiltration stimuli-responsive membranes, mainly focusing on the preparation procedures.

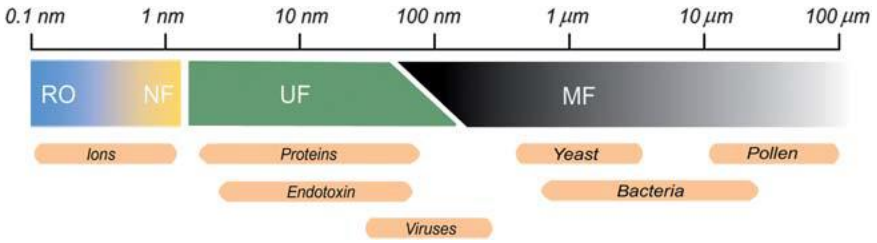

Figure 2.18. Classification of the porous membranes with the size range and targets for separation.[102]

2.3.1. Stimuli-responsive membrane preparation strategies

The essential strategy of stimuli-responsive membrane preparation is the incorporation of stimuli-responsive elements with porous membrane structure, allowing the stimuli-responsive elements work as functional gates for controlling the selective properties of membranes. The design and production practices are placed into two categories: (1) post-modification; introducing stimuli-responsive components into

existing membranes through surface modification methods; (2) *in-situ* modification; adding stimuli-responsive components during membranes fabrication processes.[1]

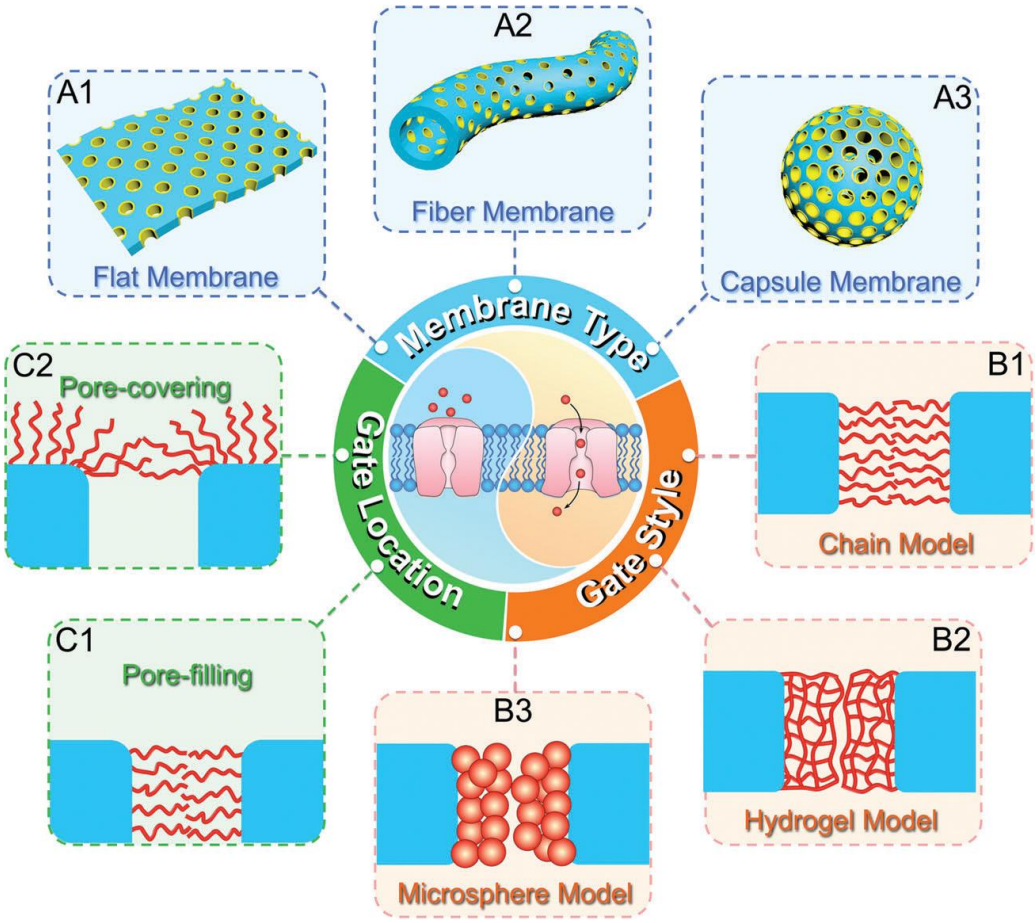

Figure 2.19. Stimuli-responsive membranes in different structures. There are three membrane shape (A1) flat sheet, (A2) hollow fiber, and (A3) hollow capsule. The stimuli-responsive functional gates can be (B1) linear brushes, (B2) hydrogel mesh, and (B3) micro- or nano-gels. The functional gate can be located in (C1) the interior of pores or (C2) membrane surface.[87]

2.3.1.1. Stimuli-responsive ultrafiltration membrane preparation by post-modification

The membrane post-modification is almost based on the surface grafting techniques, by which stimuli-responsive components are grafted on established membranes. People further classified this surface grafting techniques into “grafting to” and “grafting form” methods.

(1) "Grafting to" approach

In the "grafting to" approach, end-functionalized polymers react with functional groups on the surface of the membranes to form tethered polymer brushes. There are many stimuli-responsive membranes were fabricated using this approach with various functional groups either in polymers or membranes. For example, Park et al. prepared the thermo-responsive membranes through photo-immobilizing PNIPAM chains which were connected with photo-reactive azidophenyl groups into polycarbonate membranes (average pore diameter: 0.2 μm).[104] Tripathi et al. polymerized dopamine to modify a poly(ethylene terephthalate) (PET) microfiltration (MF) membranes (pore size: 0.3-0.4 μm), then utilized the free amine groups of polydopamine to "graft to" amino-terminated PNIPAM for achieving a thermo-responsive membrane (Figure 2.20).[105] Beside polymer brushes, stimuli-responsive microgels were also can be "grafted to" membranes.[106, 107]

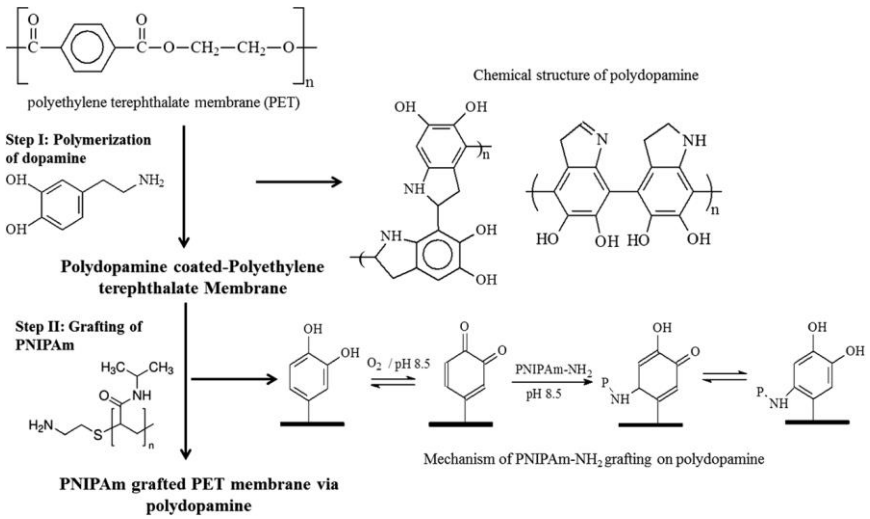

Figure 2.20. Schematic illustration of route to "graft to" PNIPAm chains on to PET membrane with polydopamine.[105]

The advantage of "grafting to" approach is that the used polymer is able to be controllably polymerized and characterized. However, with this approach, polymer chains must diffuse through the narrow pore walls and existing polymer layer to reach the reactive sites. The barriers effect becomes very big when the base membrane pore size is small and get even pronounced as the tethered polymer layer get thicker. The modified membranes usually have low grafting density and layer thickness.[2, 104-113] The inherent disadvantage of "grafting to" method restreet itself apply for the modification of the interior of ultrafiltration filtration membranes, there the reported "grafting to" stimuli-responsive ultrafiltration membranes were all prepared as pore-covering type , as shown in Figure 2.19C2.[114, 115] Because the functional polymer chains were immobilized on the membrane surface, the pore size of the original

membrane does not affected by the additional grafted chains. However, the very thin functional lay could not effectively control the selectivity.

(2) "Grafting from" approach

To circumvent the problem in "grafting to" method and have higher brush grafting density and layer thickness, people turned to use "grafting from" approach which is the best established method for stimuli-responsive membrane fabrication.

In "grafting form" approach, initiator precursors are first immobilized onto the membrane surface, followed by polymer growth with monomer addition to the immobilized initiator sites. Figure 2.21 shows a typical fabrication rout for a pH-responsive membrane via "grafting form" method. The amino groups were first introduced into poly(tetrafluoroethylene) (PTFE) membrane (pore size: 10 μm) with density determined by the power and time of the glow-discharge treatment. The amino groups worked as initiator and started the polymerization of g-benzyl l-glutamate N-carboxyanhydride to produce poly(γ-benzyl L-glutamate). After the grafted poly(γ-benzyl L-glutamate) chains were hydrolyzed into poly(glutamic acid) (PLG), a pH-responsive membrane was prepared.[116]

Different from the "grafting to" strategy, the properties of grafted layer, such as graft density, chain length, polydispersity, cross-linking or chemical functionality, are independent design parameters in "grafting form" method. This attractive advantage provides flexibility in the membrane design.[90, 114, 115, 117]

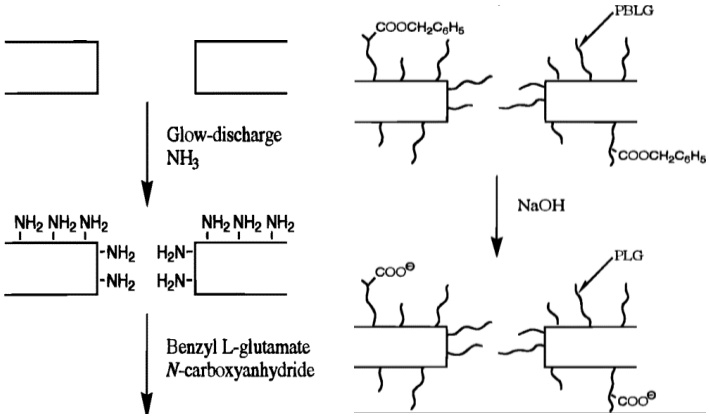

Figure 2.21. Schematic illustration of "grafting form" PLG brushes on a PTFE membrane.[116]

Although "grafting form" method allows for the precise tailoring of grafted layer by precise control of the reaction conditions, the steric hindrance from membrane pores for diffusion of monomers is still exist. Alem et al. gave a good example through growing PNIPAM brushes on 0.08 and 0.3 μm poly(ethylene terephthalate) (PET) membranes via atom transfer radical polymerization (ATRP). The confinement from

small size membrane pores strongly impacted the polymerization processes. The responsive barrier in small pores was located on the outer surface of the membrane with a grafted layer thickness larger than the pore dimension, while in larger pores, the grafted layer covered the entire membrane surface (Figure 2.22). The NIPAM monomers were hard to reach the pore walls of small pore membrane because of the rete-controlling barrier formed by the already grafted PNIPAM layer at the surface of the membrane. In the small pore case, temperature responsivity of prepared membranes were completely controlled by the outer surface layer and exhibited the "negative switching effect", i.e. a higher permeability at temperature below LCST.[118]

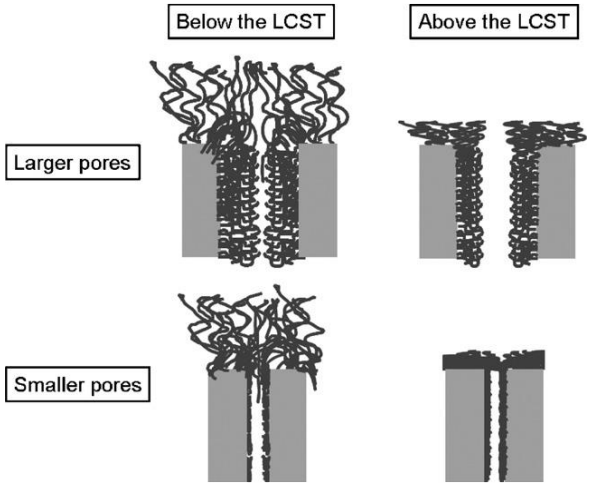

Figure 2.22. Schematic illustration of PNIPAM chains location with small and large pores via "grafting form" method.[118]

Later, a low number of stimuli-responsive ultrafiltration membranes with the "negative switching effect" were fabricated utilizing this heterogeneous "grafting form" polymers on membrane surface (Figure 2.23a). One example is the thermo-responsive membranes prepared by Hesampour et al. They "grafted form" PNIPAM on the anisotropic polysulfone ultrafiltration membranes by a free radical polymerization with persulfate-based reactive species as initiators.[119] Himstedt et al. prepared pH-responsive membranes through grafting form poly(acrylic acid) brushes on the surface of nanofiltration membrane via UV-assisted heterogeneous grafting polymerization.[120-122]

Figure 2.23. Schematic cross-section depiction of (a) membrane surface-functionalized, (b) pore surface-functionalized, and (c) hydrogel pore-filled membranes.

The stimuli-responsive membranes of pore surface-functionalized type (Figure 2.23b) are even harder to achieve. Until now, only two cases have been found. Forst et al. prepared temperature sensitive membranes by growing PNIPAM chains on Poly(ethylene terephthalate) track-etched ultrafiltration membranes (pore diameter: 0.11 μm) via surface initiated Atom Transfer Radical Polymerization(SI-ATRP). They controlled the grafting by slowing down the polymerization speed.[92] Using the same slow speed ATRP method, the same group grafted form diblock copolymers on the interior of ultrafiltration membrane pores and developed an ion and temperature responsive membrane.[123]

The publications regarded to controlled modification of ultrafiltration membrane (the two membrane types shown in Figure 2.23a and b) are rarely found. It is because of the high requirements on the polymerization technique on "grafting from" stimuli-responsive polymers on membrane with size smaller than 100 nm. An uncontrolled modification easily results in pore plugging and loss of a highly desirable barrier switching property.[92]

Other strategy to prepare ultrafiltration stimuli-responsive membranes is to fill stimuli-responsive hydrogels into commercial membrane pores (Figure 2.23c), in which hydrogels serve as sieving medium; the established membrane provides mechanical stability and confines the hydrogel within its pores.[91, 124, 125] Figure 2.24 shows a typical preparation process for a thermo-responsive pore-filling membrane. Polyethylene terephthalate (PET) track-etched membranes with pore diameters between 200 and 5000 nm were pre-modified by pre-adsorption of photo-initiators to provide anchoring sites. Then the membrane pores were filled by PNIPAM hydrogel by in-situ cross-linking polymerization. The selectivity of this membrane is defined by the hydrogel mesh size which could be tuned by changing monomer concentration and cross-linker proportion. This pore filling functionalization method were also utilized for preparing magneto-responsive membrane by trapping magnetic nanoparticles in the hydrogel network.[125] Usually those hydrogel pore-filling membranes are suffering from the relative week mechanical property, but recently it has reported that the hydrogel filled membrane has stable separation performance up to 4 bar.[91] The absolute permeabilities of the hydrogel pore-filling membranes are lower than other type membrane with comparable pore size, because of the larger barrier thickness and lower porosity.

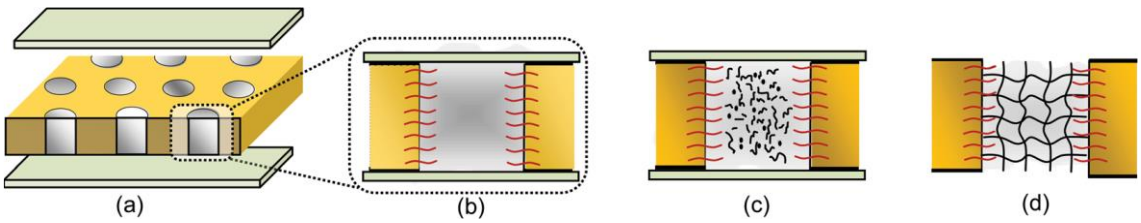

Figure 2.24. Schematic illustration of pore-filling functionalization by photo-polymerization. (a) shows the membrane were filled with reaction mixture and sealed with two glass plates on top and bottom sides. (b–d) are cross-section view membrane pore exhibiting "grafting form" procedures during equilibration with

reaction mixture (b), during UV initiated in situ crosslinking polymerization (c), and after complete reaction toward hydrogel pore-filled composite membrane (d).[91]

2.3.1.2. Stimuli-responsive ultrafiltration membrane preparation by in-situ modification

The in-situ modification method is to render membrane using stimuli-responsive copolymers or micro-gels as additives of blend during the membrane formation.

(1) Nonsolvent induced phase separation (NIPS) approach

Until now, nearly all the stimuli-responsive ultrafiltration membranes are prepared using nonsolvent induced phase separation (NIPS) strategy which is one of the most critical breakthrough in membrane field.[96, 108, 126-140] Those membranes prepared by NIPS characterized by asymmetric structure with a very thin, dense nano-/micro-porous top layer as selective layer and a thick macro-voided sublayer as supporting layer (Figure 2.25). As shown in Figure 2.26, the NIPS membrane preparation method can be easily handled with two steps: first, cast a polymer solution prepared by dissolving polymer with additives in a good solvent on a flat substrate; second, quickly move the casted film into nonsolvent bath (usually water) to induce pores. In the nonsolvent bath, the polymer solution phase separate from a non-phase region into polymer-rich and polymer-poor phases (Figure 2.27). Because the different accessibility of different location of polymer solutions of casted film, the asymmetric porous structure like it shown in Figure 2.25 can be obtained after the precipitation process.

Using NIPS strategy, many stimuli-responsive ultrafiltration membranes were constructed using pure stimuli-responsive block copolymers, like polystyrene-b-poly(4-vinylpyridine) (PS-b-P4VP),[127, 132, 133] poly(N-isopropylacrylamide)-b-polycaprolactone-b- poly(N-isopropylacrylamide) (PNIPAM-b-PCL-b-PNIPAM),[128] poly(styrene-co-isoprene)-b-poly(N, N-dimethylaminoethyl methacrylate) (P(S-co-I)-b-PDMAEMA),[141] and polystyrene-poly(N-isopropylacrylamide) (PS-PNIPAM).[137]

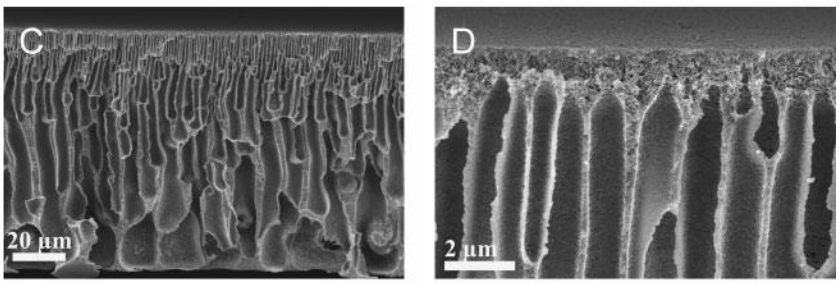

Figure 2.25. SEM images of the cross-sectional view of the membrane prepared by NIPS.[130]

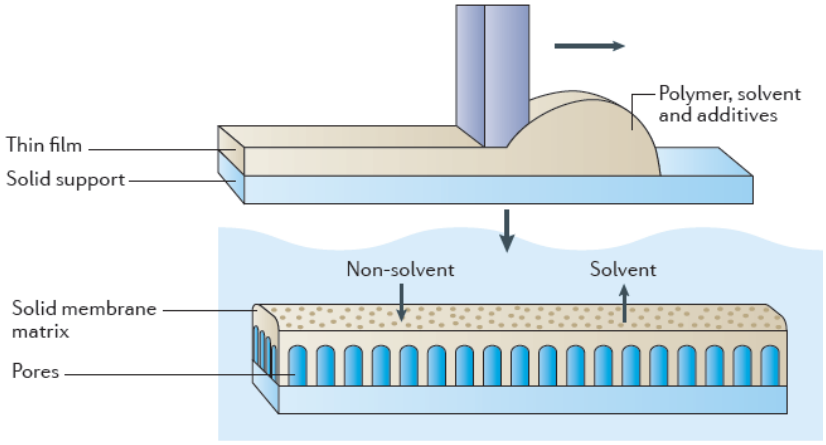

Figure 2.26. Schematic illustration of membrane formation by NIPS.[76]

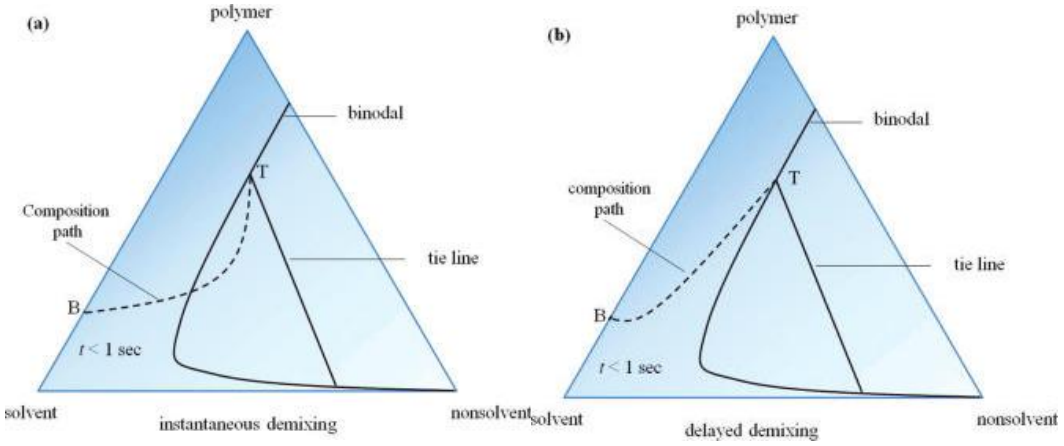

Figure 2.27. Composition paths of membrane preparation via NIPS with (a) instantaneous demixing and (b) delayed demixing; T represents the top layer and B is the bottom layer of the film.[142, 143]

The NIPS-type stimuli-responsive ultrafiltration membranes are more offen developed using blends of homo-polymers and stimuli-responsive copolymers as additives. Lou et al. fabricated pH-responsive poly(ether sulfone) (PES) composite membranes blended with amphiphilic polystyrene-block-poly(acrylic acid) (PS-b-PAA) diblock copolymers via NIPS (Figure 2.28). The membranes with ultrafiltration scale pore size, exhibit pH-responsive permeability and size selectivity.[134] There are many other homo-polymer/additive combinations, for instance, Polyethersulfone (PES) with additive poly(vinylpyrrolidone) (PVP);[131] polyacrylonitrile (PAN) with additive poly(acrylonitrile-graft-isopropylacrylamide) (PAN-g-PNIPAM);[144] and polysulfone (PSf) with additive polysulfone-graft-(poly(isopropylacrylamide-co-acrylic acid)-random-poly(methyl acrylate)) (PSf-g-(P(NIPAAm-coAA)-r-PMMA)).[139]

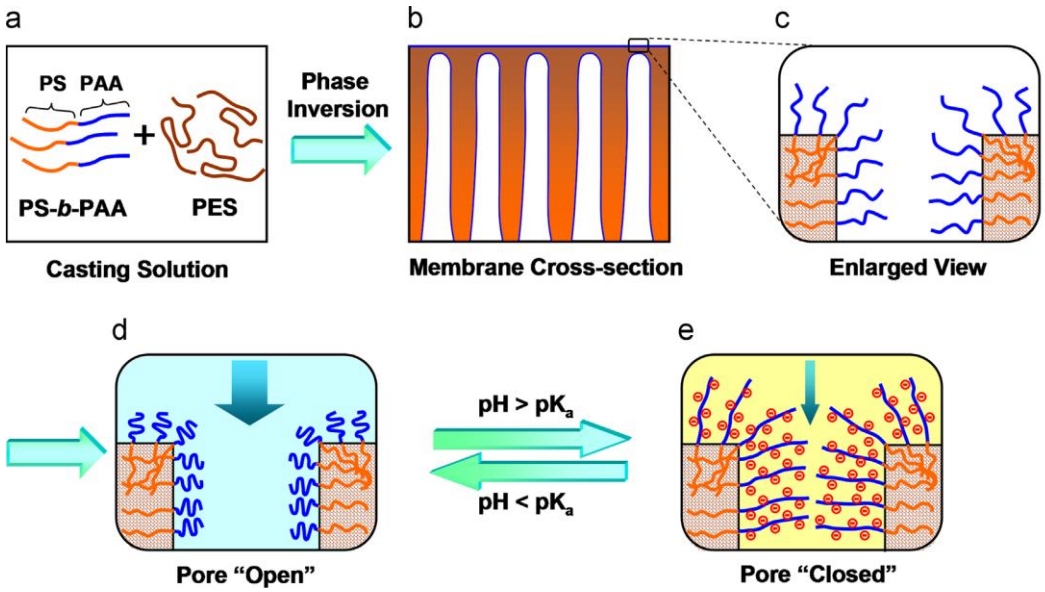

Figure 2.28. Schematic illustration of membrane fabrication processes and pH-responsivity. PS-b-PAA block copolymers are blended with PES homopolymers (a) to fabricate membrane (b) with PES as matrix and PAA brushes on membrane pore surface (c). The PAA chains on the membrane pore surfaces shrink at pH < pKa and thus "open" membrane pores (d), and stretch at pH > pKa and thus closed membrane pores (e).[134]

The membrane blends with stimuli-responsive micro-/nano-gels as additive are also utilized to fabricate stimuli-responsive ultrafiltration membranes.[96, 129, 135, 136, 138, 145] One example is a magneto-responsive ultrafiltration membrane prepared with blend of PES, PNIPAM nanogels and magnetic nanoparticles (Figure 2.29). The membranes were with ultrafiltration scale pores and with changeable molecular weight cutoff (MWCO) controlled by alternating magnetic field (AMF).[136]

The NIPS is a relative easy method and have widely studied for stimuli-responsive ultrafiltration membranes development, but the membranes prepared by NIPS typically have a rather broad pore size distribution in the barrier layer, as shown in Figure 2.30. This drawback limits efficiency of their applications.

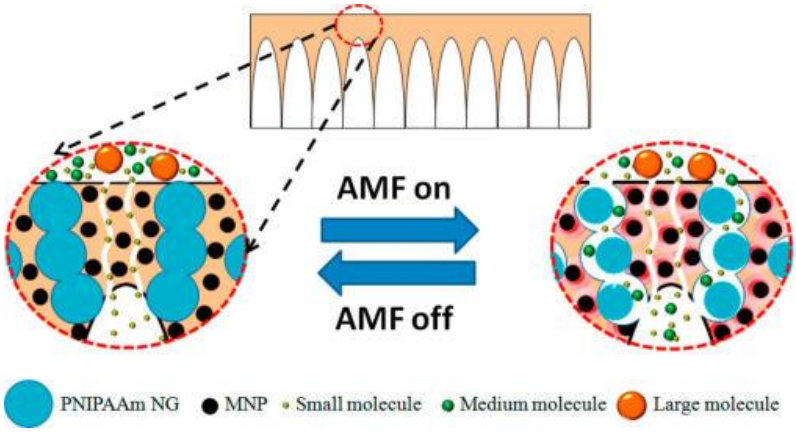

Figure 2.29. Schematic illustration of magneto-responsive ultrafiltration membrane prepared with PES, iron oxide and hydrogel mixture via NIPS. Heat generated by nearby nano-heaters triggered size transasion of PNIPAM nano-gel immobilized in PES macropores by remote-control alternating magnetic field (AMF).[136]

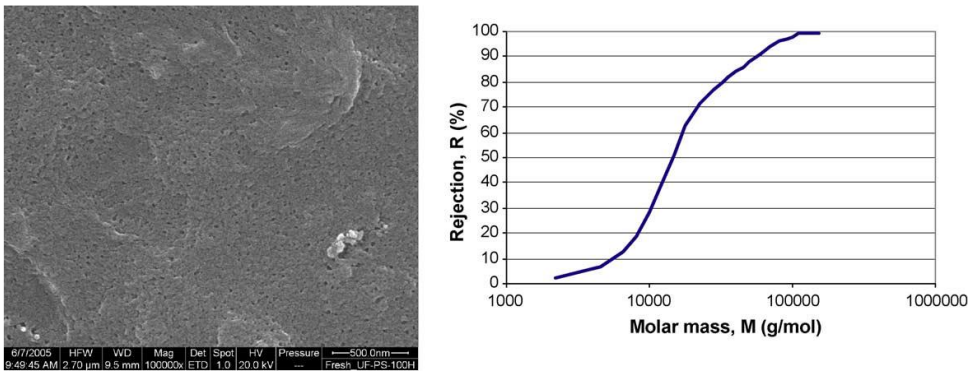

Figure 2.30. SEM image of the outer surface of a commercial polysulfone-based ultrafiltration membrane prepared by NIPS (left), and its separation curve analyzed with a dextran mixture.[103]

(2) Swelling-induced pore-making approach

Another in-situ modification strategy is to introduce mesopores into self-assembled block copolymer templates by selective swelling method. The swelling-induced pore-making approach which starts from block copolymer with the pore-forming mechanism bases on a physical phenomenon without any chemical reactions. Exposing the self-assembled BCPs in a solvent which have selective affinity with one block (let it be **A** block) leads to swelling of the domains composed of **A** blocks. The swelling which leads to excluded-volume force exerted on the non-swelling matrix of, for example, **B** block results in plastic deformation of **B** scaffold to dissipate the stress. Upon evaporation of the solvent, the mesopores form in place of the swollen domains because the swollen **A** blocks undergo entropic relaxation while the **B** domains fixate the reconstructed morphology. Therefore, the pore walls of obtained porous materials are

covered by **A** block chains. Since, by using this method, there is no mass loss in BCP materials, the robustness reduction and secondary contamination are successfully avoided.[146, 147] Wong and coworkers developed pH-responsive ultrafiltration membranes made from polystyrene-*b*-poly-(2-vinylpyridine) (PS-*b*-P2VP) by swelling introduce pore-making method. The reconstruction process of PS-*b*-P2VP nanorods was influenced by swelling temperature, BCP architecture and swelling agent.[93]

Based on the same pore-forming mechanism, many more combinations of BCPs and swelling conditions have been explored to induce the pore forming morphology reconstruction. Zhang et al. reported that PS-*b*-P2VP films of 150nm original thickness can be turned into nanoporous films by tactfully treating them in mixtures of methanol and supercritical carbon dioxide ($scCO_2$), where the compressed CO_2 was used as plasticizer to enhance the methanol swelling of P2VP domains. Because of the gas-like diffusion property of $scCO_2$ fluids, the transport of methanol to PS-*b*-P2VP films was accelerated. The swelling was facilitated without increasing the temperature. But, unfortunately, these porous films have not developed into membranes.[148] This thesis is focus on stimuli-responsive ultrafiltration membranes fabricated using this methanol-$scCO_2$ selective swelling method

2.4 Reversible addition-fragmentation chain transfer (RAFT) polymerization for stimuli-responsive polymers

Reversible deactivation radial polymerization (RDRP) is a powerful tool for polymer synthesis. It can control over the polymerization process and then provide relative an easy access to functional polymers with targeted molar mass, narrow polydispersity and versatile molecular architectures, like block copolymers, gradient copolymers, grafting and star polymers. The essence of a RDRP process is the reversible activation-deactivation equilibrium of propagating polymer radicals. This equilibrium is established by reversible termination of propagating chain or degeneration chain transfer (Figure 2.31).[149]

There are three most popular RDRPs: nitroxide mediated polymerization (NMP), atom transfer radical polymerization (ATRP), and reversible addition-fragmentation chain transfer (RAFT). For the stimuli-responsive polymer synthesis, RAFT has advantages over other two, for its tolerance of a wide range of functionalities in monomer, RAFT agent and the polymerization medium.[150] The RAFT was first developed in 1998, and then this technique has been intensively studied. Graeme Moad, Ezio Rizzardo and San H. Thang have given an in-depth review on how to conduct RAFT and choose RAFT agents to achieve particular structures.[151, 152] San H. Thang et al. reviews the design and synthesis of RAFT agent.[153] And then Keddie, D. J. and Graeme Moad reported guides for block copolymer and stimuli-responsive polymer synthesis, respectively.[149, 150] This section only briefly provides the mechanism of RAFT and block copolymer synthesis within RAFT.

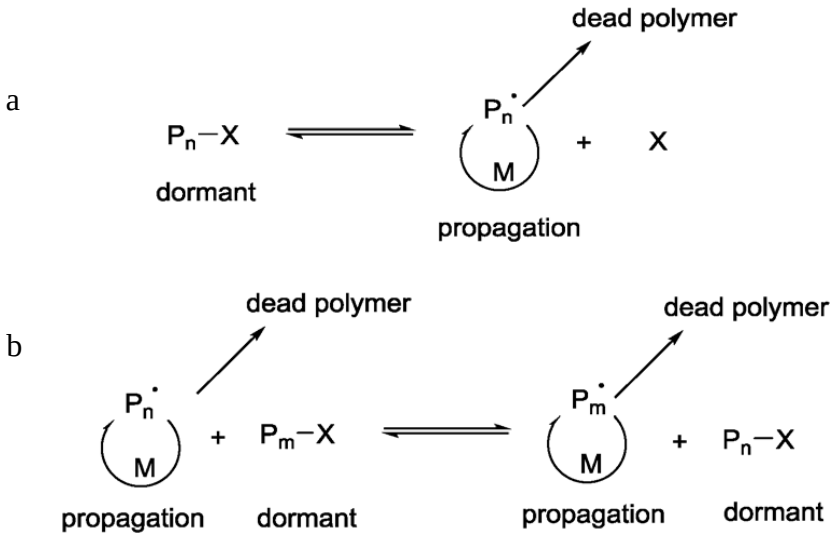

Figure 2.31. Schematic illustration of reversible-deactivation radical polymerization by (a) reversible termination and (b) degenerative chain transfer.[149]

2.4.1. Mechanism of RAFT polymerization

The feature of mechanism of RAFT polymerization is shown in Figure 2.32. As a traditional radical polymerization, RAFT polymerization also begins with initiation. An initiator derived radical (I·) propagates with monomer (M) giving a propagating radical ($P_n^{\cdot}$). Then the $P_n^{\cdot}$ reacts with the thiocarbonylthio compound **1** to form an intermediate radical **3**. The intermediate radical **3** quickly fragments to a polymeric thiocarbonylthio compound **2** and a new radical (R·) which can react with monomer to form a new propagating radical ($P_m^{\cdot}$). The pre-equilibrium can be finished rapidly in a well-controlled RAFT polymerization. Then system moves into the main equilibrium between the propagating radicals ($P_n^{\cdot}$ and $P_m^{\cdot}$) and the dormant polymeric thiocarbonylthio compound **4**. $P_n^{\cdot}$ and $P_m^{\cdot}$ have equal probability to extend with monomers (M) in this equilibrium, therefore the polymer product is able to have a narrow polydispersity. The RAFT process does not prevent the formation of dead polymer, but with an extreme low concentration. Most of stimuli-responsive polymers would be synthesized by RAFT polymerization and their monomers are almost 'more-activated' monomers.[149, 151-155]

RAFT agent is the most important part in a RAFT reaction and an inappropriate RAFT agent will lead the polymerization out of control. There are several rules to choose a suitable RAFT agent for a polymerization: (1) the RAFT agents **1** and **2** should have a reactive double bond; (2) the intermediate radicals **3** are prone to fragment to products rapidly and do no side reactions; (3) the radial R· can effectively re-initiate polymerization.[151]

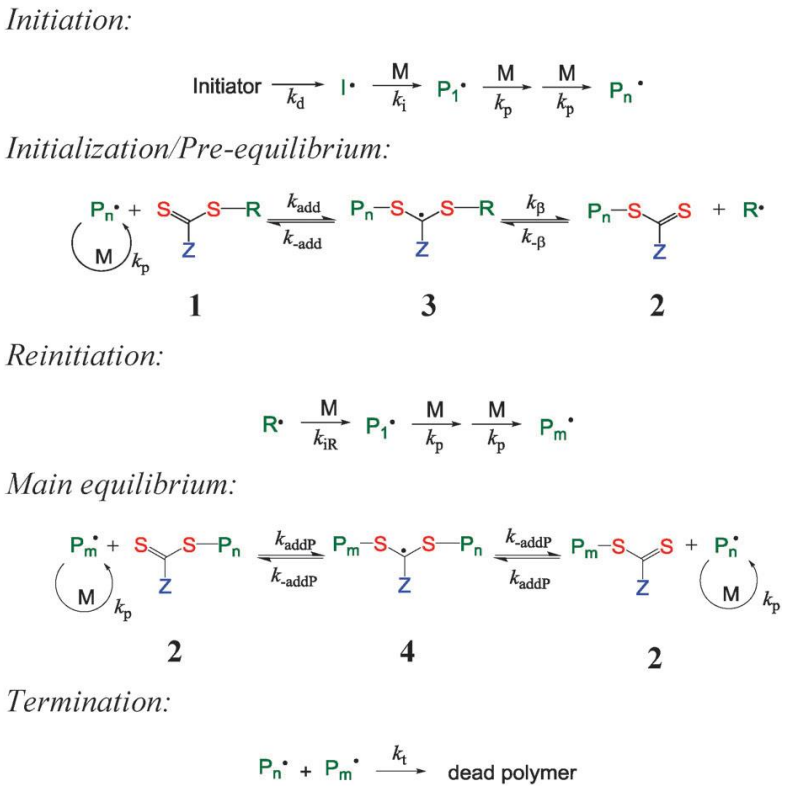

Figure 2.32. Mechanism of reversible-addition fragmentation chain transfer (RAFT) polymerization.[149]

The effectiveness of a RAFT agent is determined by the activating group Z and hemolytic leaving group R. Group Z strongly influences the rate of addition and fragmentation of radicals in the main equilibrium (Figure 2.32). Figure 2.33 shows guidelines for the Z group selection of RAFT agents. Group R should be both a good leaving group with is equal or better than the propagating radicals and a good initiating radical. The guidelines for the G group selection of RAFT agents is shown in Figure 2.34.

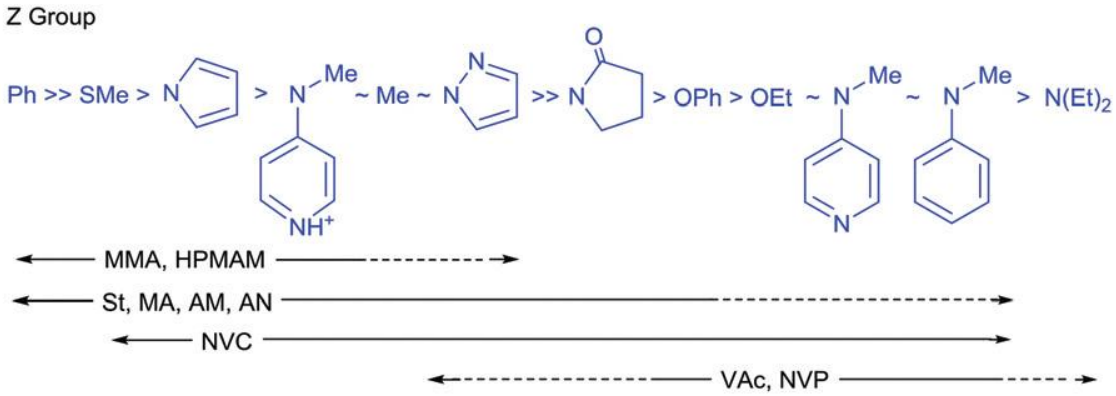

Figure 2.33. Guidelines for the Z group selection of RAFT agents. RAFT agent addition rates and transfer constants decrease and fragmentation rates increase from left to right. A dashed line means limited control

(e.g., retardation and/or high polydispersity).[150] MMA is methyl methacrylate, HPMAM is N-(2-hydroxypropyl) methacrylamide, St is styrene, DMAm is N,N-dimethylacrylamide, VAc is vinyl acetate, NVP is N-vinylpyrrolidone.

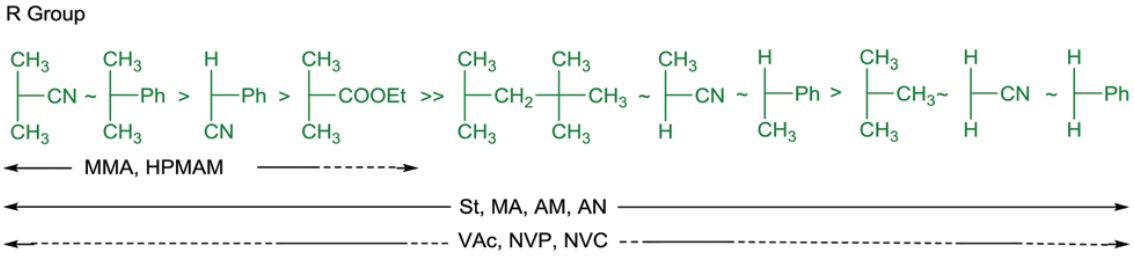

Figure 2.34. Guidelines for the R group selection of RAFT agents. Fragmentation rates decrease from left to right. A dashed line means limited control (e.g., retardation and/or high polydispersity).[150] MMA is methyl methacrylate, HPMAM is N-(2-hydroxypropyl) methacrylamide, St is styrene, DMAm is N,N-dimethylacrylamide, VAc is vinyl acetate, NVP is N-vinylpyrrolidone.

2.4.2. Block copolymer synthesis

Most of the polymer chains in the product synthesized with RAFT retain the thiocarbonylthio end group. They can work as micro-RAFT agents and used for the preparation of block copolymer.[150] The most common and easiest block copolymer preparation method using RAFT is through sequential addition of monomers with purification before each additional polymerization (Figure 2.35).[149, 156] A small amount of impurities, including initiator-derived block copolymer, initiator-derived homopolymers, dead copolymer and dead homopolymers, produced during the block copolymer RAFT polymerization is unavoidable. But with careful control of reaction condition, those impurities can be minimized and do not affect the performance of the final products.

First, the RAFT agent selection should be based on the rules mentioned above and appropriate for all the monomer types appeared in the block copolymer. Second, as shown in Figure 2.35, the **B** monomers are polymerized using a macro-RAFT agent with **A** block macro-R group, the **C** monomers are polymerized using a macro-RAFT agent with **A**-*b*-**B** diblock macro-R group, and so on. Therefore, the former macro-R group should be a good hemolytic leaving group for the propagating radical of the later adding monomer. Third, although a lower initiator concentration can decrease the amount of impurities, the polymerization rate also should be considered. Fourth, stop the polymerization with ~70% monomer conversion can reduce the dead chain contaminants in macro-RAFT agents. Fifth, macro-RAFT agents should be stored at low temperature and used as soon as possible.[149]

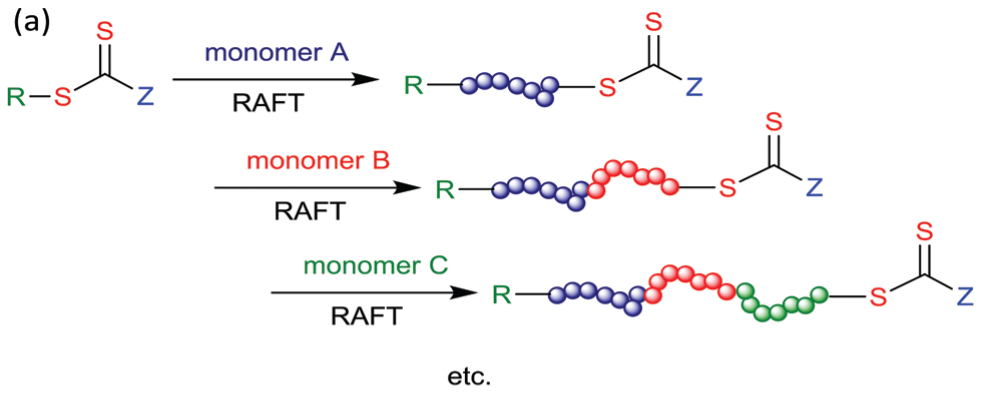

Figure 2.35. Schematic illustration of linear block copolymer synthesis by sequential monomer addition using RAFT method.[150]

2.5 X-ray photoelectron spectroscopy (XPS)

XPS is a technique heavily used for identifying and quantifying the elemental composition by assessing the electronic structure of the atoms and/or ions of a solid's outer surface within the first 10 nm. Figure 2.36 shows a schematic example of an XPS instrument and the data formats. The XPS instrument primarily consists of 3 items: an X-ray sours which usually are MgK_{α}(*hv* =1253.6 eV, linewidth 0.70 eV) and AlK_{α} (*hv* =1486.6 eV, linewidth 0.85 eV), an energy filter and a detection system. When X-ray is absorbed by atoms, electrons emitted from material surface can be collected then energy analyzed by the hemispherical detector. [157, 158]

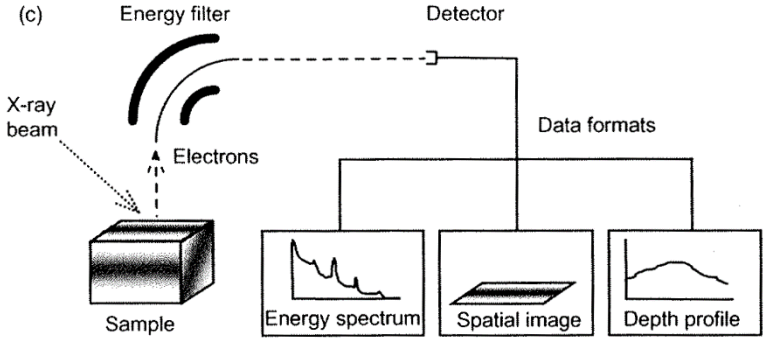

Figure 2.36. Basic component of an XPS instrument with 3 common means of relaying the data(from left to right): (1) Energy distribution of electron emissions falling within predefined energy rang; (2) Spatial distribution of an electron emission across a surface; (3) Depth distribution of an electron emission to a predefined depth (< 10 nm).[157]

2.5.1 Qualitative analysis

The principle of XPS is based on the element specific binding energy of electrons in the atomic shell and interaction between an electromagnetic wave (photon) and a material (atom or ion). The photoelectron emission process is going on 3 stages: (1) when X-ray interact with the elements in the atomic shells, the photoelectrons (Auger electrons) are generated; (2) part of the electrons move through the solid towards the surface and are subjected to various scattering processes (in which, the inelastically scattered electrons create the background); (3) after surmounting the work function threshold, the electrons reach the surface and emitted to the vacuum.[158] The energy diagram of photoelectron emission on carbon atom is shown in Figure 2.37. An excitation X-ray transfers its energy $h\nu$ to core electron with binding energy E_b (energy by which an electron is attracted to its nucleus). The kinetic energy (E_k) of emitted photoelectron is

$$E_k = h\nu - E_b - \psi \text{ [159]} \qquad (2.5)$$

Where ψ is the work function depending on the instrument, representing the minimum energy necessary to remove an electron to depart the solid.

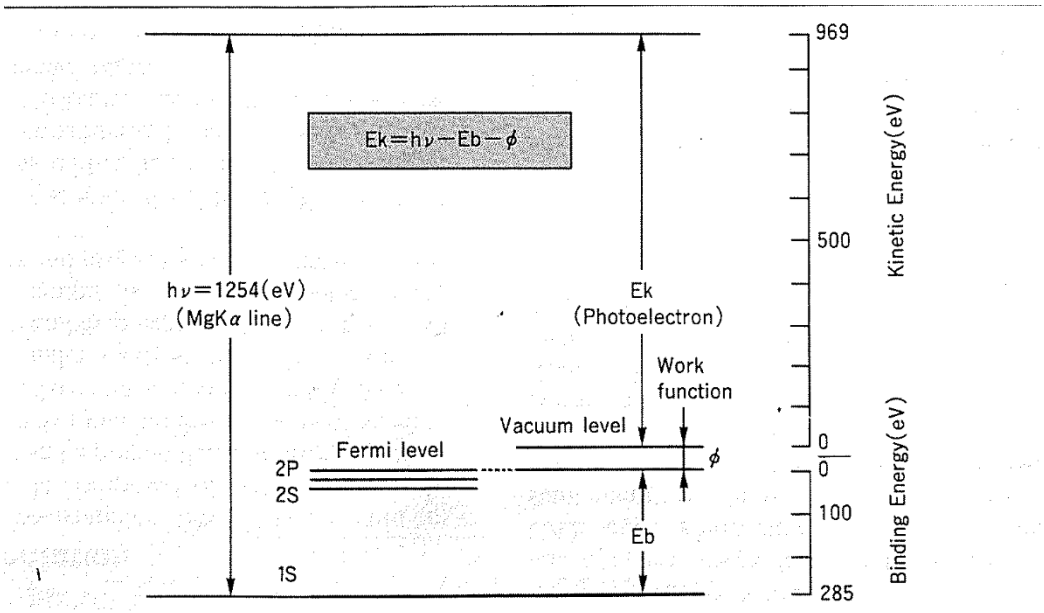

Figure 2.37. Energy diagram of photoelectron emission on carbon atom.[160]

XPS spectra are often given by intensity as a function of the binding energy. Figure 2.38 shows a wide scan XPS spectrum of an Mg surface. Beside the photoelectron peaks (Mg 1s, 2s and 2p), the KLL auger peak also is indicated. The photoelectron spectra of elements can be referenced the handbook provided by the instrument manufacturers or the internet database. The Auger electron energies are resulted from the filling of the core hole by an electron closer to the Fermi edge. But an Auger electron peak can be easily

distinguished in the XPS spectra from a photoelectron peak by changing the adjusting the X-ray source (for example, MgK_α to AlK_α), because the different energy moves the Auger peak along the spectra. Beside the photoelectron and Auger electron peaks, the satellite peaks also can be observed in the XPS spectrum, because of (1) satellite peaks without mono-chromator, (2) plasmon loss peaks and (3) shake-up, shake-off, multiplet splitting.[158]

Any change in the bonding state of an atom gives rise to chemical shifts and Full Width at Half Maximum (FWHM) of photoelectron peaks and sometime accompany satellite peaks. Chemical bonding in the compound generally causes a change of the E_b, leading to the chemical shift which can be qualitatively explained by the effective charge potential change on an atom. When an atom bonds with another atom with higher electronegativity, its charge transfers and becomes positive, leading to a shift of the photoelectron peak into a higher bonding energy. The valence state metal atoms typically show increasing shifts, as shown in Figure 2.39. The doublet shifts about 1 eV per valence (the electron transitions from levels with total angular momentum higher than *s*, for *p, d, f,* show doublet peak structures). The overlapping photoelectron peaks (due to multiple valence states of Ta) in the Figure 2.39 is separated by curve fitting.

When the features of photoelectron, Auger electron and satellite peaks are known in advance, the qualitative analysis of XPS is often easier.

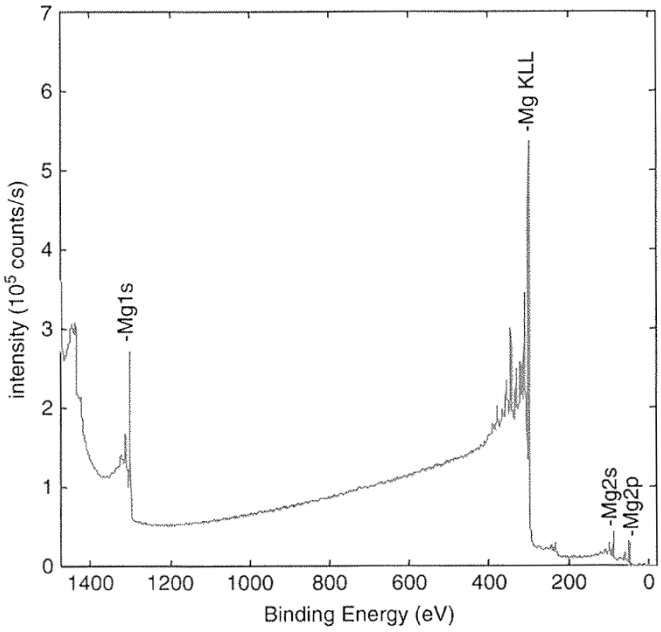

Figure 2.38. A wide scan XPS spectrum of a sputter-cleaned Mg surface.[158]

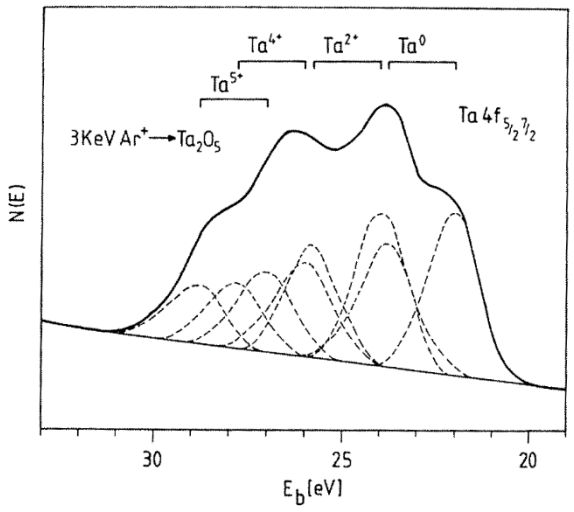

Figure 2.39. Decomposition of the Ta $4f_{5/2,7/2}$ doublet peak structure measured at a Ta_2O_5 sample after bombardment with 3 keV Ar^+.[158]

2.5.2 Quantitative analysis

In quantitative analysis, the energy spectra over all accessible energies (wide scan) is usually carried out at first and then concentrating on particular photoelectron signals (narrow scan), which ensures all the elements are accounted and time-effectivity.

In a XPS spectrum, the peak intensity of an element (i) in a uniform sample is generally determined by 3 major parameters: (1) photoionization cross section (σ) which is the probability that a photoelectron will be ejected from an atom/ion following photon irradiation; (2) inelastic mean free path (λ) which is defined as the average distance traveled by an electron of a specific energy within a particular single-layered homogeneous amorphous solid between two successive inelastic scattering events; (3) analyzer transmission (T) which is a parameter dependent on instrument geometry or experimental setup.

Therefore, the peak intensity (I_i) is giving by following equation:

$$I_i = C_i \cdot \sigma(\sigma_0, \alpha, \beta) \cdot \lambda(s, E_i) \cdot T(E_i) \qquad (2.6)$$

where C_i is the concentration of element i, σ_0 is the total photoionization cross section, α is the angle between the direction of X-ray and photoelectron emission, β is the asymmetry parameter and E_i is the kinetic energy of electrons of element i.[160]

There are 2 major methods for quantitative analysis. One method is to use standard samples. The concentration (C_i) of unknown sample can be obtained by following equation:

$$C_i = \frac{I_i}{\lambda(s, E_i)} \cdot \frac{C_i^{std} \cdot \lambda(std, E_i)}{I_i^{std}} \tag{2.7}$$

where the C_i^{std} is the concentration of standard sample, the $\lambda(std, E_i)$ and $\lambda(s, E_i)$ are inelastic mean free path of standard and unknown samples respectively, the I_i^{std} and I_i are peak intensities of standard and unknown samples respectively. This method is with ~10% accuracy.

The second method is without the need for reference materials and relative ease, but the accuracy is not better than 10% and even error up to 30%. The photoionization cross section (σ), inelastic mean free path (λ) and analyzer transmission (T) are encompassed into sensitivity factor (R), the concentration of element i (C_i) can be expressed by the equation:

$$C_i = \frac{I_i}{R_i} / \sum_j (\frac{I_j}{R_j}) \tag{2.8}$$

where j runs over all elements present.

To know how the elements present vary as a function of depth, there are 2 often used methods to draw the depth profile. One is sputter depth profiling which is done by analyzed the residual surface after a certain ion sputtering time. Other one is sample tilting method. The analyze volume is adjustable by varying the take-off angle θ (Figure 3.40), therefore changing the effective escape depth of photoelectrons. The peak intensity of element i (I_i) at take-off angle θ is given by:

$$I_i = C_i \cdot \sigma \cdot T \cdot \lambda \cdot sin\theta \tag{2.9}$$

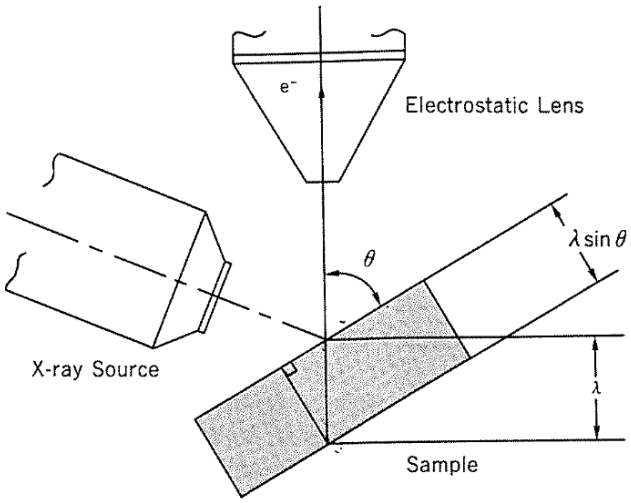

Figure 3.40. Principle of sample tilting method.[160]

3. Thermo-responsive mesoporous block copolymer membranes

DOI: 10.1021/acs.macromol.6b01665

3.1. INTRODUCTION

Stimuli-responsive membranes are an important class of functional membranes, and interest in these materials has increased dramatically in the last two to three decades. The permeabilities, selectivities, hydrophilic and hydrophobic behavior, absorption abilities, and optical properties of these membranes can be controlled by external stimuli, such as temperature, pH, ionic strength, electric and magnetic fields, and the presence of specific ions or molecules.[161] Among the stimuli-responsive membranes, thermoresponsive membranes have attracted significant attention because temperature is an easily adjustable environmental condition in biological and chemical systems. Changing the external temperature changes the pore diameters and surface properties of thermoresponsive membranes, which in turn affects the permeabilities, selectivities, and absorption abilities of the membranes. If thermoresponsive polymer chains are applied in combination with commercially available porous membranes, they can be used as functional gates. At low temperature, the swollen polymer chains attached inside the pore walls inhibit permeation through the membrane ("pore closing"), while, the deswelling of the polymer layer leads to increased permeability at high temperatures ("pore opening").[1, 162]

Up to now, most thermoresponsive membranes comprise poly(*N*-isopropylacrylamide) (PNIPAM), which has a lower critical solution temperature (LCST) at 32 °C. However, the fixed LCST of PNIPAM makes it difficult to tune the response temperature of PNIPAM membranes, and there are only a few examples of the thermoresponsive membranes with different response temperatures.[91, 92, 163-166] Xie and coworkers have developed thermoresponsive membranes by grafting NIPAM and acrylamide (AAM)/butyl methacrylate (BMA) copolymers onto macroporous membranes. The response temperature of these membranes was varied by adjusting the incorporation ratio of the hydrophilic (AAM) or hydrophobic (BMA) monomers in the PNIPAM chains. However, the membrane pores were very large, about 0.22 μm in diameter[166], and preparing thermoresponsive membranes with pore sizes smaller than 100 nm remains challenging. Until recently, thermoresponsive membranes were almost always prepared by surface modifying commercial template membranes using the "grafting to" and "grafting from" approaches. In the "grafting to" approach, diffusion of the thermoresponsive polymer chains into the pores is prevented by

grafted polymer brushes already on the membrane surface. In the "grafting from" approach, the monomer concentration becomes inhomogeneous in the pores and the control of polymerization is difficult.[1, 2] These inherent difficulties mean that these approaches are rarely used to prepare the thermoresponsive membranes with nanoscale pores. Furthermore, an uncontrolled modification easily results in pore plugging and loss of the easy barrier switching (a highly desirable property).[92] Alem *et al.* used atom transfer radical polymerization (ATRP) to grow PNIPAM brushes within two poly(ethylene terephthalate) (PET) membranes with pores measuring 0.08 μm and 0.3 μm, respectively. For the membrane with 0.3-μm sized pores, the PNIPAM grafted layer covered the entire pore surface homogeneously. However, the polymer brushes inside the small pores (0.08 μm) were not successfully grafted because of the supply of monomers in the narrow pores was low, inhibiting the growth of PNIPAM chains on the inner wall of smaller pores and leading to uneven grafting.[118]

Block copolymers (BCPs) are promising materials for the fabrication of ultrafiltration membranes because the chemically distinct but connected polymers microphase separate into periodic arrays of nanoscale domains.[71, 73] Extensive research has been carried out to develop BCP-based mesoporous membranes. One approach is to etch the minor phase component of the BCP selectively, while the remaining blocks maintain the integrity and mechanical stability of the final porous polymer materials. However, this etching method is polymer-specific and limited to BCPs containing degradable blocks. Moreover, the decomposed fragments may remain in the materials, causing secondary contamination.[102, 167] Swelling-induced pore-making is a new strategy for the preparation of mesoporous membranes with several advantages, including simplicity and high pore regularity. This approach starts from a block copolymer, and the pore-forming mechanism is based on the physical swelling of certain BCP domains. In this process, a self-assembled BCP is placed in a solvent that has a selective affinity for one of the block polymers, leading to swelling of the domains composed of this block. For example, a variety of block copolymers with CO_2-philic blocks can be turned into mesoporous materials by swelling with supercritical CO_2 at high pressure and de-swelling at atmospheric pressure.[168-177] While CO_2 is conveniently added to or removed from the system by changing the pressure, there are few CO_2–philic polymer species and these are always hydrophobic. However, supercritical or compressed CO_2 can also be mixed with another solvent to control the solvent quality; subsequently, CO_2 is removed at the end of the process. Poly(styrene-*b*-2-vinylpyridine) (PS-PVP) has been turned into a mesoporous material using this method.[178] Methanol alone has a strong affinity for PVP blocks and potentially swells the PVP domains; however, the glassy PS matrix prevents swelling. The addition of CO_2 to the methanol solvent reduces the glass transition temperature (T_g) of PS, allowing the PVP domains to swell with methanol; then, the CO_2 is removed from the mixture upon depressurization. We have used this method for pore fabrication in the membranes reported here. After that, this swelling-induced strategy has also been used, at room and elevated temperatures, to generate nanopores.[93, 146]

In this study, we prepared tunable thermoresponsive mesoporous membranes consisting of thin mesoporous selective layers of poly(oligo(ethylene glycol) methyl ether methacrylate)-*b*-polystyrene-*b*-poly(oligo(ethylene glycol) methyl ether methacrylate) ($PMEO_nMA$-*b*-PS-*b*-$PMEO_nMA$) on macroporous polyvinylidene fluoride (PVDF) support layers. In $PMEO_nMA$-*b*-PS-*b*-$PMEO_nMA$, *N* is the number of ethylene glycol units in the oligo(ethylene glycol) side chains, and the number of ethylene glycol units affects the LCST. The mesopores were introduced into the $PMEO_nMA$-*b*-PS-*b*-$PMEO_nMA$ films by controlled, selective swelling of the $PMEO_nMA$ domains with methanol assisted by compressed CO_2.[178] The compressed CO_2 plasticizes the continuous PS matrix to allow methanol to swell the dispersed $PMEO_nMA$ domains. Then, the compressed CO_2 was removed, followed by methanol, introducing mesopores into the $PMEO_nMA$ domains. Using this method, the hydrophilic component of the BCP, $PMEO_nMA$, covers the interior of the pores, thus polymers with tailored thermoresponsive barrier properties can be produced. The LCST of $PMEO_nMA$ can be conveniently selected by varying *N*;[50] therefore, by using $PMEO_nMA$-*b*-PS-*b*-$PMEO_nMA$ with different values of *N*, we obtained a series of thermoresponsive membranes with different response temperatures. Moreover, the response temperature can be fine-tuned by randomly copolymerizing ME*N*MAs with various numbers of ethylene glycol units. We investigated the water permeability the permeations of gold nanoparticles and dextran molecules through the thermoresponsive mesoporous membranes. Furthermore, we confirmed the thermos-responsivity and excellent size selectivity, which was found to be on the order of nanometers.

3.2. EXPERIMENTAL SECTION

3.2.1. Materials.

$PMEO_nMA$-*b*-PS-*b*-$PMEO_nMA$ polymers were synthesized by sequential anionic polymerization. The synthesis of the monomers and their polymerization and characterization have been reported elsewhere.[49] Table 3.1 summarizes the molecular characteristics of the $PMEO_nMA$-*b*-PS-*b*-$PMEO_nMA$ polymers used in this study. The $PMEO_{2.2}MA$ blocks were prepared by copolymerization of di(ethylene glycol) methyl ether methacrylate (MEO_2MA) (80 mol%) and tri(ethylene glycol) methyl ether methacrylate (MEO_3MA) (20 mol%).

Table 3.1. Properties of $PMEO_nMA$-*b*-PS-*b*-$PMEO_nMA$.

	Mn (kg/mol)	Weight percent of $PMEO_nMA$	Mw/Mn
$PMEO_2MA$-*b*-PS-*b*-$PMEO_2MA$	23.5-102-23.5	31.5%	1.08
$PMEO_{2.2}MA$-*b*-PS-*b*-$PMEO_{2.2}MA$	18.5-87-18.5	29.8%	1.07
$PMEO_3MA$-*b*-PS-*b*-$PMEO_3MA$	20.5-80-20.5	33.9%	1.10

Commercial polyvinylidene fluoride (PVDF) macroporous membrane discs (Φ = 2.5 cm) were purchased from Millipore, USA. The membranes had an average pore diameter of 220 nm. Deionized water was used in all experiments and was obtained from a water purification system (Millipore Ltd.).

3.2.2 Membrane preparation

Figure 3.1 shows the fabrication processes of the $PMEO_nMA$-*b*-PS-*b*-$PMEO_nMA$ composite membranes schematically. The $PMEO_2MA$-*b*-PS-*b*-$PMEO_2MA$, $PMEO_{2.2}MA$-*b*-PS-*b*-$PMEO_{2.2}MA$, and $PMEO_3MA$-*b*-PS-*b*-$PMEO_3MA$ BCPs were dissolved in chloroform (Wako, Japan) at a concentration of 4 wt%. PVDF membrane discs, used as support layers, were submerged in deionized water for several hours, allowing the water to penetrate into the pores, preventing the BCP solutions from flowing into the pores (Figure 3.1a). The BCP solutions were spin-coated onto the surface of water-prefilled PVDF membranes discs at 3000 rpm for 10 s, followed by vacuum drying at room temperature overnight to remove any residual solvent. Then the membranes were the heated to 130 °C for 10 min to enhance the adhesion between the $PMEO_nMA$-*b*-PS-*b*-$PMEO_nMA$ layer and the PVDF surface (Figure 3.1b). After forming the BCP-coated films into 13 mm diameter discs, mesopores were introduced into BCP layers by using the methanol-$scCO_2$ swelling method (Figure 3.1c).[178]

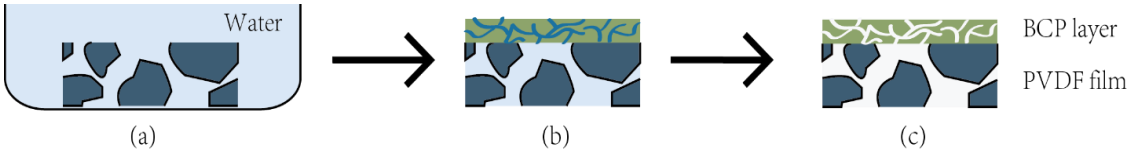

Figure 3.1. Schematic depiction for the fabrication processes of the composite membrane with mesoporous BCP as the selective layer and PVDF macroporous membrane as the supporting layer.

A stainless steel high-pressure vessel was used for the swelling processes. The vessel was connected to a high-pressure liquid chromatography pump (JASCO PU-2086 plus) with a cooling head and a back-pressure regulator (JASCO SCF-Bpg). The BCP-coated membranes and methanol were loaded into the high-pressure vessel which was immersed in a 45 °C water bath and then filled with CO_2 at 15 MPa. All samples were swelled for 30 min, followed by pressure release at a rate of 0.5 MPa/min. After the membranes had been removed from the vessel, methanol was removed from the specimens under vacuum for 1 h.[178] The produced composite membranes were stored in deionized water before the filtration measurements.

3.2.3. Scanning electron microscopy investigation

The morphological features of composite membranes were analyzed with a scanning electron microscope (SEM) (Hitachi S-4800). Samples were prepared for cross-sectional viewing by freezing for 2 to 3 minutes in liquid nitrogen, followed by fracturing. To improve the conductivity of the samples, the membranes were sputtered with a thin layer of platinum using an ion sputter coater (Hitachi E-1300).

3.2.4. Water permeability measurements.

The permeability of the PVDF base membrane and the $PMEO_2MA$-*b*-PS-*b*-$PMEO_2MA$, $PMEO_{2.2}MA$-*b*-PS-*b*-$PMEO_{2.2}MA$, and $PMEO_3MA$-*b*-PS-*b*-$PMEO_3MA$ composite membranes were measured using a custom dead-end filtration device (Figure 3.2) at several different temperatures and a transmembrane pressure of 0.2 bar. The BCP-coated side was faced the feed solution. A constant temperature circulator (Julabo F25-MC) was used to adjust the operating temperature during filtration. The dead-end filtration cell containing deionized water was kept in the temperature controlled water bath for at least 30 min before the filtration test. The filtrates were collected and weighed every 1 min for 15 min. Water permeabilities (*P*) at different temperatures were determined as follow:[179]

$$P\ (\mathrm{g/min \cdot bar \cdot cm^2}) = \frac{m_f}{\Delta p \times A \times \Delta t} \tag{3.1}$$

where m_f represents the weight of the filtrate, Δp is the transmembrane pressure, A is the effective membrane surface area (A = 0.8 cm^2), and Δt is the filtration time.

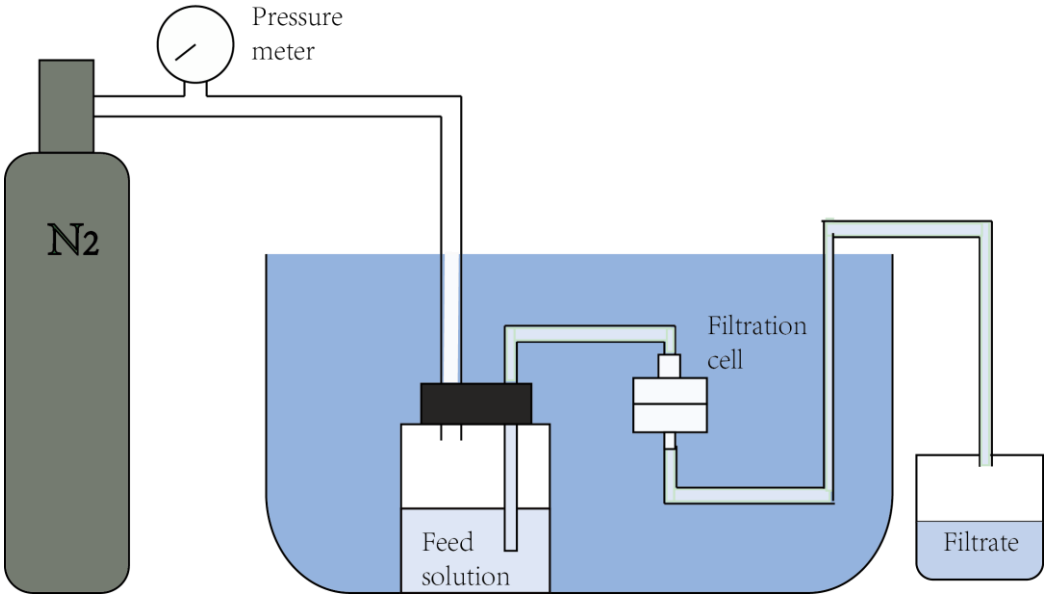

Figure 3.2. The homemade device used for investigate the water permeability.

3.2.5. Gold nanoparticles filtrations.

Two aqueous solutions containing different sizes of monodisperse colloidal gold nanoparticles (5 nm and 15 nm) (Sigma-Aldrich) were used as feed solutions to test the sieving characteristic of the membrane at different temperatures. The filtration experiments were performed with the filtration setup used to determine the water permeability. Filtration under the same conditions was repeated three times. The gold concentrations of the feed solution and filtrates were measured using a UV-visible spectrometer (Shimadzu UV-3150).

3.2.6. Dextran sieving tests

The sieving characteristic of $PMEO_2MA$-*b*-PS-*b*-$PMEO_2MA$, $PMEO_{2.2}MA$-*b*-PS-*b*-$PMEO_{2.2}MA$, and $PMEO_3MA$-*b*-PS-*b*-$PMEO_3MA$ composite membranes were investigated by dextran sieving measurements using polydisperse dextran with molecular weights of 1500–2800 kDa (Sigma-Aldrich D5376). The feed solution and standard solutions were composed of 0.20 wt% dextran, 0.02 wt% sodium azide (NaN_3), 0.30 wt% sodium chloride (NaCl), and deionized distilled water.[180] All the dextran solutions were pre-filtrated through 0.22 μm PTFE filter (Millipore Ltd.) to remove any undissolved dextran and salts prior to use.

Size exclusion chromatography (SEC) (JASCO) coupled with OHpak SB-804 HQ (Shodex) and G6000PWxl (TOSHO) tandem columns and a refractive index detector (JASCO RI-2031plus) was used to analyze the feed solution and filtrates. The analyses were carried out at 25 °C using deionized water containing 0.3wt% NaCl and 0.02wt% NaN_3 as the eluent. NaCl was used to stabilize the sample and NaN_3 inhibited the decomposition of dextran. The columns were calibrated using narrow molecular weight dextran standards (Sigma-Aldrich) ranging from 1 to 1100 kDa. A calibration curve was constructed using the following equation:[181]

$$\log\left(M_p\right) = \alpha \cdot V_R + \beta \tag{3.2}$$

where M_p represents peak average molecular weight, V_R is retention volume, and α and β are constants. Because the molecular weights of dextran used in feed solution (1500−2800 kDa) were greater than the size of the largest dextran standard (1100 kDa). The SEC retention times were converted to molecular weight by dextran calibration.

The rejection coefficient (R) is defined by Equation (3.3),

$$R = 1 - \frac{C_{filtrate}}{C_{feed}} \tag{3.3}$$

where $C_{filtrate}$ and C_{feed} are the concentrations of the feed solution and the filtrate, respectively, determined by the peak height of the elution curves.[182]

3.3. RESULTS

3.3.1. Morphology of the composite membranes

To form a bicontinuous structure after the swelling induced pore-making process, the initial volume fraction of the minority block copolymer component must be below the threshold that separates lamellar and cylindrical morphologies.[183] Therefore, the block copolymer chosen for the thermoresponsive membranes was $PMEO_nMA$-*b*-PS-*b*-$PMEO_nMA$ with volume fractions of the PS and $PMEO_nMA$ blocks of around 70/30. Based on the volume fraction of the asymmetric $PMEO_nMA$-*b*-PS-*b*-$PMEO_nMA$ used, the resultant films were expected to have a cylindrical morphology at equilibrium.

Figures 3.3a, 3.3c, and 3.3e show cross-sections of the $PMEO_2MA$-*b*-PS-*b*-$PMEO_2MA$, $PMEO_{2.2}MA$-*b*-PS-*b*-$PMEO_{2.2}MA$, and $PMEO_3MA$-*b*-PS-*b*-$PMEO_3MA$ composite membranes. All the membranes have double-layered composite structures with thin top layers supported by thick, macroporous PVDF bottom

layers. The top layers are composed of swelling-induced mesoporous $PMEO_nMA$-*b*-PS-*b*-$PMEO_nMA$ layers with a thickness of about 1 μm. The $PMEO_nMA$-*b*-PS-*b*-$PMEO_nMA$ layers tightly adhere to PVDF surface. There is no interfacial gap along the interface between these $PMEO_nMA$-*b*-PS-*b*-$PMEO_nMA$ and PVDF layers. Pores on the PVDF layers immediately below the interface are filled with $PMEO_nMA$-*b*-PS-*b*-$PMEO_nMA$, attributed to the slight penetration of the $PMEO_nMA$-*b*-PS-*b*-$PMEO_nMA$ melt into PVDF membrane during annealing at 130 °C. This slight penetration strongly increased the adhesion between the $PMEO_nMA$-*b*-PS-*b*-$PMEO_nMA$ and PVDF layers because the $PMEO_nMA$-*b*-PS-*b*-$PMEO_nMA$ in the pores of the PVDF membrane anchored the layers together. We found that, if the 130 °C thermo-annealing step was removed, the $PMEO_nMA$-*b*-PS-*b*-$PMEO_nMA$ layers could be easily peeled away from the PVDF support membranes after the swelling process. As shown in Figure 3.3b, 3.3d, and 3.3e, after swelling at 45 °C for 30 min with $scCO_2$ at 15 MPa, a bicontinuous porous structure was obtained over the entire top layer composed of $PMEO_nMA$-*b*-PS-*b*-$PMEO_nMA$.

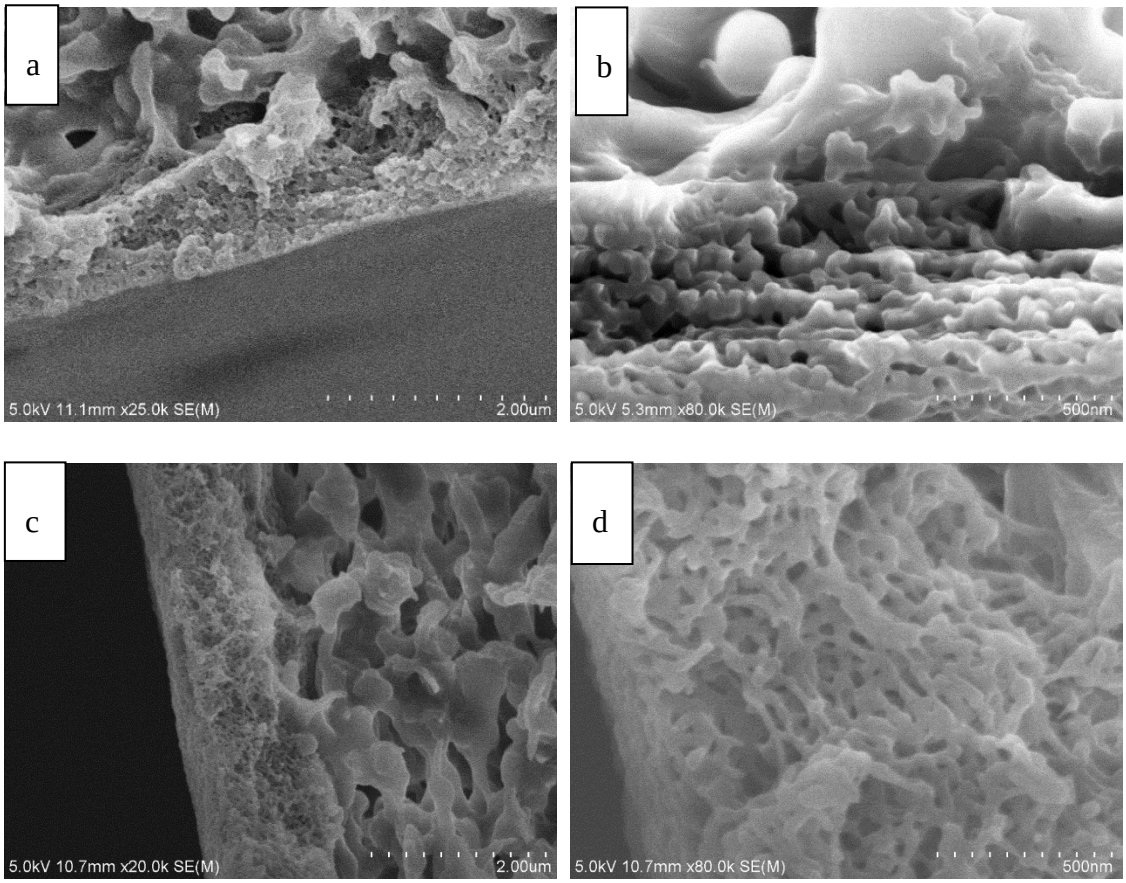

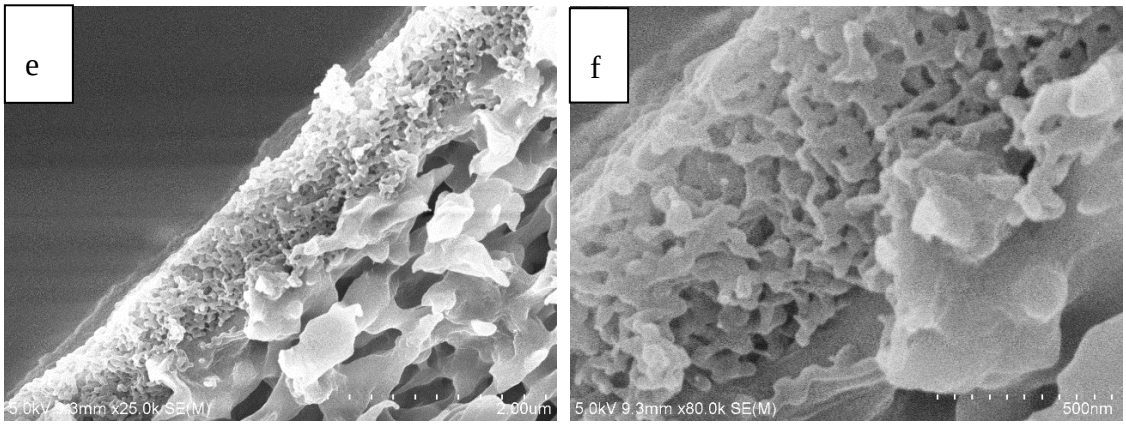

Figure 3.3. SEM images of cross-sectional view of composite membrane with $PMEO_2MA$-*b*-PS-*b*-$PMEO_2M$ in (a) and (b), $PMEO_{2.2}MA$-*b*-PS-*b*-$PMEO_{2.2}MA$ in (c) and (d), and $PMEO_3MA$-*b*-PS-*b*-$PMEO_3MA$ in (e) and (f) porous layer supported on the macroporous PVDF membrane. The scale bars in (a, c, e) correspond to 2 μm, and the scale bar in (b, d, f) corresponds to 500 nm.

The SEM images of the $PMEO_2MA$-*b*-PS-*b*-$PMEO_2MA$, $PMEO_{2.2}MA$-*b*-PS-*b*-$PMEO_{2.2}MA$, and $PMEO_3MA$-*b*-PS-*b*-$PMEO_3MA$ composite membrane surfaces are shown in Figure 3.4. The top views of the $PMEO_2MA$-*b*-PS-*b*-$PMEO_2M$ and $PMEO_{2.2}MA$-*b*-PS-*b*-$PMEO_{2.2}MA$ membrane surfaces show the formation of a tortuous nano-channel structure (Figure 3.4a and 3.4b), while the $PMEO_3MA$-*b*-PS-*b*-$PMEO_3MA$ membrane surface contains mesopores with partial connections (Figure 3.4c). However, bicontinuous porous networks were formed in all three membranes (as shown in Figure 3.3). Furthermore, water flowed well through all three membranes. The pores in each membrane have a narrow pore size distribution, and the average diameter of the mesopores of the $PMEO_2MA$-*b*-PS-*b*-$PMEO_2MA$, $PMEO_{2.2}MA$-*b*-PS-*b*-$PMEO_{2.2}MA$, and $PMEO_3MA$-*b*-PS-*b*-$PMEO_3MA$ composite membranes were approximately 50 nm, 30 nm, and 30 nm, respectively. Notably, all the samples were dry membranes with shrunken thermoresponsive brush layers; therefore, the morphological characteristics observed in the SEM images do not reflect the morphologies of the wet state, *i.e.*, the pore sizes seen in the SEM images must be larger than the pore sizes in aqueous solution.

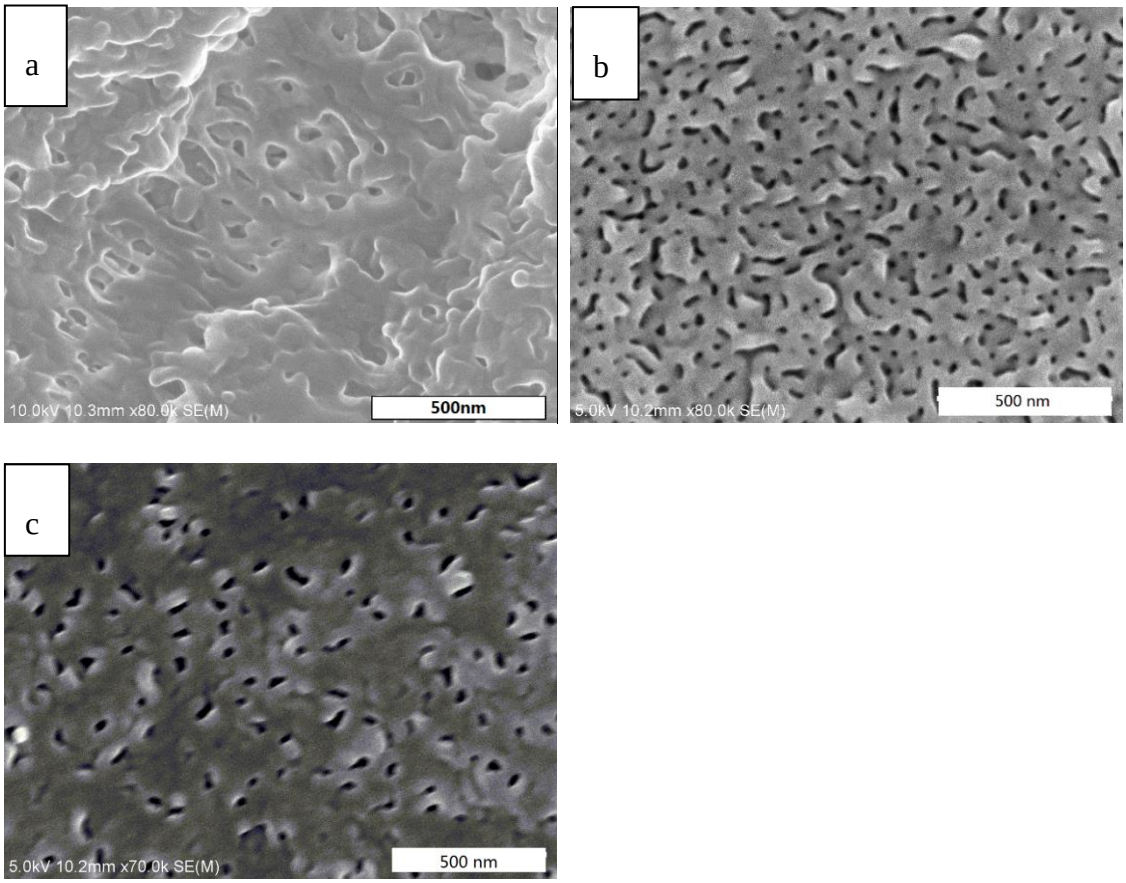

Figure 3.4. SEM images of top view of composite membrane with (a) $PMEO_2MA$-*b*-PS-*b*-$PMEO_2M$, (b) $PMEO_{2.2}MA$-*b*-PS-*b*-$PMEO_{2.2}MA$ and (c) $PMEO_3MA$-*b*-PS-*b*-$PMEO_3MA$ porous layers supported on the macroporous PVDF membranes.

The formation mechanism for the bicontinuous porous structures using methanol-$scCO_2$ swelling treatment is outlined in Figure 3.5. The main requisites to introduce nanostructures into the block copolymers are 1) to effectively plasticize the surrounding matrix, 2) selectively swell the minority compositions, and 3) freeze the morphology. Methanol can dissolve a large amount of CO_2, and the methanol-$scCO_2$ system can form a homogeneous phase above the vapor-liquid equilibrium line including the supercritical fluid phase. When the self-assembled $PMEO_nMA$-*b*-PS-*b*-$PMEO_nMA$ coated membrane (Figure 3.5a) is submerged into CO_2-expanded methanol (CEM), the $PMEO_nMA$-*b*-PS-*b*-$PMEO_nMA$ layer encounters the CEM both at the free top surface and the bottom surface, which adheres to the macroporous PVDF substrate, because the CEM can easily penetrate the microporous PVDF membrane and reach the $PMEO_nMA$-*b*-PS-*b*-$PMEO_nMA$ layer. Methanol alone has a strong affinity for $PMEO_nMA$ domains, but the $scCO_2$ effectively plasticizes the PS matrix, allowing methanol to diffuse easily into the $PMEO_nMA$ domains.[184] Due to the swelling induced volume expansion, the $PMEO_nMA$ domains fuse with neighboring domains, forming a continuous phase (Figure 3.5b). Upon depressurization, the methanol-$scCO_2$ system

phase separates, and the CO_2 is lost from the PS matrix. The PS domains become glassy, maintaining the polymer structure, while the $PMEO_nMA$ domains remain swollen with methanol. In the subsequent drying process, the swollen $PMEO_nMA$ blocks fixed on the solid PS walls release methanol and shrink. Consequently, bicontinuous mesopores are introduced into the swollen $PMEO_nMA$ domains and the pore walls are covered with $PMEO_nMA$ block chains (Figure 3.5c).

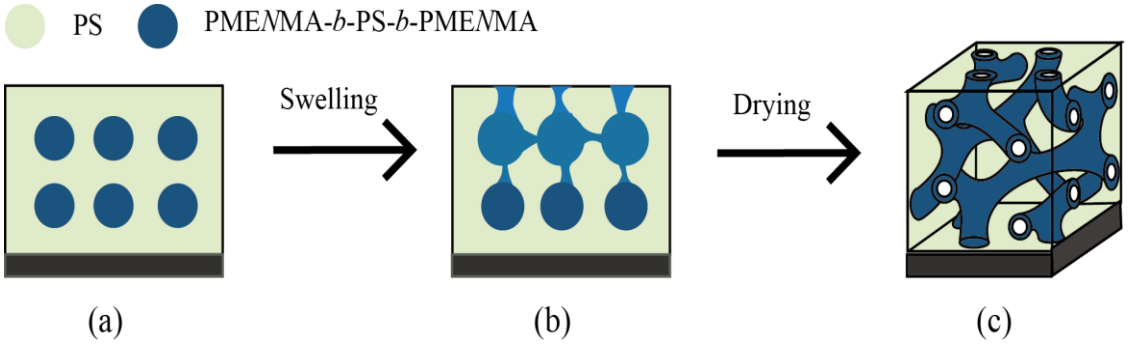

Figure 3.5. Schematic depiction for the Methnol-$scCO_2$ swelling method.

The porosity and pore size of the $PMEO_nMA$-*b*-PS-*b*-$PMEO_nMA$ layers can be manipulated by adjusting the pore fabrication parameters, such as swelling temperature, time, and the CO_2 pressure. In this study, these experimental parameters for the methanol-$scCO_2$ swelling process were fixed at 15 MPa, 45 °C, and 30 min, and the resulting porosities of the $PMEO_2MA$-*b*-PS-*b*-$PMEO_2MA$, $PMEO_{2.2}MA$-*b*-PS-*b*-$PMEO_{2.2}MA$, and $PMEO_3MA$-*b*-PS-*b*-$PMEO_3MA$ layers were about 17%, 36%, and 22%, respectively. These porosities were calculated by comparing the thickness of the $PMEO_nMA$-*b*-PS-*b*-$PMEO_nMA$ films before and after the swelling processes and assuming one-dimensional expansion.[168]

3.3.2. Thermoresponsive permeability of composite membranes

Figure 3.6 shows the results of water permeability experiment for the 220 nm PVDF base membrane and the $PMEO_2MA$-*b*-PS-*b*-$PMEO_2MA$, $PMEO_{2.2}MA$-*b*-PS-*b*-$PMEO_{2.2}MA$, and $PMEO_3MA$-*b*-PS-*b*-$PMEO_3MA$ composite membranes. The 220-nm PVDF membrane is highly permeable to water. The water permeability increased linearly with increasing temperature (Figure 3.6a) as a result of the lowering of water viscosity at higher temperatures. In contrast, the water permeabilities of the composite membranes changed nonlinearly as a function of temperature (Figure 3.6b-d). The drastic changes in water permeability arose from pore size changes, suggesting that the thermoresponsive $PMEO_nMA$ brushes had been formed inside the pores. The $PMEO_nMA$ brushes in the pores switched the membranes between "ON" and "OFF" states by thermally controlled conformational transitions. The conformational transition of $PMEO_nMA$ brush was related to the formation and breakage of hydrogen bonds between the ethylene oxide groups of

the $PMEO_nMA$ side chains and water molecules. At temperatures below the LCST, the $PMEO_nMA$ chains inside the pores are swollen, sealing the membrane pores. In contrast, the hydrogen bonds were broken at temperatures above the LCST, interactions between hydrophobic groups became dominant, and the $PMEO_nMA$ blocks collapse, resulting in the opening of the membrane pores. However, water flows through the composite membrane even in the "OFF" state because the swollen brushes in the mesopores function as gel-filled porous membranes; that is, the water permeability of the gel membrane is small but noticeable.

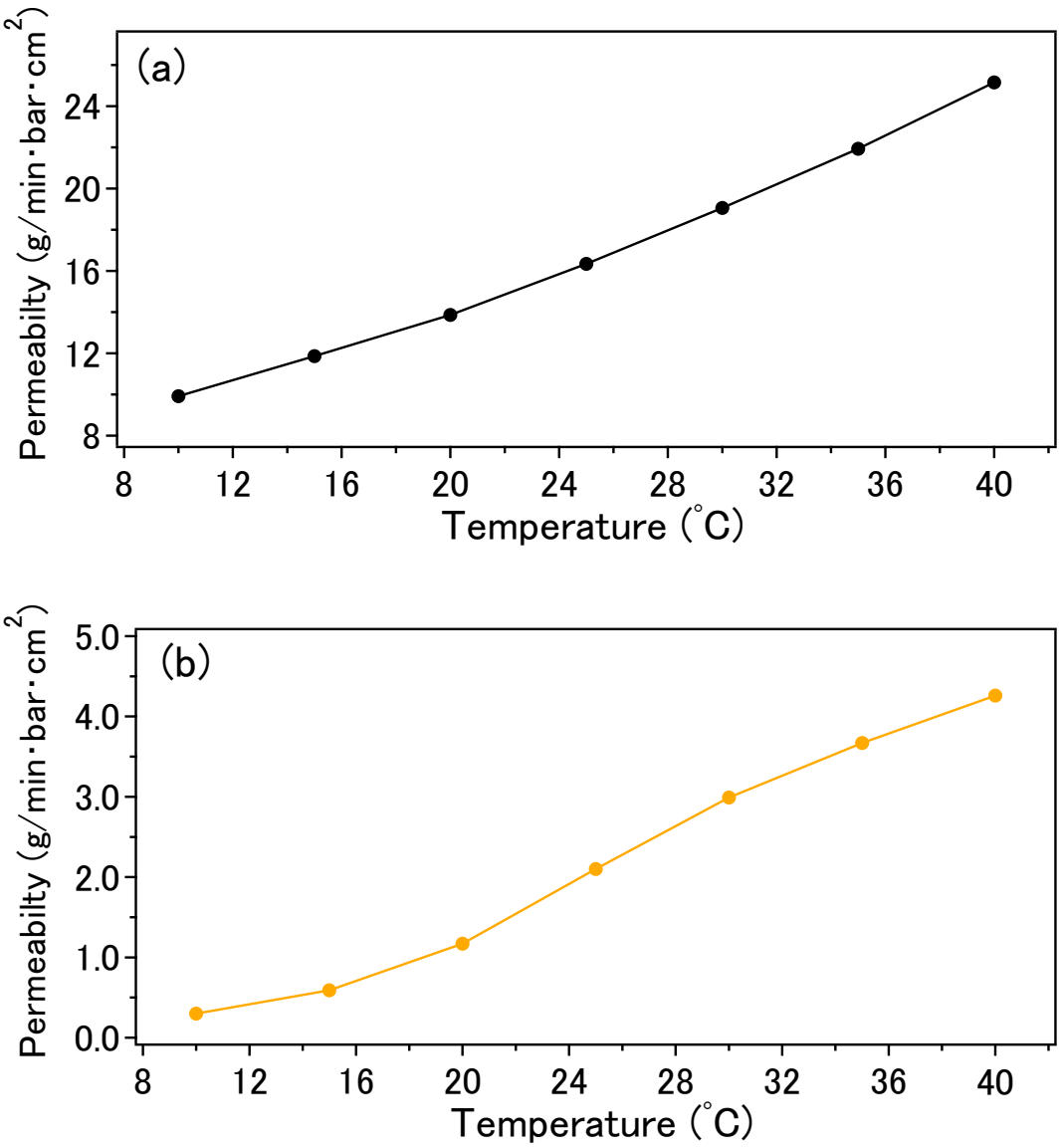

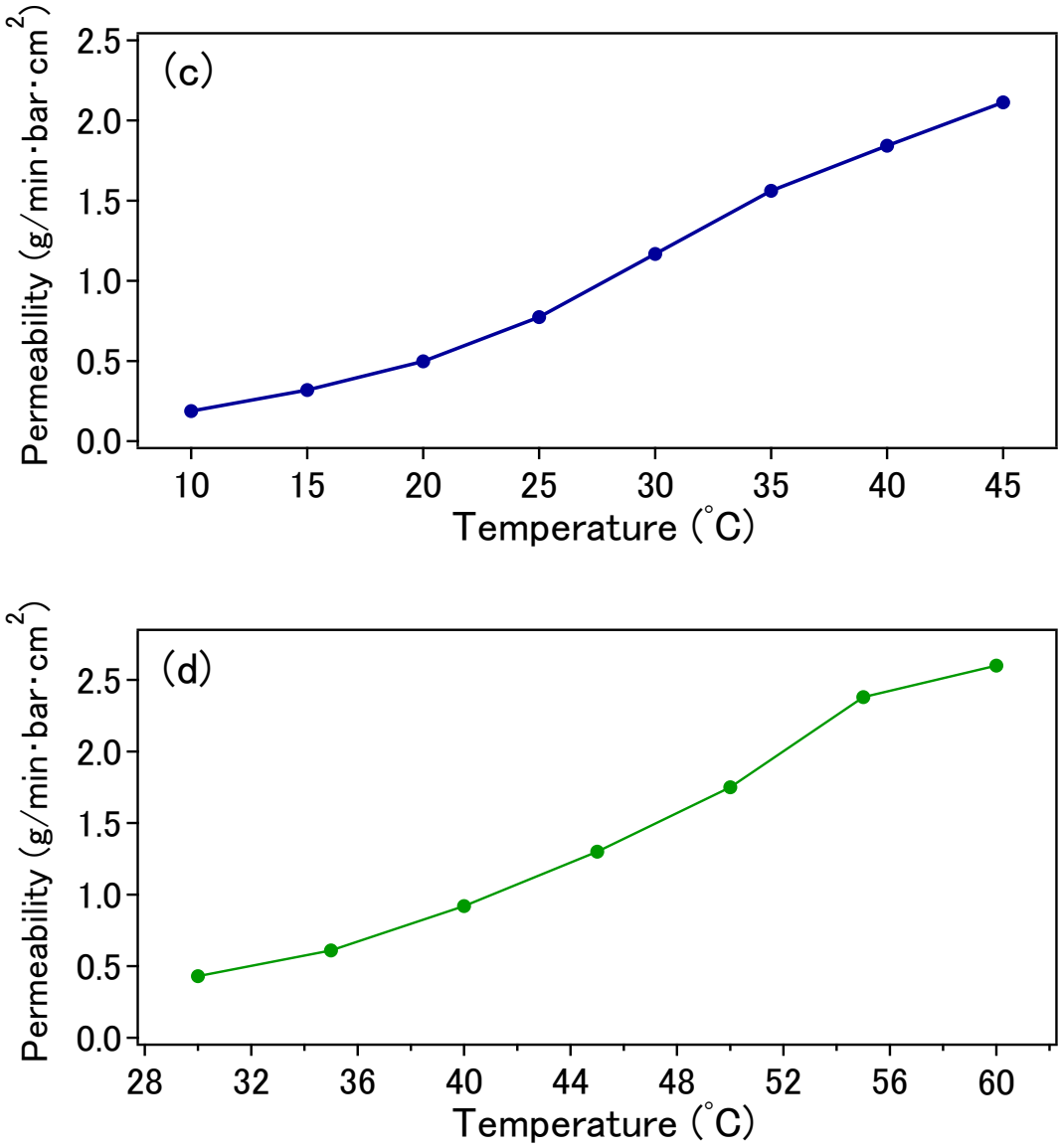

Figure 3.6. Water permeability versus temperature of (a) 220 nm PVDF membrane, (b) $PMEO_2MA$-*b*-PS-*b*-$PMEO_2M$, (c) $PMEO_{2.2}MA$-*b*-PS-*b*-$PMEO_{2.2}MA$ and (d) $PMEO_3MA$-*b*-PS-*b*-$PMEO_3MA$ membranes with transmembrane pressure at 0.2 bar.

As shown in Figure 3.6b–d, inflection points in the nonlinear plot of water permeability of the different composite membranes occurred in the vicinity of 25 °C, 30 °C, and 50 °C for the $PMEO_2MA$-*b*-PS-*b*-$PMEO_2MA$, $PMEO_{2.2}MA$-*b*-PS-*b*-$PMEO_{2.2}MA$, and $PMEO_3MA$-*b*-PS-*b*-$PMEO_3MA$ composite membranes, respectively. The shift in response temperature (the temperature at which the water permeability across the membrane changed dramatically) can be explained by the changes in the hydrophilicity of the $PMEO_nMA$ blocks with oligo(ethylene glycol) side chains of different lengths. $PMEO_nMA$ with long oligo(ethylene glycol) side chains, such as $PMEO_3MA$, contain a greater number of

hydrophilic ethylene oxide groups; consequently, more hydrogen bonds were formed at low temperature. The breakage of the hydrogen bonds requires high temperatures. Therefore, the $PMEO_3MA$-*b*-PS-*b*-$PMEO_3MA$ composite membrane shows highest response temperature among these the three composite membranes, and the response temperature of $PMEO_{2.2}MA$-*b*-PS-*b*-$PMEO_{2.2}MA$ was greater than that of $PMEO_2MA$-*b*-PS-*b*-$PMEO_2M$. Note that the copolymerization of $PMEO_nMA$ s with different numbers of ethylene glycol units is an effective method to tune the response temperature; thus, the response temperature can be fine-tuned through controlled copolymerization of $PMEO_nMA$. This unique control over the design, preparation, and pore-closing temperature of thermoresponsive membranes allows the preparation of thermoresponsive polymers for specific applications.

The $PMEO_2MA$-*b*-PS-*b*-$PMEO_2M$ composite membrane showed relative higher overall water flow rate than those of the $PMEO_{2.2}MA$-*b*-PS-*b*-$PMEO_{2.2}MA$ and $PMEO_3MA$-*b*-PS-*b*-$PMEO_3MA$ composite membranes. This greater flow rate was attributed to the larger pore size of the $PMEO_2MA$-*b*-PS-*b*-$PMEO_2M$ composite membrane compared with that of other two membranes, as shown earlier by SEM in Figure 3.4.

By using the Hagen-Poiseuille law, which takes the dependence of solvent viscosity on temperature into account, the thermoresponsive performance can be more quantitatively expressed. The permeability of the porous membranes is expressed as:

$$P = \frac{n\pi r^4 A}{8\eta}\frac{\Delta p}{\Delta x} \tag{3.4}$$

where P is the water permeability (g/min·bar·cm^2), n is the number of pores per cm^2, r is the pore radius, A is the membrane surface area, Δp is the applied pressure, η is the viscosity of the flowing liquid, and Δx is the membrane thickness.[185] Let r_0 represent the effective pore radius of membranes at standard temperature, T_0 (°C). T_0 was 10 °C for the PVDF, $PMEO_2MA$-*b*-PS-*b*-$PMEO_2M$, $PMEO_{2.2}MA$-*b*-PS-*b*-$PMEO_{2.2}MA$ membranes and 30 °C for $PMEO_3MA$-*b*-PS-*b*-$PMEO_3MA$ membrane. r_T is the pore radius at a T (°C), a temperature higher than T_0 (°C). The relative pore radius r_T/r_0 of the membrane is expressed as:

$$\frac{r_T}{r_0} = \left(\frac{J_T \eta_T}{J_0 \eta_0}\right)^{\frac{1}{4}} \tag{3.5}$$

where J_T and J_0 are the water flow rates at T (◦C) and T_0 (°C), and η_T and η_0 are the viscosities of the flowing liquid at T (◦C) and T_0 (°C).[179]

Figure 3.7 shows the relationship between the r_T/r_0 of the membranes and the temperature. The relative pore radius of the PVDF base membrane remained almost constant as a function of temperature, suggesting that, as expected. pore size is independent of temperature and that the temperature dependence of the water viscosity is effectively eliminated. The relative pore sizes increased gradually until the temperature reached 25 °C, 35 °C, and 55 °C for the $PMEO_2MA$-*b*-PS-*b*-$PMEO_2MA$, $PMEO_{2.2}MA$-*b*-PS-*b*-$PMEO_{2.2}MA$, and $PMEO_3MA$-*b*-PS-*b*-$PMEO_3MA$ composite membranes, respectively. The thermoresponsive performances of these composite membranes were quite different from those of typical PNIPAM membranes with pore sizes of the order of microns that alter their pore size abruptly around 32 °C.[102, 166, 186, 187]

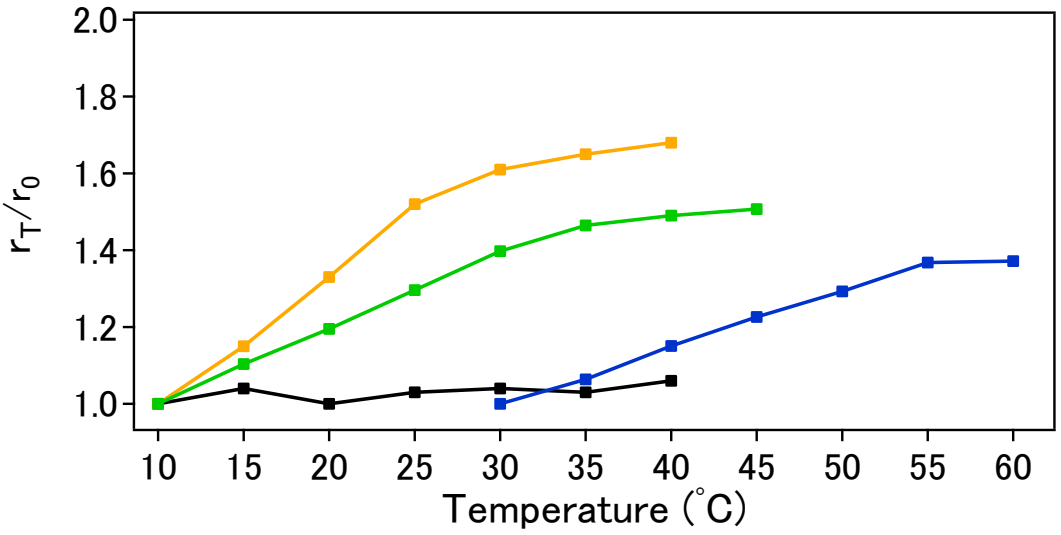

Figure 3.7. Relative pore radius (r_T/r_0) for 220 nm PVDF membrane (black), $PMEO_2MA$-*b*-PS-*b*-$PMEO_2M$ (orange), $PMEO_{2.2}MA$-*b*-PS-*b*-$PMEO_{2.2}MA$ (green) and $PMEO_3MA$-*b*-PS-*b*-$PMEO_3MA$ (blue) membranes.

The reversibility of the temperature response was verified by varying the temperature between 10 °C and 40 °C over several cycles (Figure 3.8). The water permeability recovery values are close to 100%, indicating that the switching was reversible, and confirming the stability of the porous structure of the composite membranes. There was no evidence of any damage to the mesoporous BCP layers under the applied pressure because 1) the triblock architecture of high molecular weight $PMEO_nMA$-*b*-PS-*b*-$PMEO_nMA$ is mechanically robust and 2) the rigid macroporous PVDF membrane support the thin $PMEO_nMA$-*b*-PS-*b*-$PMEO_nMA$ layer, preventing deformation of the porous structure of the thin $PMEO_nMA$-*b*-PS-*b*-$PMEO_nMA$ layer.

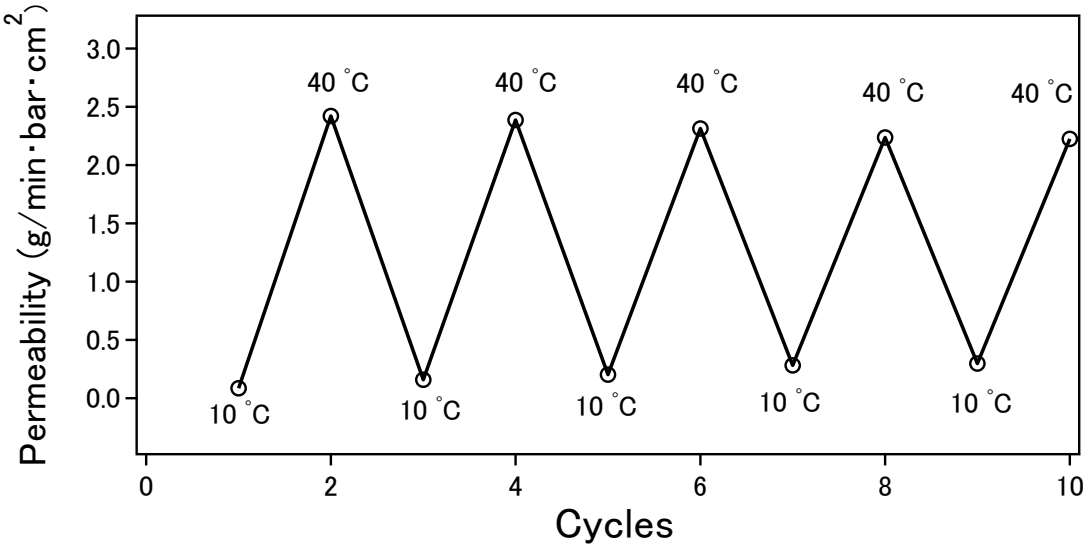

Figure 3.8. Water permeability of $PMEO_2MA$-*b*-PS-*b*-$PMEO_2M$ membrane at temperature cycling between 10 and 40 °C.

3.3.3. Thermoresponsive separation of gold nanoparticles

The transport of gold nanoparticles through the $PMEO_2MA$-*b*-PS-*b*-$PMEO_2M$ composite membranes was studied under ultrafiltration conditions to identify the thermo-dependent size selectivity of the membranes. Two kinds of gold nanoparticles with diameters of 5 nm and 15 nm in aqueous solution were chosen as the feed solutions. Both these gold nanoparticle solutions are red in color, and their UV-visible spectra contain peaks centered at approximately 520 nm, corresponding to the surface plasmon polariton generated within the gold nanoparticles.[188] Because the integrated intensity of the plasmon absorption of a gold nanoparticle solution is proportion to the concentration of nanoparticles, a UV-vis scanning spectrophotometer was chosen to measure the concentration of gold nanoparticle in the feed solutions and filtrates. Concerned about membrane fouling, we carried out each filtration experiment with a new $PMEO_2MA$-*b*-PS-*b*-$PMEO_2M$ composite membrane sample with the same pore size (50 nm, dry state).

Figure 3.9a shows the selectivity of the 5-nm gold nanoparticles through the $PMEO_2MA$-*b*-PS-*b*-$PMEO_2M$ composite membranes at different temperatures. When the temperature was 40 °C, the 5-nm gold nanoparticles passed through the membrane with a very little rejection. Consequently, the composite membrane covered by shrunken $PMEO_2MA$ chains must have a pore sizes larger than 5 nm at 40°C. A decrease in temperature to 30 °C led to an increase in the 5-nm gold nanoparticles rejection, indicating that the membrane pore size shrank at 30 °C as a consequence of the swelling of the $PMEO_2MA$ chains. When the temperature was lowered to below the LCST of $PMEO_2MA$, the filtrates were colorless, and there was

no absorption at 520 nm in the UV-vis spectra, suggesting that the 5-nm gold nanoparticles were completely blocked and the membrane pores have diameters smaller than 5 nm. Even when the plasmon peak disappeared in the spectrum of the filtered solution, a weak absorption in the low wavelength region was observed. The absorption does not arise from the gold nanoparticles but from the compound used to stabilize the 5-nm colloidal gold particles. Therefore, we subtracted this background from the spectrum (Figure 3.9b) and estimated the number of gold particles that have passed through the membrane from the peak intensity at 520 nm (Figure 3.10). The decrease in rejection rate with increasing temperature indicates the thermo-controllable size selectivity of the membranes.

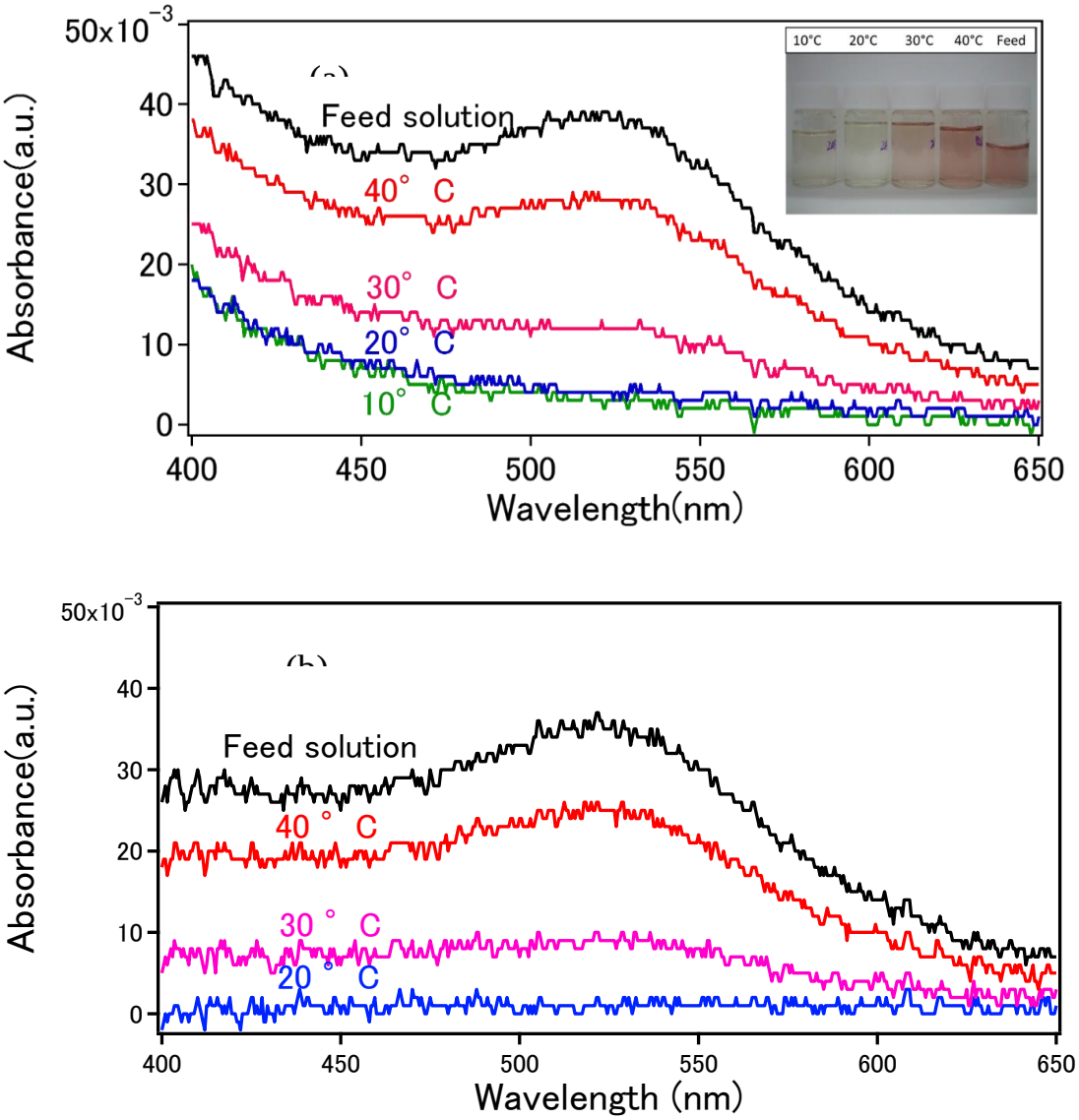

Figure 3.9. (a) UV-vis spectra of feed solution and filtrate obtained in the filtration of 5-nm gold colloidal particles solution at different temperature ($PMEO_2MA$-*b*-PS-*b*-$PMEO_2M$ membrane) with the inset of the

photograph of feed solution and filtrates, and (b) the corrected spectra by subtracting the background using the spectrum at 10 °C.

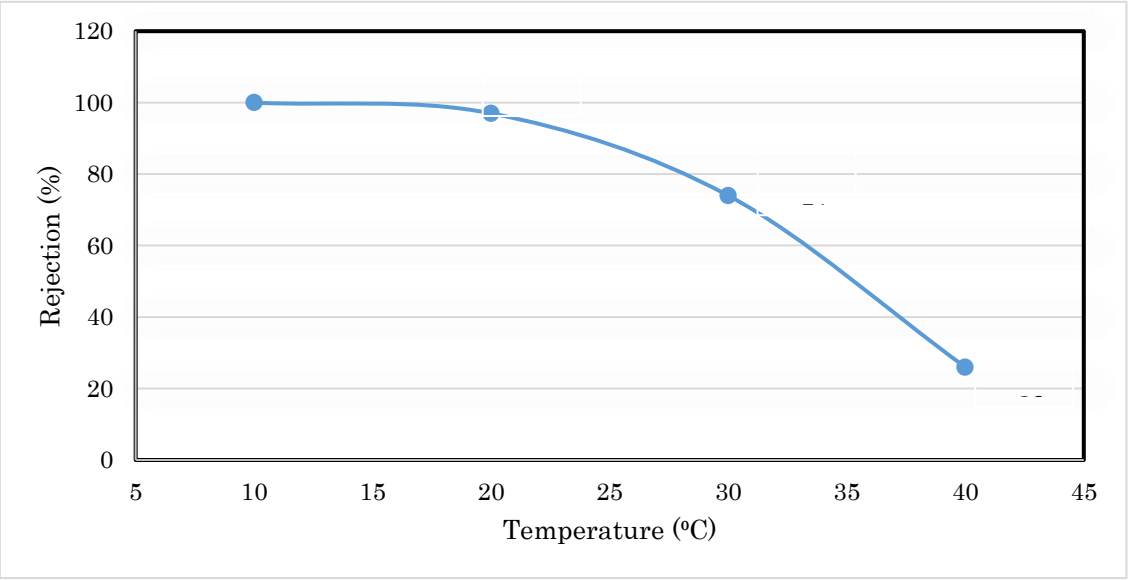

Figure 3.10. 5-nm gold nanoparticles rejection rates through the PMEO$_2$MA-*b*-PS-*b*-PMEO$_2$M membrane at different temperature. (The rejections were calculated by comparing the absorbance at 520 nm between feed solution and filtrates).

Figure 3.11 shows the UV-vis spectra of feed solution and filtrate produced after filtration of the 15-nm gold nanoparticle solution at 40 °C. In sharp contrast to the permeation results for colloidal 5-nm gold nanoparticles at 40°C, all the 15-nm gold nanoparticles were filtered out from the feed solution. The effective separation of particles three times size larger indicates that the PMEO$_2$MA-*b*-PS-*b*-PMEO$_2$M composite membrane has a strong size selectivity, which is attributed to the uniform distribution and almost identical length of the PMEO$_2$MA chains on the pore walls and the relatively narrow size distribution of the membrane pores.

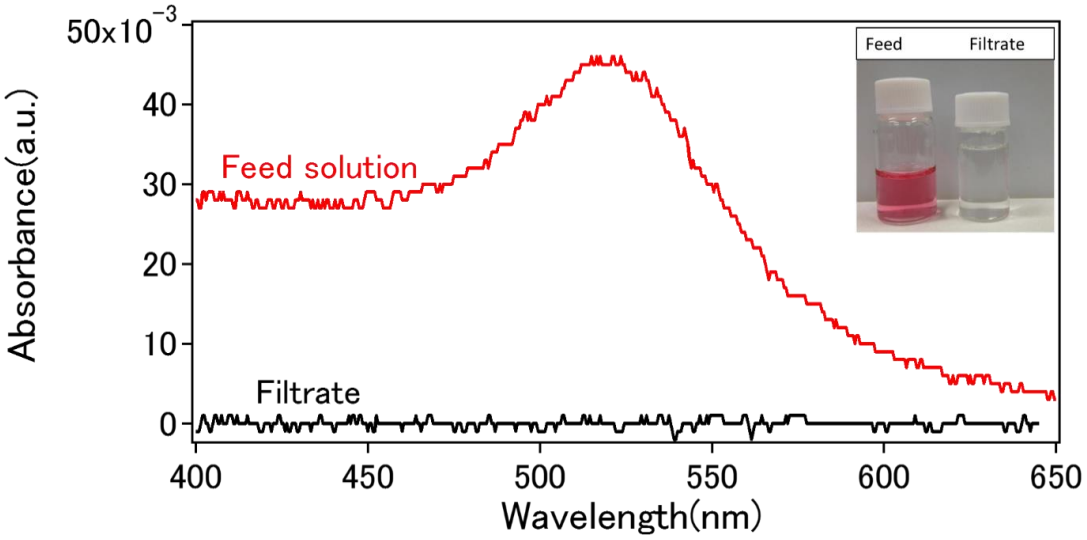

Figure 3.11. UV-vis spectra of feed solution and filtrate obtained in the filtration of 15-nm gold particles solution at 40°C ($PMEO_2MA$-*b*-PS-*b*-$PMEO_2M$ membrane). The inset is the photograph of feed solution and filtrate.

3.3.4. Thermoresponsive separation of dextran molecules

A polymeric dextran solution was also used as a feed solution to test the size-discriminating properties of the $PMEO_nMA$-*b*-PS-*b*-$PMEO_nMA$ composite membranes. Dextran was chosen because its polymers are neutral and do not interact with the studied membranes, are well characterized, and have a broad size (molecular weight) distribution over the whole size range of the pores found in our membranes.[189]

Figure 3.12 displays the dextran rejection coefficients obtained using the $PMEO_2MA$-*b*-PS-*b*-$PMEO_2MA$, $PMEO_{2.2}MA$-*b*-PS-*b*-$PMEO_{2.2}MA$, and $PMEO_3MA$-*b*-PS-*b*-$PMEO_3MA$ composite membranes at different temperatures. The selectivity of the dextran was temperature dependent for all composite membranes, being 5 °C for $PMEO_2MA$-*b*-PS-*b*-$PMEO_2M$, 10 °C for $PMEO_{2.2}MA$-*b*-PS-*b*-$PMEO_{2.2}MA$, and 30 °C for $PMEO_3MA$-*b*-PS-*b*-$PMEO_3MA$. In addition, very large overall rejection coefficients were observed due to the swollen $PMEO_nMA$ chains that switched the membranes into the "OFF" state. As temperature increased, the rejection coefficient of each composite membrane decreased, and the downward shifts in rejection were sharper around their LCSTs. The results again exhibit that the swelling/deswelling transition of the $PMEO_nMA$ chains on the composite membranes occurred slowly and continuously around the LCSTs (Figure 3.13).

(a)

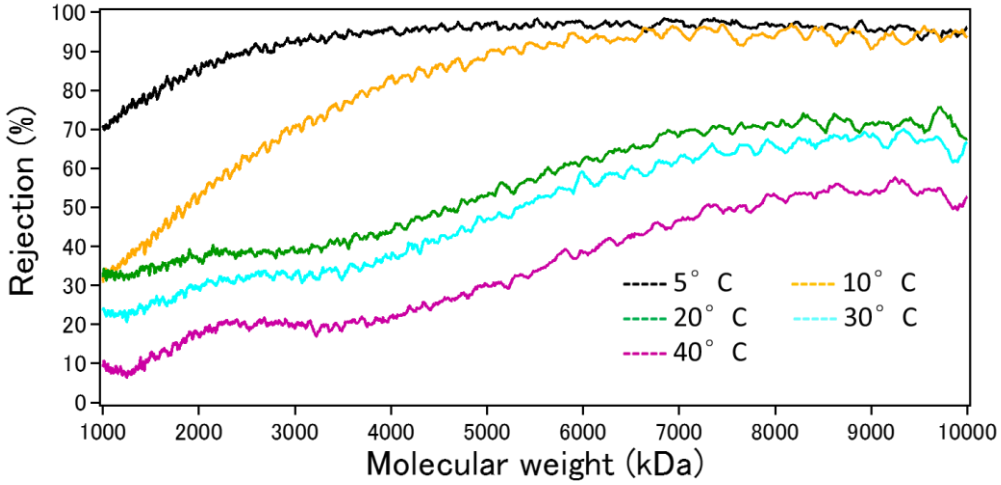
Rejection (%)
Molecular weight (kDa)
5° C
10° C
20° C
30° C
40° C

(b)

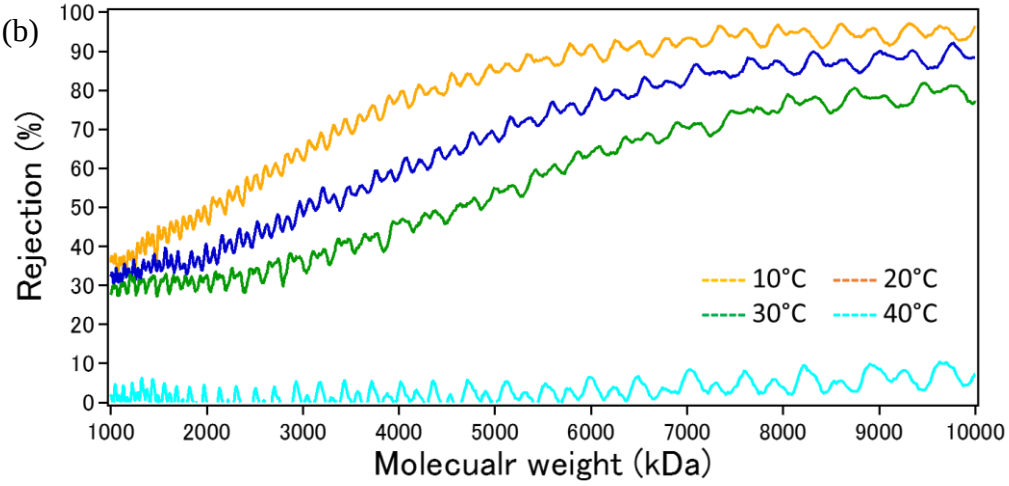
Rejection (%)
Molecualr weight (kDa)
10°C
20°C
30°C
40°C

(c)

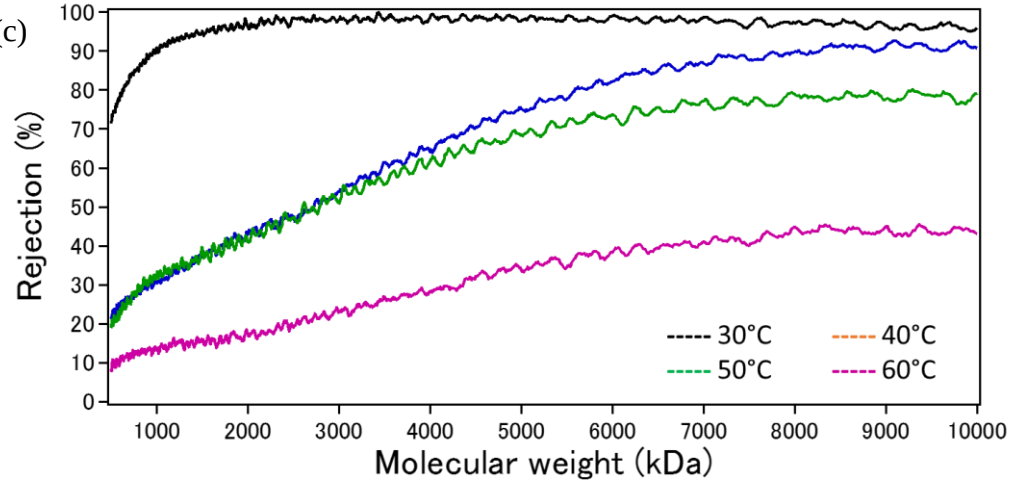
Rejection (%)
Molecular weight (kDa)
30°C
40°C
50°C
60°C

Figure 3.12. Rejection coefficients as a function of dextran molecular weight obtained during filtration of a 0.2wt% 1500-2800kDa dextran solution through (a) $PMEO_2MA$-*b*-PS-*b*-$PMEO_2M$, (b) $PMEO_{2.2}MA$-*b*-PS-*b*-$PMEO_{2.2}MA$ and (c) $PMEO_3MA$-*b*-PS-*b*-$PMEO_3MA$ composite membranes.

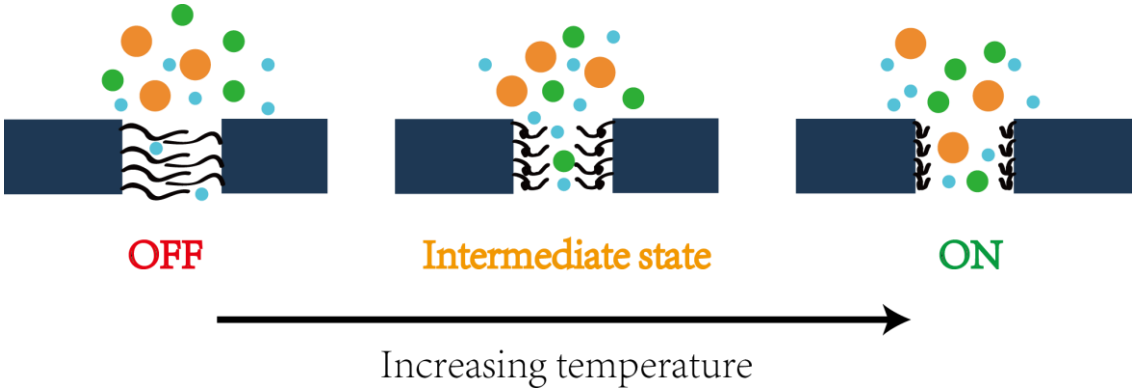

Figure 3.13. Schematic depiction for the switchable barrier properties of the $PMEO_nMA$-*b*-PS-*b*-$PMEO_nMA$ thermo-responsive membrane.

The hydrodynamic radii of the polymeric dextrans were calculated using the Stokes-Einstein equation:[181]

$$r_s = \frac{kT}{6\pi\mu D_{20}} \tag{3.6}$$

where k is the Boltzmann constant (k = 1.38 × 10^{-23} J/K), T is the absolute temperature, μ is the solution viscosity, and D_{20} is the diffusion coefficient at 20 °C.

The diffusion coefficients (m^2/s) have been experimentally related to the molecular weight, M_w (Da), by Equation (3.7). [190]

$$D_{20} = 7.667 \times 10^{-9} \times M_w^{-0.47752} \tag{3.7}$$

The rejection coefficients of $PMEO_2MA$-*b*-PS-*b*-$PMEO_2M$ composite membrane at 20 °C are shown as a function of dextran Stokes radius in Figure 3.14. The smallest dextran that produced a rejection of around 70 % had a radius of 51 nm. However, the filtration results obtained using a feed solution containing 5-nm gold particles suggest that the pore size of the $PMEO_2MA$-*b*-PS-*b*-$PMEO_2M$ composite membrane at 20 °C was less than 5 nm (diameter).

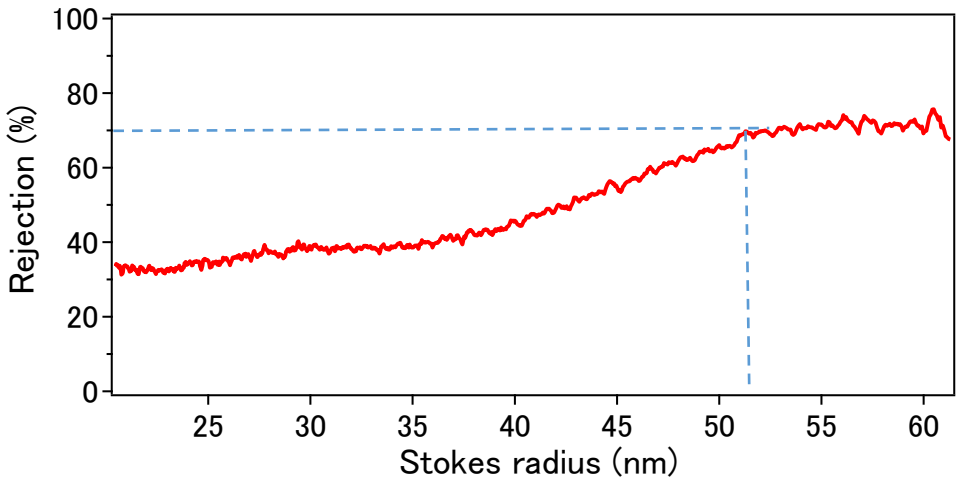

Figure 3.14. Rejection coefficients as a function of dextran stokes radius obtained during filtration of a 0.2wt% 1500-2800kDa dextran solution $PMEO_2MA$-*b*-PS-*b*-$PMEO_2M$ composite membranes at 20°C.

To understand these contradictory results from gold colloidal nanoparticles and dextran sieving experiments, which were carried out under the same operating conditions, ultrafiltration with both dextran and 5-nm gold nanoparticles feed solutions was investigated as a function of transmembrane pressure at 10°C. In Figure 3.15, the curves show a deviation from 100% fractionation for certain molecular weights of dextran with increasing transmembrane pressure. All the dextran molecules were blocked by the composite membrane at 0.03 bar, but only dextrans with small molecular weights permeated the membrane at 0.2 bar. When the pressure was increased to 3 bar, the membrane showed no sieving of dextran particles with molecular weights ranging from 1000 to 10000 kDa. For all the experiments, there was no evidence of any bypass or leakage. Figure 3.16 shows the UV-vis spectra of 5-nm gold nanoparticles feed solution and that of the filtrate obtained at 0.2 bar and 3 bar. Although the transmembrane pressure was increased from 0.2 bar to 3 bar, the 5-nm gold particles were still filtered out of the feed solution, suggesting that the pore size of the membrane did not change significantly at these two transmembrane pressures.

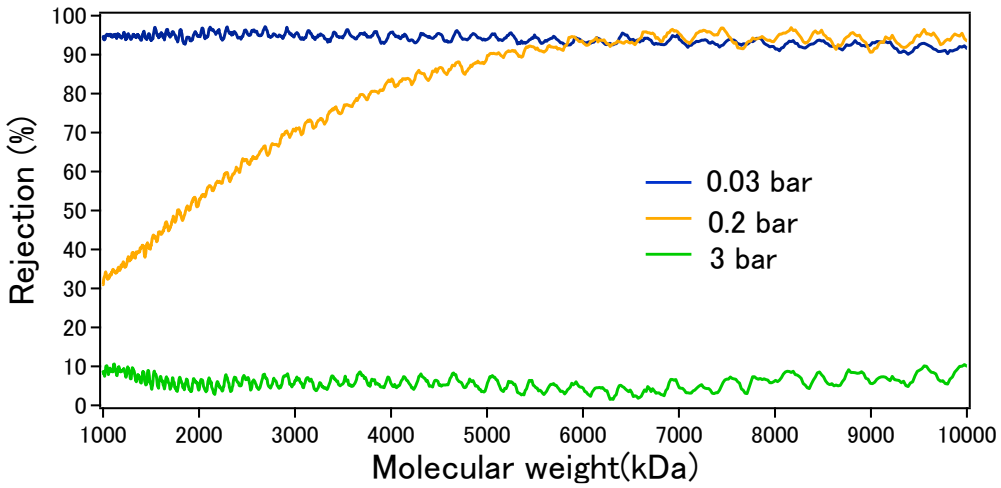

Figure 3.15. Rejection coefficients as a function of dextran molecular weight obtained during filtration of a 0.2wt% 1500-2800kDa dextran solution at different transmembrane pressure.

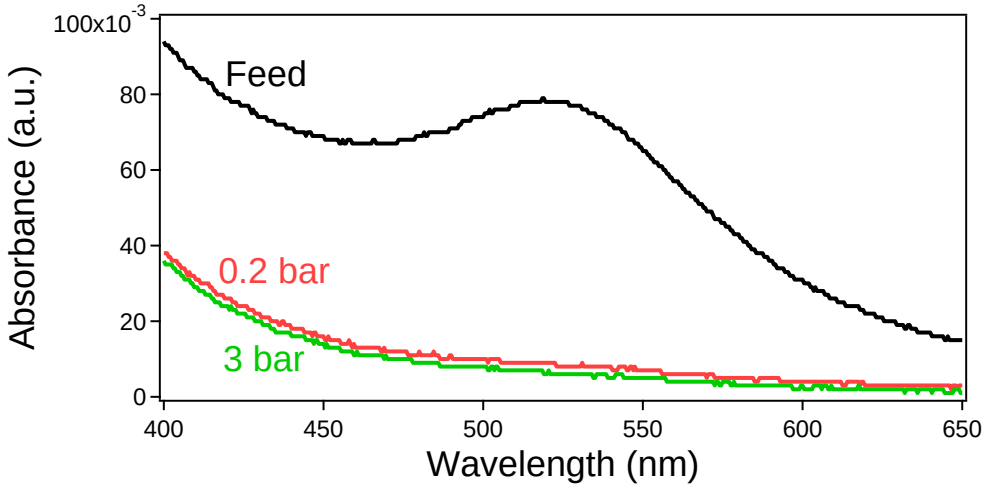

Figure 3.16. UV-vis spectra of feed solution and filtrate obtained in the filtration of 5-nm gold colloidal particles solution with different transmembrane pressure.

Combining the pressure-dependent ultrafiltration results, the contradictory evidence from the sieving experiments can be explained by the deformation and reptation motion of dextran molecules (Figure 3.17). The gold nanoparticles are hard spheres, whereas dextrans are flexible molecules, which are anticipated to be much more sensitive to shearing forces. At high transmembrane pressures, the convective water permeability through the $PMEO_nMA$ A brush-covered membrane pores imposed a stronger drag force onto the solute dextran molecules. Thus, the dextran molecules were extended through the pores and convectively drawn through the $PMEO_nMA$ brush covered pores with increasing transmembrane pressure. The extended dextran chains may also diffuse faster by reptation. The $PMEO_nMA$ brushes on the pore walls

should also be affected by elastic deformation; however, the deformation of soft particles (dextran molecules) is the main reason for the difference in ultrafiltration results between soft and hard particles, *i.e.*, dextran and 5-nm gold particles, respectively. No effect of transmembrane pressure was observed on the filtration of 5-nm gold nanoparticles by the membrane.

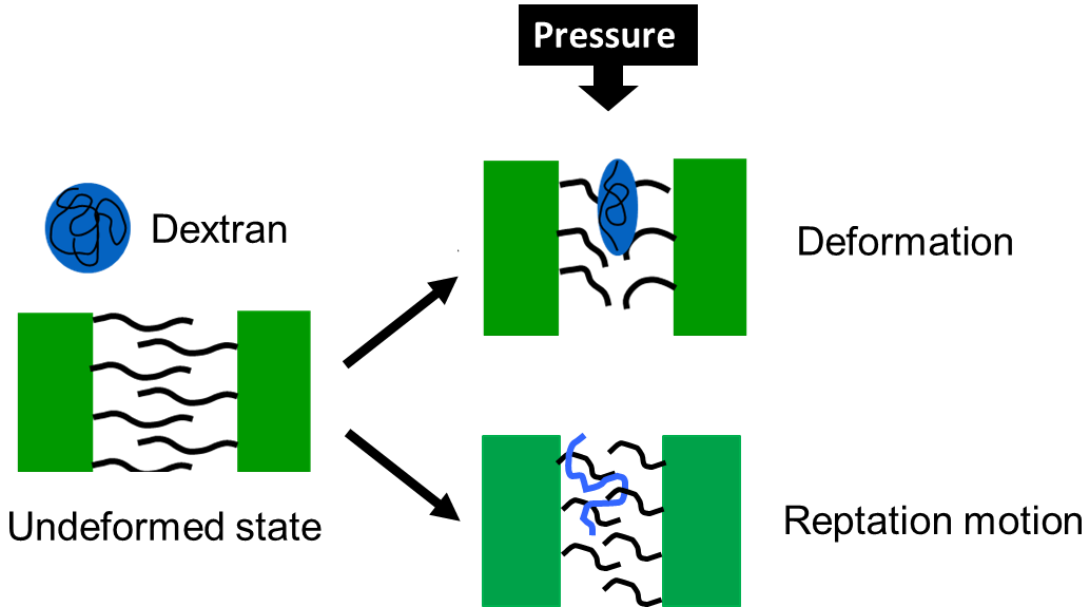

Figure 3.17. Schematic depiction for deformation and reptation motion of dextran molecules during the filtration.

3.4. CONCLUSION

In this study, we successfully prepared thermoresponsive block copolymer membranes with controllable response temperatures. These two-layer membranes consist of thermoresponsive mesoporous PMEO$_n$MA-*b*-PS-*b*-PMEO$_n$MA films as size-selective layers on macroporous, supporting PVDF films. SEM images of the samples show that a bicontinuous mesoporous network was formed in the BCP films. Water permeability results shown that the pores increased gradually in size until the temperature reached the response temperature of each membrane, ranging from 25°C to 55°C. The PMEO$_n$MA chains covering the interior of the mesopores provide the composite membranes with their temperature-dependent, tailored barrier properties. Furthermore, due to the ability to alter the LCST of PMEO$_n$MA by changing the number of ethylene oxide side chains, the response temperature is tunable. The temperature dependent size selectivity of the composite membranes was confirmed by conducting gold nanoparticles and dextran sieving experiments. The results indicate that the size selectivity of the membranes is strongly discriminating for hard particles such as gold and that an “ON”/”OFF” transition, related to the opening

and closing of pores, occurs around the BCP LSCTs. In addition, we observed that, at 20°C, the $PMEO_2MA$-*b*-PS-*b*-$PMEO_2M$ composite membrane permits the transport of the dextran with Stokes radii smaller than 51 nm, while 5 nm diameter gold nanoparticles passed through. Unlike the gold nanoparticles, which are hard spheres, dextran molecules are flexible chains that can be easily extended in the nanopores under shear forces, resulting in their transport through the membranes under convective flow.

3.5 SUPPORTING INFORMATION (Stability of composite membrane)

The pressure dependence of water permeability for $PMEO_2MA$-*b*-PS-*b*-$PMEO_2M$ composite membranes were measured using a dead-end filtration device at 15 °C (Figure S3.1). The pressure was stepwise increased from 0.2 bar to 4.0 bar with 10 min at each stage (black dots). Then, the water permeability was re-measured at 0.2 bar (red square point) with a value which is close to the previous one. The very good recovery indicates the wonderful stability of composite membranes.

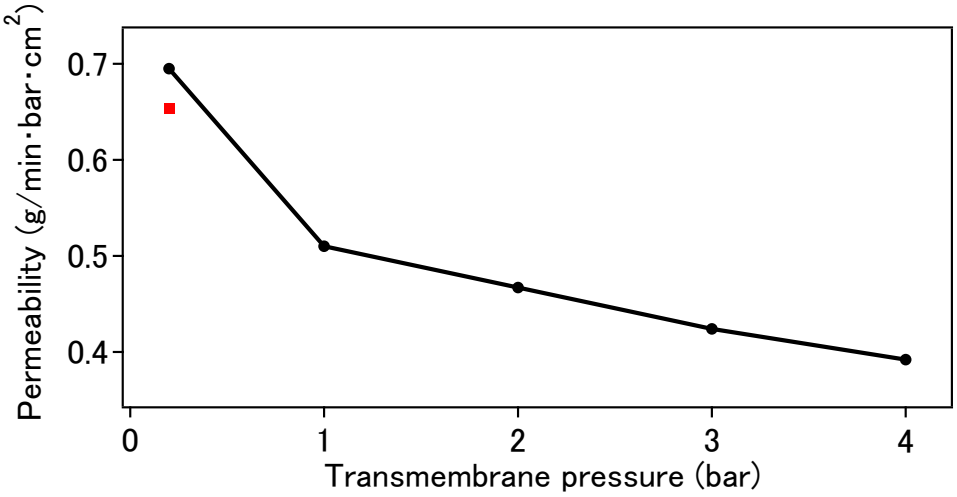

Figure S3.1. Water permeability versus transmembrane pressure of $PMEO_2MA$-*b*-PS-*b*-$PMEO_2M$ membrane at 15 °C.

4. Magneto-responsive mesoporous block copolymer membranes

DOI: 10.1021/ie401853k.

4.1. INTRODUCTION

Stimuli-responsive membranes are an important class of functional materials that can change their chemical, physical and barrier properties by responding to the environmental conditions.[94] Different types of stimuli were applied to induce responses, including the direct stimulants such as temperature, pH, and specific ions[3, 90-94], and newly emerged remote triggers such as light and electric and magnetic fields.[95-98] Magneto-responsive membranes have recently attracted particular attention, because of their remote controllability, rapid response and special potential for integration into microfluidic devices for analytical and drug delivery systems.[11, 95, 97, 136, 191, 192]

Some magneto-responsive membranes were realized by manipulating integrated magnetic nanoparticles with static or low-frequency magnetic fields in order to induce subtle changes of effective pore size, or to trigger cleaning and mixing effects.[192-194] Other types of magneto-responsive membranes addressing the switching of (selective) transport through barrier pores were prepared by combining a thermo-responsive polymer membrane and magnetic nanoparticles (MNPs) which release heat by high-frequency alternating magnetic field (AMF). The thermo-responsive part of the membrane works as an actuator and, potentially, as selective sieving medium and the MNPs act as localized heaters. Thus, Gajda and Ulbricht prepared magneto-responsive membranes by immobilizing the iron oxide MNPs on the pore walls of track-etched (TE) polyethylene terephthalate (PET) membranes with 700 nm diameter pore. The walls of TE PET membranes were functionalized with poly(N-isopropylacrylamide) (PNIPAm) via photo-initiated "grafting from" brush formation.[195] The membranes showed large and reversible changes of water permeability by switching the AMF on and off. Additional analyses had revealed that upon stimulation with the AMF ("on" state), the balance between the generated heat by the MNPs within the membrane pores and convective heat loss by the cold feed water lead to a local temperature above the lower critical solution temperature (LCST) of PNIPAm (32 °C), causing deswelling of the temperature-responsive polymer. However, because of the large membrane pore size, the membrane did not perform an interesting size selectivity.[195] Later, Qian et al. utilized surface-initiated atom transfer radical polymerization (ATRP) to graft PNIPAm from the pore walls of TE PET membranes (pore size also 700 nm), followed by conjugating iron oxide MNPs to the ends

of the grafted polymer chains. Although those membranes exhibited a size selectivity in polystyrene latex particles filtration which is adjustable by external AMF, successful selective separation was only limited to relatively large particles.[196]

Until now, as far as we know, only two types of magneto-responsive membranes with switchable nano-scale barrier pore size have been developed. One type is a magneto-hydrogel pore-filled membrane which is fabricated by post modification of TE PET membranes. The PNIPAm hydrogel network with entrapped iron oxide MNPs inside the PET membrane pores was prepared via *in situ* reactive pore-filling functionalization. The membranes were proven to have a good magneto-responsive molecular sieving performance during ultrafiltration; the rejection of 2000 kDa dextran was decreased from 94% to 30% when the AMF was turned on.[125] However, the membranes were obtained by a complicated preparation processes and the permeability was very low. The other type is a polyethersulfon-based mixed matrix membrane blended with prefabricated PNIPAm nanogel particles and iron oxide MNPs, fabricated by facile non-solvent induced phase separation (NIPS) process. The molecular weight cutoff (MWCO) of the obtained ultrafiltration membrane with quite high intrinsic permeability shifted from ~70 to 1750 kDa by switching on the AMF and returned to the initial value upon switching off the remote stimulation. However, because the PNIPAm shows an abrupt conformation change at the LCST (32 °C), the barrier pores of such PNIPAm-based magneto-responsive membranes can only be switched between two states, the off and on states of the AMF. Moreover, NIPAm monomer is suspected to be carcinogenic, which may hinder the transfer of PNIPAm-based membrane systems toward a technology breakthrough for controlled drug delivery devices in the human body.[41]

Poly(oligo(ethylene glycol) methyl ether methacrylate) ($PMEO_nMA$) is a newly emerged thermo-responsive polymer. The LCST of $PMEO_nMA$ can easily be tuned into the physiological temperature range (in particular by the average number of ethylene glycol repeating units in the side group, *n*) and it has very good biocompatibility.[43] In previous work, we prepared a novel thermo-responsive mesoporous membrane using poly(oligo(ethylene glycol) methyl ether methacrylate)-*block*-polystyrene-*block*-poly(oligo(ethylene glycol) methyl ether methacrylate) ($PMEO_nMA$-*b*-PS-*b*-$PMEO_nMA$). Formation of the mesoporous barrier layer with PS being the mechanically stable part of the matrix was driven by selective swelling of the $PMEO_nMA$ domains. $PMEO_nMA$ brushes on the pore walls underwent a gradual and reversible conformational change upon gradual variation of temperature, and thus tuned the barrier pore size of the resulting ultrafiltration membranes in a broad range of temperature around the LCSTs of the $PMEO_nMA$.[3]

The $PMEO_nMA$ containing triblock copolymers seemed to be perfect materials for preparation of magneto-responsive membranes which have finely controlled barrier pore sizes tuned by the external AMF. Therefore, in this study, we developed a new kind of magneto-responsive membranes, in which the pore size can be finely tuned through controlling the magnetic field amplitude of the external AMF. The

magneto-responsive thin-film mixed matrix nanocomposite membranes consist of a macroporous polyvinylidene fluoride support membrane and a thin mesoporous $PMEO_nMA$-*b*-PS-*b*-$PMEO_nMA$ film with embedded 30 nm iron oxide nanoparticles (IONPs). The loaded IONPs can generate heat upon stimulation with AMF so that the temperature of the membranes will increase when the AMF is applied, and the membrane will be cooled down by the convective flow of cold feed when the AMF is switched off. The heat generated by the IONPs is due to relaxation and hysteresis losses which are strongly related to the frequency and field amplitude of the AMF; therefore the temperature of membrane can be manipulated by applying AMF with different input energy. Because the $PMEO_nMA$ blocks on the pore walls can change their conformation gradually in a broad range of temperatures around their LCSTs, the pore size of membrane can be finely controllable within AMF.

4.2. EXPERIMENTAL SECTION

4.2.1. Materials

$PMEO_{2.2}MA$-*b*-PS-*b*-$PMEO_{2.2}MA$ (18,500-87,000-18,500 g/mol; M_w/M_n = 1.07) was synthesized by sequential anionic polymerization.[49] The $PMEO_{2.2}MA$ block is a random copolymer of di(ethylene glycol) methyl ether methacrylate (MEO_2MA) (80 mol%) and tri(ethylene glycol) methyl ether methacrylate (MEO_3MA) (20 mol%). Oleic acid coated iron oxide nanoparticles (IONPs, 30 nm diameter) in chloroform dispersion (Fe concentration 25 mg/mL) were purchased from Ocean NanoTech (USA). Commercial polyvinylidene fluoride (PVDF) macroporous membrane discs (diameter 2.5 cm) with a nominal pore diameter of 220 nm (Millipore, USA) were used as the support membrane.

4.2.2 Membrane preparation

The membrane preparation method was described in detail in our previous work.[3] PVDF membrane discs, used as support layers, were submerged in deionized water for several hours. Then, the solutions consisting of $PMEO_{2.2}MA$-*b*-PS-*b*-$PMEO_{2.2}MA$ (BCP) and different fractions of IONPs were spin-coated onto the surface of water-prefilled PVDF membrane discs at 3000 rpm for 10 s, followed by vacuum drying at room temperature overnight. The membranes were heated to 130 °C for 10 min for enhancing the adhesion between the BCP-IONPs layer and the PVDF surface. Then the mesopores were introduced into BCP-IONPs layer by using the methanol-scCO_2 swelling method, which had been described in our previous articles.[168, 170-173, 178] In this work, the BCP-IONP coated PVDF membranes and methanol were loaded into the high-pressure vessel which was kept at 45 °C, and then filled with 200 bar CO_2 for selectively swelling the $PMEO_nMA$ domains of BCP. In the supercritical state, the mole fraction of CO_2 in the thus obtained

methanol-CO_2 mixture was estimated as 0.89, and therefore methanol and CO_2 were able to form a homogeneous phase.[184] After 30 min swelling, the pressure was released at a rate of 5 bar/min. All the prepared membranes were cut into 13 mm diameter discs and stored in deionized water.

Five different BCP-IONPs membranes were prepared by spin-casting the $PMEO_{2.2}MA$-*b*-PS-*b*-$PMEO_{2.2}MA$ and IONPs chloroform mixture at different mass ratio. The purchased 25 mg/ml IONPs dispersion was diluted into 1 mg/mL, 5 mg/mL and 10 mg/mL with chloroform. Then, $PMEO_{2.2}MA$-*b*-PS-*b*-$PMEO_{2.2}MA$ was dissolved in the diluted IONPs dispersion at a concentration of 60 mg/ml. Figure 4.1 shows the visual inspection of membranes with 0 mg/mL (BM), 1 mg/mL (1CS), 5 mg/mL (5CS), 5 mg/mL (5CL) and 10 mg/mL (10CL) IONP loading. The spin-cast solutions of 1CS and 5CS stood for 5 min after adding $PMEO_{2.2}MA$-*b*-PS-*b*-$PMEO_{2.2}MA$ in the diluted IONPs dispersions before spin-casting. The solutions for 5CL and 10CL stood much longer, about 20 min. Although 5CS and 5CL were prepared with the same amount of IONPs in the solutions, the colors of the membranes were different. The 5CS membrane was brown but 5CL was grayish. It can be explained by the stronger aggregation of IONPs in 5CL spin-cast solution caused by prolonged standing time (for more detailed discussion see Section 4.3.2).

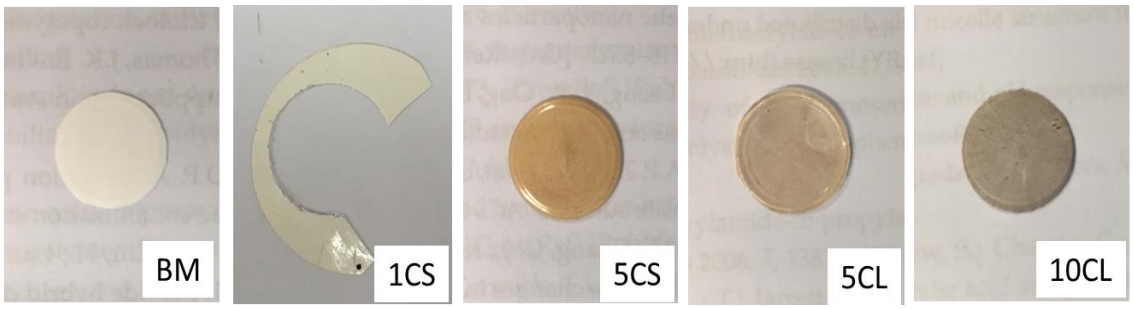

Figure 4.1. Digital photographs of the BCP thin-film composite membranes without (BM) and with immobilized IONPs (CS or CL; number stands for IONP concentration; S and L stand for short and long time, respectively, between solution preparation and casting). The image of 1CS is the residual of the bigger membrane sample obtained directly after preparation; the other samples had been used for ultrafiltration tests.

4.2.3. Evaluation of the IONPs heating effect by calorimetric method

A Truheat HF series 5010 generator (Trumpf Hüttinger, Germany) with sandwich copper tube coils was employed in this study to generate AMF at a frequency of 745 kHz. The 10 ºC cooling water within external circuit constantly flowed through the lumen of the copper tube during the operation. The AMF conditions had been thoroughly investigated by Lin et al.[125] Between the inductor coils, the magnetic field distribution

was uneven. The field amplitude in the center of sandwich coils was in good linear relationship with input current but not dependent of the field frequency. The relationship of field amplitude (H, kA/m) and current (I, A) was H = 1.861 * I. That had been investigated by measuring the field strength in the center of the sandwich coils for varied input frequency and current; the details are shown in Supporting Information (S4.1).[197]

The heating effect of IONPs in chloroform dispersion was evaluated by using calorimetric method.[125] A volume of 1 mL of 0.5 mg/mL IONPs chloroform dispersion was loaded in a homemade closed glass vial with vacuum walls, and then the vial was mounted between the inductor coils. The solution temperature was measured before and after 1 min AMF exposure. To exclude the influence of AMF generated non-specific heat, analogous experiments were performed with 1 mL chloroform treated as background solvent. The specific loss power (SLP) of IONPs was calculated as follows:[198]

$$SLP\ (\mathrm{W} \cdot g^{-1}) = c\ \frac{m_s}{m_{Fe}}\left(\frac{\Delta T_s - \Delta T_c}{\Delta t}\right) \tag{4.1}$$

where c is the heat capacity of water, m_s is the mass of the sample, m_{Fe} is the mass of IONPs in the sample, ΔT_s is the temperature increase of the IONPs dispersion, ΔT_c is the temperature increase of chloroform, and Δt is time duration with AMF.

4.2.4. Scanning electron microscopy (SEM) investigation

To observe the morphological features of membranes and to visualize the loading with IONPs, the instrument ESEM Quanta 400 FEG (FEI Co., Hillsboro, USA) with backscattered electron detector was used. Samples were frozen in liquid nitrogen for 2 to 3 minutes, followed by fracturing. Both outer surface and cross-section of samples were sputtered with 5 nm thin palladium layer using K550 sputter coater from Emitech Ltd. (Ashford, U.K).

4.2.5. Thermo- and magneto-responsive water permeability

The thermo-responsive water permeabilities of the BCP-IONPs membranes were measured using Millipore Swinnex filter holder (diameter 13 mm, USA) at 10-45 °C (5°C interval for each measurement). The coated side faced the feed solution and effective membrane area was 0.7 cm^2. A thermostat (Julabo, Germany) with external circuit was used to adjust the operating temperature and the transmembrane

pressure was controlled by Argon gas pressure. Filtrate samples were collected every 5 minutes and weighed. Water flux (J) and permeability (P) were determined accordingly:[179]

$$J\ (kg \cdot h^{-1} \cdot m^{-2}) = \frac{m_f}{A \times \Delta t} \tag{4.2}$$

$$P\ (kg \cdot h^{-1} \cdot m^{-2} \cdot bar^{-1}) = \frac{J}{\Delta p} \tag{4.3}$$

where m_f represents the weight of the filtrate, A is the effective membrane area, Δt is the filtration time, and Δp is the transmembrane pressure.

The magneto-responsive water permeabilities of the BCP-IONPs membranes were studied using a homemade filtration setup as shown in Figure 4.2. The filtration cell was always placed in the middle of the inductor coils because of the uneven magnetic field distribution (cf. Section 4.2.3). To keep the operating temperature at ~15 ºC which is lower than the LCST of $PMEO_{2.2}MA$ (32 ºC), the feed solution reservoir was immersed in 15 ºC water bath, and the filtration cell and AMF coils were placed in the chamber of hood with 15 ºC circulating water in the lumen. Moreover, insulating foam covered the tube to prevent heat transfer during the feed solution transfer from the reservoir to the filtration cell. Note that the actual temperature of the filtration cell might be little higher or lower than 15 °C, because the filtration system would not completely isolated from the environment. During filtration runs, the AMF was kept at off state for 15 minutes; then it was switched on for 30 minutes and thereafter turned off for 20 minutes. The water flux was monitored by weighting filtrate samples every 5 minutes and calculating according to equation (4.2).

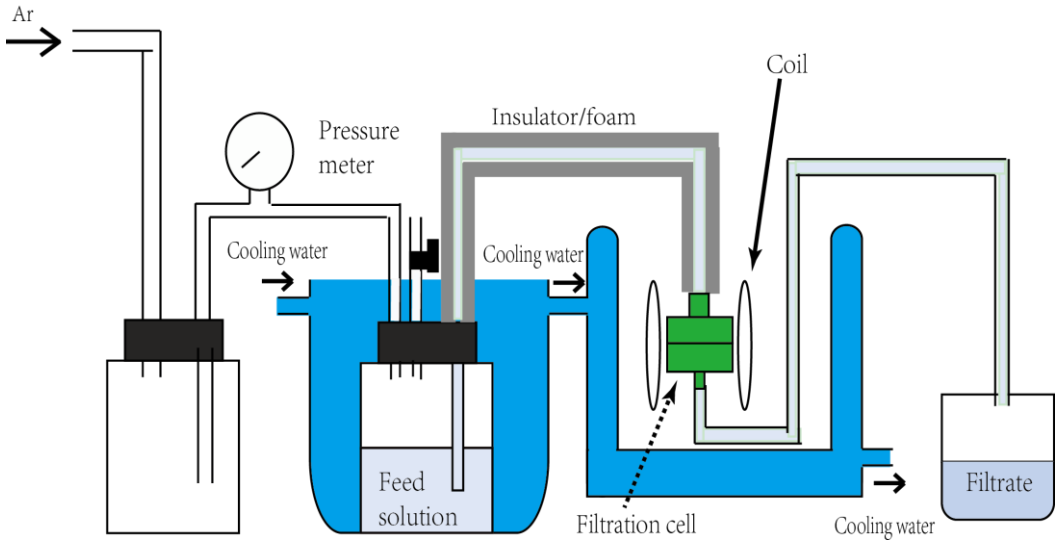

Figure 4.2. The home-made AMF filtration setup for investigating the magneto-responsivity of the membranes.

4.2.6. Thermo- and magneto-responsive molecular sieving performance

The thermo-responsive sieving characteristics of the membranes were investigated by dextran ultrafiltration at 10 ºC, 30 ºC and 50 ºC with same type of filter holder used in water permeability measurements (cf. Section 4.2.5). The aqueous feed solution contained 0.5 g/L of 35 kDa dextran (Serva, Germany) and 0.5 g/L of 2000 kDa dextran (Sigma-Aldrich). High-performance gel permeation chromatography (HP-GPC) with two SUPREMA columns (linear, 10 µm, 8 x 300 mm, calibrated from 100 to 100,000,000 g/mol with dextran), water with 0.01 M NaN_3 at a flow rate of 1 mL/min at 45 ºC as eluent, the RI-101 differential refractive index detector (Shodex Showa Denko K.K., Tokyo, Japan) and the software Win GPC Unity from PSS (Polymer Standards Service GmbH, Germany) was used to analyze the compositions and concentrations of feed and filtrates. The rejection coefficient (R) for each dextran molecular weight was calculated as follows:[182]

$$R = 1 - \frac{C_{\text{filtrate}}}{C_{\text{feed}}} \tag{4.4}$$

where C_{filtrate} and C_{feed} are the dextran concentrations of the filtrate and feed, respectively, determined by the peak height of the elution curves.

The magneto-responsive dextran ultrafiltration was studied using the setup shown in Figure 4.2. The filtrate samples were first taken when the AMF was off, then when the AMF was on. The compositions and concentrations of feed and filtrates were also analyzed by HP-GPC and the rejections were calculated using equation (4.4). To minimize the fouling effects in subsequent tests, the used membranes were washed with 50 ºC water for 1 hour and for more than 5 hours at room temperature water. The room temperature water was changed for 3 times during the washing. Water flux tests to assess fouling were carried out before and after dextran ultrafiltration including washing as described above.

4.3. RESULTS AND DISCUSSION

4.3.1. Heating efficiency of IONPs dispersion

The heat generation of the IONPs with AMF was investigated by the calorimetric method and the obtained data are shown in Table 4.1. With a fixed input frequency and different currents (I), the magnetic field amplitude (H) in the center of sandwich coils was different and was calculated using the relationship

H = 1.861 * I (cf. Section 4.2.3). The temperature of chloroform without any IONPs only slightly increased as the input current increased because of the higher non-specific heat generation with larger input energy. At the same field amplitude, the temperature changes of IONPs dispersions in chloroform were much larger than those for pure chloroform due to the specific heat generated by the IONPs. The SLP of IONPs increased with higher H; this correlates well with other reports that the magnetic heating is an increasing function of frequency and field amplitude.[199] The SLP of the IONPs used in this study was quite high which was in accordance to the other data for the same kind of materials (for instance, SLP = 670 W/g had been measured for 40 nm large IONP from the same manufacturer at the same field strength of 20 kA/m, with the twofold higher absolute value than in this work caused by the larger particle diameter). Therefore, it was expected that the IONPs embedded in the block copolymer porous top layer of composite membrane may provide enough heat at relatively small loading amount, thus significantly and rapidly increasing the temperature of the very thin BCP film without disturbing the membrane's pore structure. Because the applied AMF frequency was too high to allow the IONPs to follow the external field, the Brownian relaxation (physical rotation of the whole particle within the dispersing medium) would not contribute to the heat release.[194, 199] Hysteresis loss (the magnitude represented by the area inside the hysteresis loop) and Neel relaxation (rotation of the magnetic moment within the particle) were therefore the main sources of the heating of IONPs.[136] Of course, the same behavior was expected for the IONPs immobilized in the BCP film of the composite membrane.

Table 4.1. Specific loss power (SLP) of chloroform and IONPs (30 nm diameter) dispersions in chloroform upon AMF excitation at fixed frequency (745 kHz).

I (A)	H (kA/m)	Chloroform	IONP in chloroform	SLP (W/g)
		ΔT_c (ºC)	ΔT_s (ºC)	
8.0	14.9	0.8	4.1	157
10.7	20.0	1.2	8.8	363
13.4	24.9	1.8	15.4	649
15.6	29.0	2.3	19.1	801

4.3.2. Morphology of the BCP-IONPs thin-film composite membranes

To clarify the morphological features of the membranes with and without the IONPs, the SEM images for the cross-section of composite membranes (Figure 4.3, a1-5) and the top surface of BCP-IONPs films (Figure 4.3, b1-5) were taken. All the membranes have two-layered composite structure with mesoporous top layers and macroporous PVDF supporting layers. The BM membrane which was prepared without IONPs showed the same morphology as observed in our previous work.[3] For the 1CS, 5CS, 5CL and 10CL membranes, the bright spots or clusters which originated from the loaded IONPs could be clearly observed in the cross-section images a2-5 and top-view images b2-5 (Figure 4.3). Based on the analysis of the cross-section images, the thickness of the barrier layer of the different composite membranes was almost same, i.e. 1.8 µm (BM), 1.6 µm (1CS), 1.5 µm (5CS), 2.3 µm (5CL) and 2.0 µm (10CL). This suggests that the nanoparticle loading does not affect the thickness of the block copolymer top layers much. In the SEM images, the change of porosity in the top layer of the membrane was hardly observed after adding IONPs, indicating that the embedded IONPs did not have any influence on the barrier pore size. The small and relatively even barrier pore size (about 50 nm) ensured that the BCP-IONPs membranes could be used for the ultrafiltration separation based on differences in nano-scale molecular size (cf. Section 4.3.4). Note that there was no defect or pinhole observed in the BCP top layers in all the composite membranes, and this was also proved by the relatively low and reproducible water permeability data for all the membranes (cf. Section 4.3.3).

The bright spots in the 1CS and 5CS membranes had a round shape and were about 100~500 nm large. This size was much bigger than the diameter of a single IONP (30 nm), suggesting that aggregation of IONPs occurred during the membrane preparation processes. Comparing the top-view images of the 1CS and 5CS membranes, the density of bright spots in the membrane was very much increased with 5 fold higher loading of IONPs, but the size of the spots still stayed at the same level (Figure 4.3, b2-3). Unlike the relatively small round IONPs clusters in the 1CS and 5CS membranes, the IONPs clusters in the 5CL and 10CL membranes had random shape and were overall of much bigger size (0.6-1 µm). This might be because of the longer standing time of the casting solutions for the 5CL and 10CL membranes which lead to a stronger IONPs aggregation. The different color of the 5CS and 5CL membranes which had the same overall loading of IONPs (Figure 4.1) could also be explained by the same reason. The commercial 25mg/mL IONPs in chloroform solution were stabilized by oleic acid loaded on the surface of IONPs. When the commercial 25 mg/mL IOPN dispersion was diluted (down to 10 or 1 mg/mL), a fraction of oleic acid might be removed from the IONPs surface. Exposed hydroxyl groups on the IONPs surface might then interact with one another or with $PMEO_{2.2}MA$ blocks in the BCP leading to IONPs aggregation in particular for longer standing time. In Figure 4.3b5, the areal fraction of bright parts in the 10CL membrane top-view image was higher compared to the 5CL membrane, because of the increased concentration of IONPs of 10CL spin-casting solution. One could speculate that the strongly aggregated IONPs might cause large

local heat and therefore higher temperature around the IONPs clusters than in other remote parts; therefore the pore open states of 5CL and 10CL membranes upon AMF excitation might be locally different.

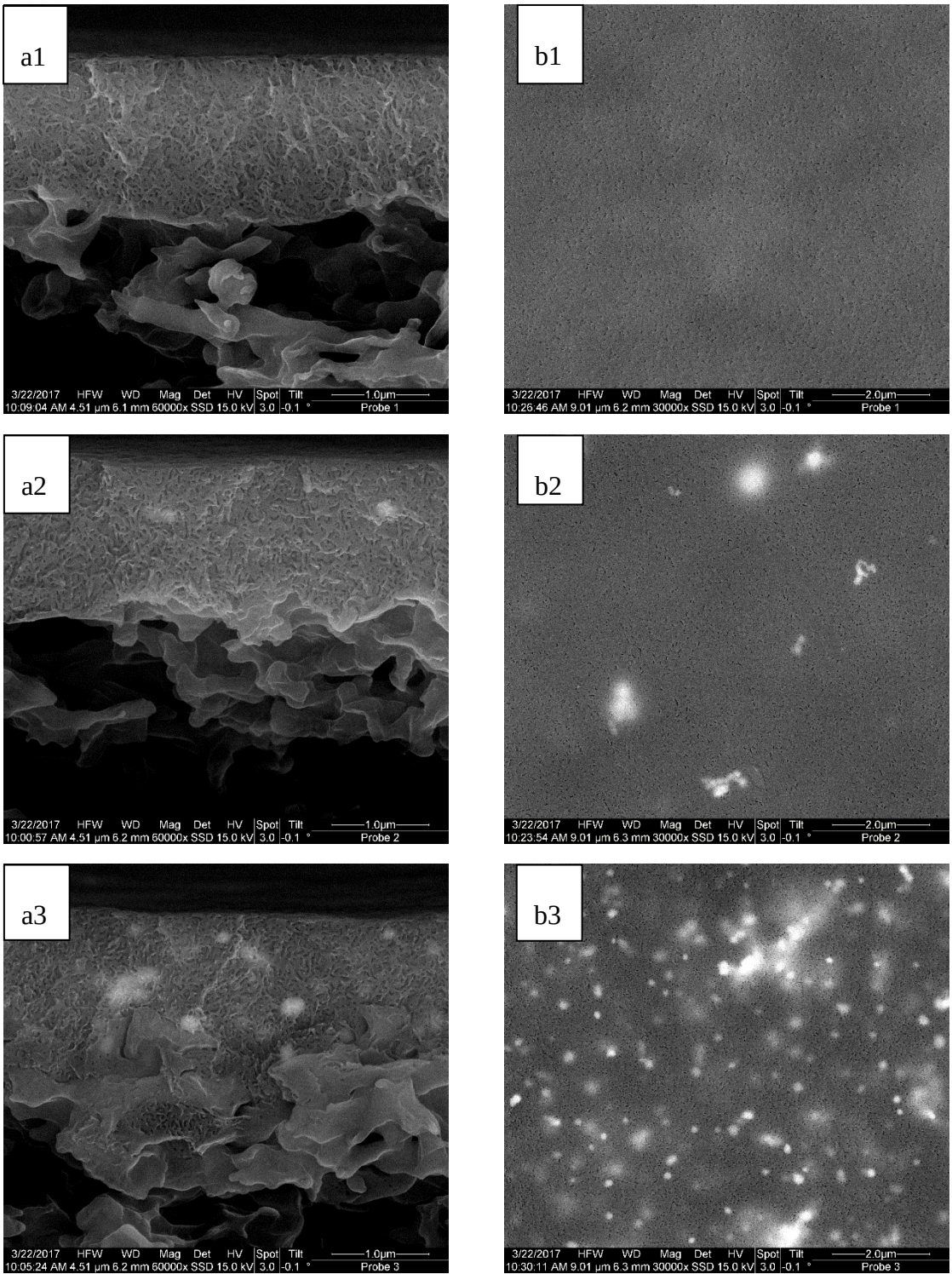

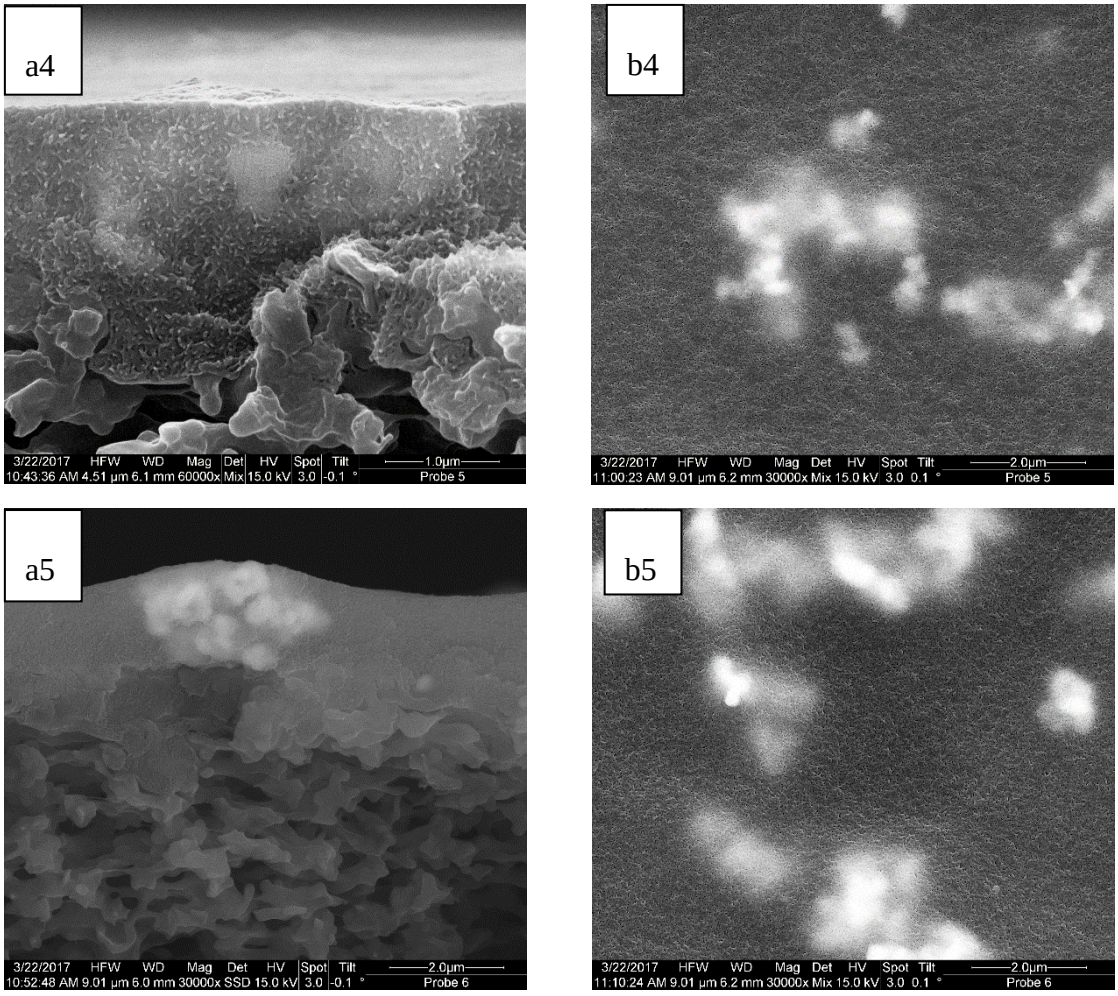

Figure 4.3. SEM images of cross-sectional view of (a1) BM, (a2) 1CS, (a3) 5CS, (a4) 5CL, (a5) 10CL membranes and SEM images of top view of (b1) BM, (b2) 1CS, (b3) 5CS, (b4) 5CL, (b5) 10CL membranes. Note that "S" indicates short and "L" longer time before solution/dispersion had been used for spin-casting. The scale bars in (a1-4) correspond to 1 µm, and the scale bars in (a5, b1-5) correspond to 2 µm.

4.3.3. Thermo- and magneto-responsive water permeability of the BCP-IONPs membranes

Figure 4.4 shows the water permeability of the membranes BM, 5CS and 5CL at different temperature from 10 ºC to 45 ºC. For each membrane, water permeability increased with increasing temperature, suggesting that the barrier pore size of the membranes was tuned by temperature, *i.e.* all the membranes had a good thermo-responsivity. The increase of the water permeability of the BCP-IONPs containing membranes (5CS and 5CL) with increasing temperature was lower than that for the BM membrane. Among the three membranes, the water permeabilities as well as the slope of water permeability as a function of

temperature of the 5CL membrane were the lowest. The permeability ratios at 45 °C and 15 °C for the BM, 5CS and 5CL membranes were 6.7, 5.0, and 3.6, respectively (Table 4.2). Based on the SEM images (Figure 4.3), the differences between the membranes with and without IONPs could possibly be explained by blockage of membrane pores by the IONPs clusters. However, because of the stronger aggregation of IONPs in the 5CL membrane, the diameter of IONPs clusters in those membranes was as big as the thickness of the block copolymer top layer. Hence, only pores in the parts without IONPs clusters showed the thermal response. In contrast, for the 5CS membrane, the IONPs clusters were much smaller and uniformly distributed so that the water flow through the channels was more effective.

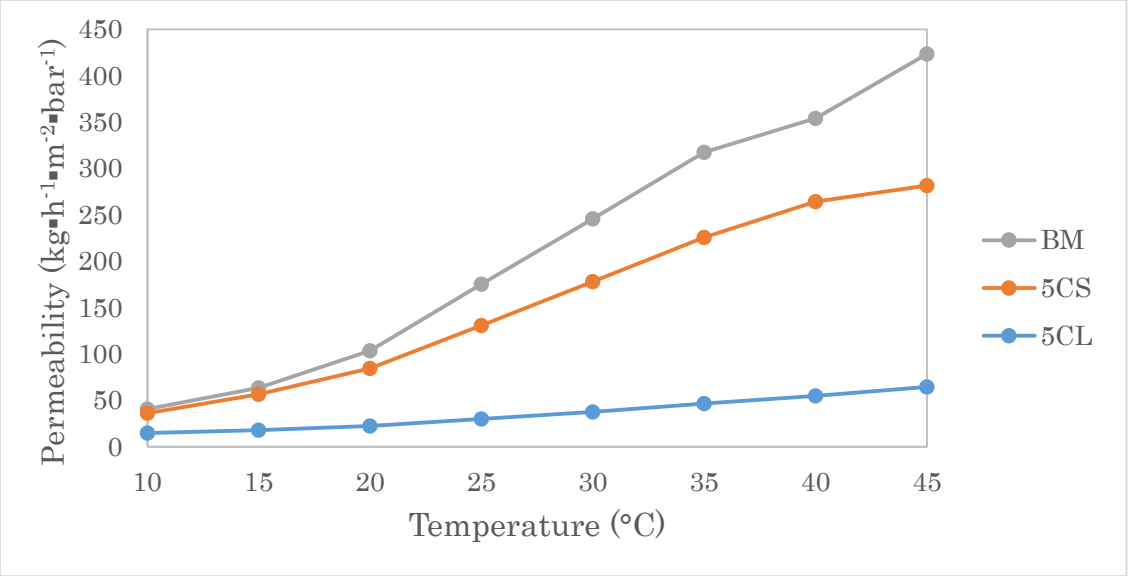

Figure 4.4. Water permeability versus temperature of the BM, 5CS and 5CL membranes. The transmembrane pressures for measuring the fluxes were 0.2 bar for BM membrane, 1.0 bar for 5CS membrane and 1.8 bar for 5CL membrane.

To investigate the magneto-responsive behavior, the water fluxes of the BM, 1CS, 5CS, 5CL and 10CL membranes were measured without and with the magnetic field with a frequency of 745 kHz and a current of 15.6 A (resulting field amplitude at center of coils was about 29 kA/m; cf. Figure 4.2). Figure 4.5 shows the water flux changes of the BM, 1CS and 5CS membranes when the external AMF was switched on and then off. It should be noted that the non-specific heating had its impact predominately on the feed liquid and the membrane within the membrane module which had been surrounded by the inductor coils, while the temperature in the feed reservoir was kept constant by a thermostat and insulating material around the tube to the module (cf. Fig. 4.2); that this is the case is confirmed by the clear impact of flux (convective cooling by feed liquid) on the effects of heating. Three levels of transmembrane pressures were chosen, so that the flux measurements for the three membranes were performed with 3 initial water fluxes, *i.e.* at ~15 $kg▪m^{-2}▪h^{-1}$ (“low”), ~40 $kg▪m^{-2}▪h^{-1}$ (“middle”) and ~190 $kg▪m^{-2}▪h^{-1}$ (“high”). This corresponds to different

magnitudes of convective cooling (low, middle, high).[195] During the first 15 minutes, the AMF was off. After the AMF was turned on, the water fluxes of both, reference membrane (BM) and BCP-IONPs membranes (1CS and 5CS), were increased and reached a plateau within 10 minutes. The flux plateau indicates the stationary state balanced by the heats generated by AMF and removed by convective flow of the feed (about 15 °C) through the pores. After switching off the AMF, the water flux returned to the same values as at the beginning of the experiments. This performance indicates that phase transition of the thermo-responsive polymer brushes in all the membranes (with or without IONPs) occurred. One might distinguish between the rate of response, i.e. the response time and rate of flux change, and the magnitude of response, i.e. the stationary flux achieved after switching on or off the AMF. One may expect some difference in response time between specific and non-specific heating, but with the used systems, this is complicated to analyze and no such attempt had been made here. However, the magnitude of the response is much more relevant when aiming at membranes with barrier properties which are tunable by alternating magnetic field stimulation. Indeed, the 5CS membrane showed higher water flux than the BM membrane with the AMF on, *i.e.* (ΔJ_{5CS}-ΔJ_{BM}) values were positive (cf. Table 4.2). This suggests that the temperature of the 5CS membrane was higher than that of the BM membrane and the thermo-responsive brushes on the pore walls of 5CS membrane were de-swollen to a higher degree.

Moreover, with the higher initial flux, the (ΔJ_{5CS}-ΔJ_{BM}) values became even larger. The increase in water flux of BM membrane during the AMF operation time was caused by the non-specific heat from the magnetic field inductor. Because at higher initial flux convective cooling was more efficient, the relative increase in flux upon switching on AMF decreased ($\Delta J/J_{off}$ was ~1.9 for low, ~1.3 for medium and ~0.6 for high fluxes). However, for the 5CS membrane, both non-specific heat from outside the filtration cell and heat generated inside the membrane by the IONPs, lead to the water flux increase upon switching on the AMF ($\Delta J/J_{off}$ was ~2.0 for low, ~1.7 for medium and ~0.9 for high fluxes). The additional increase compared to membrane BM can be attributed to the effect of the embedded IONPs. In contrast, 1CS membrane did not show the magneto-responsivity, i.e. the (ΔJ_{1CS}-ΔJ_{BM}) data were negative at very low absolute values (cf. Figure 4.5 and Supporting Information Table S4.1). This was probably because the amount of loaded IONPs in 1CS membrane was too low to generate enough specific heat. The morphology differences between the 1CS and BM membranes could also contribute to the observed effects, especially the negative values (apparently less response to AMF for the membrane containing IONPs).

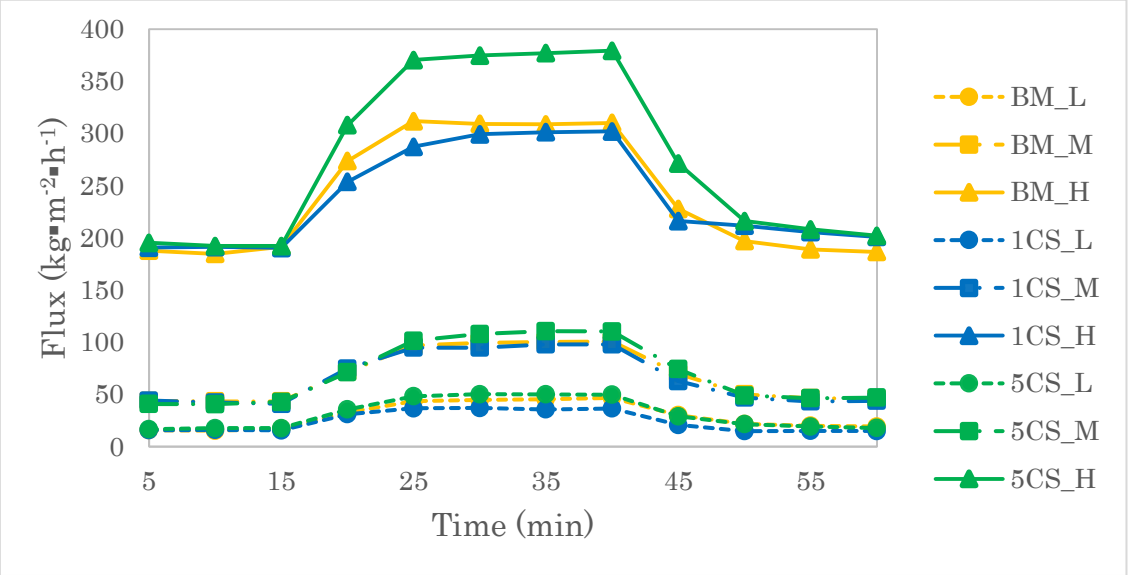

Figure 4.5. Water fluxes through the BM, 1CS and 5CS membranes without and with AMF observed at low (L), middle (M) and high (H) initial fluxes; feed temperature fixed at ~15°C.

Figure 4.6 shows the water flux of the BM, 5CL and 10CL membranes with and without the AMF. The flux measurements were also performed with different initial water fluxes (at ~15 kg▪m^{-2}▪h^{-1} and ~40 kg▪m^{-2}▪h^{-1}). The 5CL membrane exhibited much higher water flux than the BM membrane upon switching on AMF at low initial flux. By increasing the initial flux to ~40 kg▪m^{-2}▪h^{-1} (middle), the flux difference between 5CL and BM membranes became even bigger. The 5CS and 5CL membranes had been prepared with a same loading of IONPs. However, the magneto-responsive properties indicated by water flux were much different, i.e. (ΔJ_{5CL}-ΔJ_{BM}) data reached a relatively high value even with low initial water flux, while (ΔJ_{5CS}-ΔJ_{BM}) was small unless the initial flux had been increased to ~190 kg▪m^{-2}▪h^{-1} (cf. Table 4.2). Unlike the small size IONPs clusters which were finely dispersed in the 5CS membrane, the strongly aggregated IONPs in the 5CL membrane generated larger heat in smaller volume. Hence, the thermo-responsive polymer brushes on the pore walls which are located around the big IONPs clusters might be exposed to much higher local temperature; therefore pores were open more widely than pores in other parts which were mainly influenced by non-specific heat. The fraction of more widely opened pores in membrane 5CL will lead to an over-proportional increase of flux, at the same pressure according to Hagen-Poiseuille model proportional to pore radius to the power of 4, compared to membrane 5CS where the changes of pore size are more evenly distributed and smaller. The magneto-responsive performance of the 10CL membrane is shown in Figure 4.6 and Supporting Information, Table S4.2. With the AMF, the water flux of the 10CL membranes was almost the same as that for BM membrane when the initial flux was low. When the initial flux was set to middle level, the (ΔJ_{10CL}-ΔJ_{BM}) value became higher but still much smaller than the (ΔJ_{5CL}-ΔJ_{BM}) value. This may be because the too large amount of loaded IONPs occupied too much of the membrane barrier layer so that the effective porous area became too small to show the water flux increase,

even when all the through-pores were open upon stimulation by the AMF. In summary, for too low loading with IONPs, the specific local heating in the membrane is too small compared to nonspecific heating of the system, and for low initial flux the convective cooling of the membrane by the feed flow is low so that effects of non-specific heating (compared to membranes without IONPs) can only be observed at higher flux through the membrane. At the same nominal loading, more clustered IONPs show larger effect toward switching pore size, too high loading reduced switching efficiency.

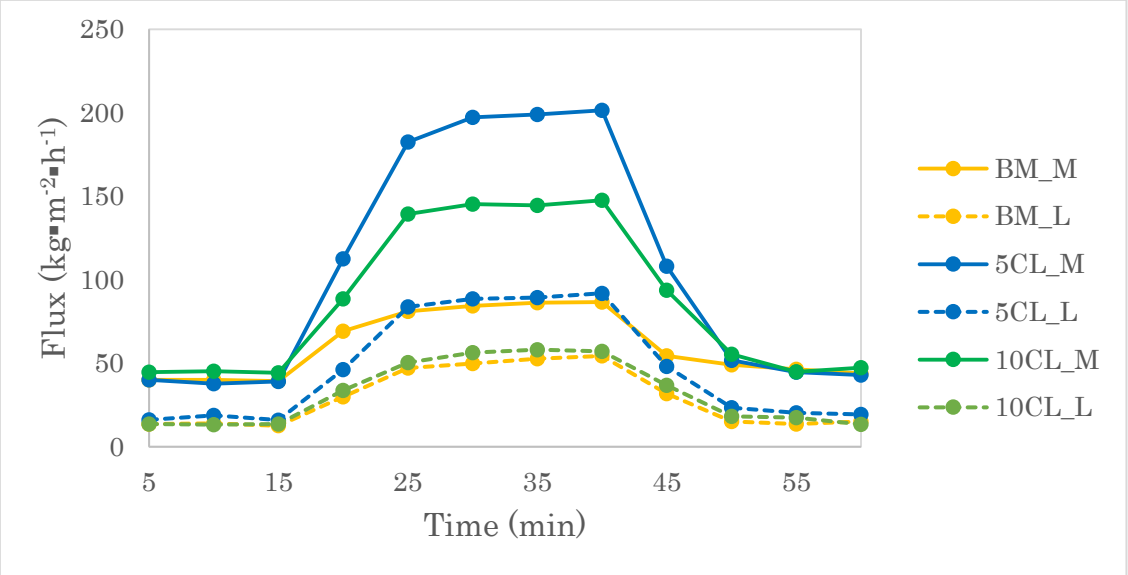

Figure 4.6. Water flux change of the BM, 5CL and 10CL membranes without and with the AMF performed at low (L) and middle (M) initial flux; feed temperature fixed at ~15°C.

Table 4.2. Water flux (kg▪m^{-2}▪h^{-1}), permeability (kg▪m^{-2}▪h^{-1}▪bar^{-1}) and rejection coefficients for 500 kDa dextrane of the membranes BM vs. 5CS and BM' vs. 5CL. BM and BM' were reference membranes without IONPs and had been prepared with the same method under identical conditions as their IONPs containing counterparts 5C and 5CL, respectively.

Membrane		BM	5CS	BM'	5CL
Water permeability at	$P_{15\,°C}$	63.4	56.5	-	17.8
	$P_{45\,°C}$	423.4	281.6	-	64.5

15 °C and 45 °C	$P_{45\,°C}/P_{15\,°C}$	6.7		5.0		-		3.6	
Water fluxes with/without AMF[a]	*Initial flux (pressure)*	M	H	M	H	L	M	L	M
	J_{off}	43.7	187.7	40.8	195.3	13.5	39.9	16.1	40.1
	J_{on}	100.3	308.7	110.6	377.0	52.6	86.2	89.3	199.0
	$\Delta J = J_{on} - J_{off}$	56.6	121.0	69.8	181.7	39.1	46.3	73.2	158.9
	$\Delta J / J_{off}$	1.3	0.6	1.7	0.9	2.9	1.2	4.6	4.0
	ΔJ_{5CX}-ΔJ_{BM}[b]	-	-	13.2	60.7	-	-	34.1	112.6
Rejections for 500 kDa dextran with/without AMF or at different temperatures[a]	*Initial flux (pressure)*	H				M			
	$R_{0kA/m}$	0.40		0.62		0.70		0.63	
	$R_{29kA/m}$	0.32		0.27		0.52		0.42	
	$R_{10°C}$	-		0.64		-		0.93	
	$R_{50°C}$	-		0.27		-		0.31	

[a] L represents the low level for initial flux (~15 kg▪m^{-2}▪h^{-1}); M represents the middle level for initial flux (~40 kg▪m^{-2}▪h^{-1}); H represents the high level for initial flux (~190 kg▪m^{-2}▪h^{-1}).

[b] ΔJ_{5CX} or ΔJ_{BM} represent the changes of flux upon switching on the AMF (ΔJ) for a particular membrane (either 5CS or 5CL, or BM).

As it was observed in our previous work, the thermo-responsive performance of $PMEO_{2.2}MA$-*b*-PS-*b*-$PMEO_{2.2}MA$-based membrane was quite different from those of typical PNIPAm-based membranes that alter their pore size abruptly around 32 °C (LCST of PNIPAm). The swelling/deswelling transition of the $PMEO_{2.2}MA$ chains on the membrane occurred almost continuously with temperature in the vicinity of its LCST (cf. Figure 4.4).[3] Therefore, we expected that by adjusting the input energy of external AMF, the BCP-IONPs membranes could reach different distinct temperatures and therefore the pore size could be tuned into any diameter between complete open and closed states. We performed the water flux measurements with BM, 5CS and 5CL membranes with magnetic field amplitudes of 15 kA/m, 20 kA/m, 25 kA/m and 29 kA/m. Because the 5CS membrane only could show its pronounced magneto-responsive performance with high transmembrane pressure (cf. Figure 4.5), but middle level transmembrane pressure was enough for the 5CL membrane to exhibit its magneto-responsivity (cf. Figure 4.6), we chose the initial fluxes ~190 $kg{\cdot}m^{-2}{\cdot}h^{-1}$ for the 5CS membrane and ~40 $kg{\cdot}m^{-2}{\cdot}h^{-1}$ for the 5CL membrane. Table 4.3 shows water flux values for the BM membrane (J_{BM} and J'_{BM}), 5CS membrane (J_{5CS}) and 5CL membrane (J_{5CL}) when the AMF was on. The water flux curves of the BM, 5CS and 5CL membranes as a function of time can be found in the Supporting Information (Figure S4.2). The J_{5CS} and J_{5CL} values increased with increasing magnetic field amplitude (*H*), because higher amplitude causes larger heat generated by the IONPs (cf. Table 4.1), leading to a higher temperature of the 5CS and 5CL membranes, thus switching the pores to more open states. This observed performance indicated that the pore size of the BCP-IONPs membrane could be tuned by the external AMF. The water flux of the membrane without IONPs (J_{BM} and J'_{BM}) also increased with an increasing *H* due to the increased non-specific heat from the coils with more input energy; however, the water fluxes of the membranes with IONPs were much higher than that without IONPs at the same condition. The difference between the water fluxes for membranes with and without IONPs was more pronounced with higher field amplitude. All data suggest that the immobilized IONPs provided more additional heat when the field strength is step-wise increased and that this leads to step-wise higher local temperatures in the membrane and consequently step-wise larger effective pore sizes.

Table 4.3. Water fluxes for the BM, 5CS and 5CL membranes with different magnetic field amplitudes (the frequency was kept at 745 kHz; the current was set to values of 8.0 A, 10.7 A, 13.4 A, and 15.6 A; the unit of all the water fluxes is $kg{\cdot}m^{-2}{\cdot}h^{-1}$).

H (kA/m)	Initial flux ~190 $kg{\cdot}m^{-2}{\cdot}h^{-1}$			Initial flux ~40 $kg{\cdot}m^{-2}{\cdot}h^{-1}$		
	J_{BM}	J_{5CS}	$(J_{5CS} - J_{BM})^a$	J'_{BM}	J_{5CL}	$(J_{5CL} - J'_{BM})^a$

15	245.5	253.7	8.2	55.7	77.7	21.9
20	268.1	285.1	17.0	67.0	113.0	45.9
25	300.5	331.0	30.5	79.5	157.7	78.2
29	308.7	377.0	68.2	92.1	199.0	107.0

[a] Difference between flux values for BCP-IONPs membrane (5CS or 5CL) and BCP membrane (BM) at same initial flux.

4.3.4. Thermo- and magneto-responsive molecular sieving performance of the BCP-IONPs membranes

The magneto-responsive molecular sieving performances of the BM, 5CS and 5CL membranes were investigated by ultrafiltration of a dextran solution without and with the AMF at different magnetic field amplitudes. Because of the small deviation between individual membrane samples, performances of the two reference membranes (BM vs. BM') had a small difference. The dextran has a rather broad molecular weight distribution well covering the hydrodynamic diameter range corresponding to the pore diameters of the membranes used in this study. Figure 4.7a and 4.7b show the dextran rejection curves without and with the AMF at different amplitude. The rejection coefficients for 500 kDa dextran are shown in the Table 4.2.

Based on the results of water permeability, transmembrane pressures of 0.75 bar and 1.9 bar were chosen for BM membrane and 5CS membrane, respectively, so that the initial water flux of these two membranes was adjusted to the same level (193 $kg \cdot m^{-2} \cdot h^{-1}$). The flux results for water and dextran solutions as feed are shown in the Supporting Information (Figure S4.2a). In Figure 4.7a, molecular sieving behavior of BM and 5CS membranes was different without AMF because of the small difference in pore structures of those two membranes resulting in the different membrane permeability (cf. Table 4.2). The BM membrane with higher water permeability had also a somewhat higher molecular weight cut-off. When the AMF was turned on, the rejection coefficients for both membranes decreased, but the downward shift for the 5CS membrane was much larger than for the BM membrane. Without AMF, i.e. at low temperature, the thermo-responsive polymer chains on the pore walls of both membranes were swollen and the membranes were at the closed state. With the AMF on, the non-specific heat that came from the coils increased the temperature of the BM membrane, so that the pores in this membrane were opened to a certain degree. But for the 5CS membrane, in addition to the non-specific heat from outside, the heat was also generated by the embedded IONPs (cf.

Section 4.3.3). The additional heat yielded a higher temperature for 5CS membrane, therefore the effective barrier pore size increased to a larger extend, as clearly indicated by the much lower dextran rejection compared to the state without remote stimulation.

For the BM' and 5CL membranes, the AMF with magnetic field amplitude at 0 kA/m, 20 kA/m and 29 kA/m were applied (Figure 4.7b). The initial water flux was about 43 $kg \cdot m^{-2} \cdot h^{-1}$. The flux results with water and dextran solution as feed for the BM' and 5CL membranes are shown in the Supporting Information (Figure S4.2b). Analogous to behavior of BM and 5CS membranes, the rejection of BM' and 5CL membranes also dropped as the AMF was switched on but the 5CS membrane had a larger decrease. The ($R_{29kA/m}$ - $R_{0kA/m}$) was 0.36 for the 5CS membrane and 0.21 for the 5CL membrane (cf. Table 4.2). With an increased magnetic field amplitude (from 20 kA/m to 29 kA/m), the rejection curves of the BM' membrane did not change much further, indicating that the non-specific heat only could increase the local temperature in the membrane to a limited extent (cf. Section 4.3.3). However, the 5CL - 29 kA/m rejection curve was shifted further to higher molecular weight values compared to the 5CL - 20 kA/m rejection curve, suggesting that the sieving barrier pore size of membranes with immobilized IONPs could indeed be adjusted by changing the input magnetic field amplitude (cf. Section 4.3.3).

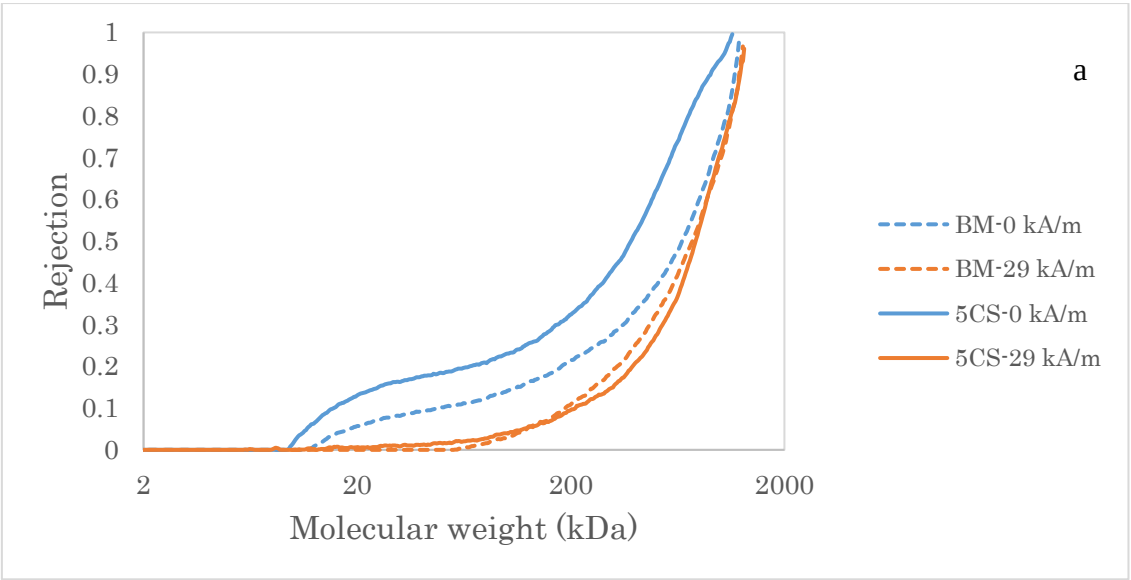

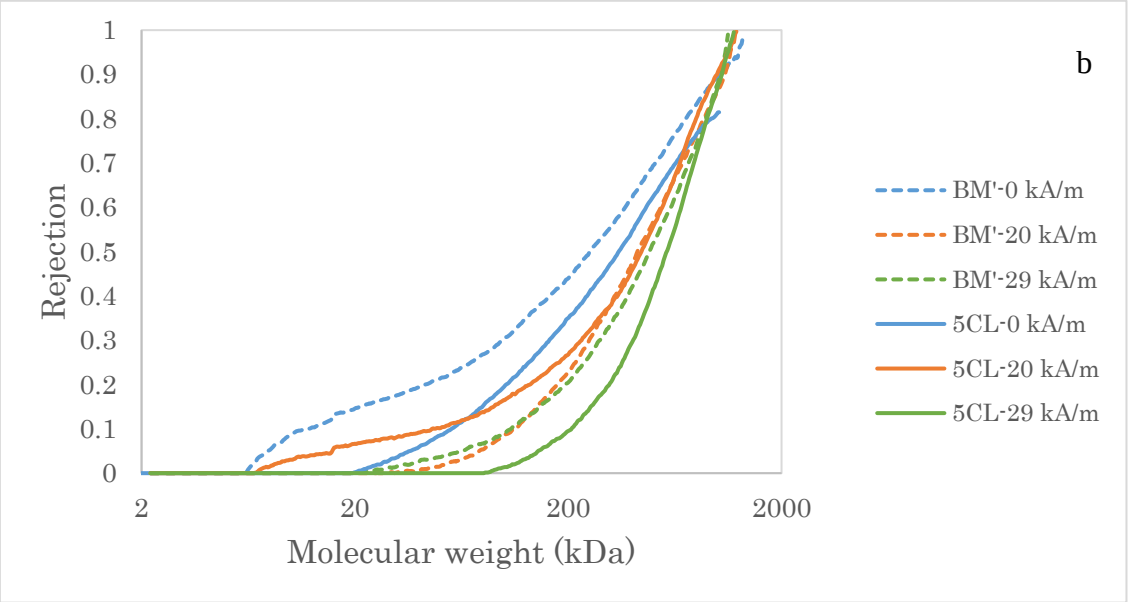

Figure 4.7. Rejection coefficients as a function of dextran molecular weight of (a) the BM and 5CS membranes with the magnetic field amplitude at 0 and 29 kA/m (initial fluxes ~193 Lm-2h-1; feed temperature fixed at ~15°C), and (b) the BM' and 5CL membranes with the magnetic field amplitude at 0, 20 and 29 kA/m (initial flux ~43 $Lm^{-2}h^{-1}$; feed temperature fixed at ~15°C). The aqueous feed solution contained 0.5 g/L of 35 kDa dextran and 0.5 g/L of 2000 kDa dextran.

The thermo-responsive molecular sieving performances of the 5CS and 5CL membranes were also studied by ultrafiltration of the same dextran mixtures at 10 °C, 30 °C and 50 °C (Figure 4.8a and 4.8b). The initial water flux of the 5CS membrane was set to about 193 $kg{\cdot}m^{-2}{\cdot}h^{-1}$ and the one for 5CL membrane to about 43 $kg{\cdot}m^{-2}{\cdot}h^{-1}$; i.e., identical conditions as for the experiments shown in Figure 4.7 had been chosen. As seen in Figure 4.8a, the rejection curves of for 5CS - 0 kA/m and 5CS - 10 °C, for 5CS - 20 kA/m and 5CS - 30 °C, and for 5CS - 29 kA/m and 5CS - 50 °C were overlapping, indicating that when the AMF was applied to the 5CS membrane at 0, 20 and 29 kA/m, the effective barrier pore sizes were approximately as large as the pores in the same membrane at 10 °C, 30 °C and 50 °C. Moreover, because the slope of the rejection curves was identical when using the external AMF, the open pores had still the same relatively small size distribution. This could be related to the rather finely distributed IONPs in the 5CS membranes. Note that the filtration system for the magneto-responsivity measurements might be not perfectly isolated, so that the real temperature of membrane for the magneto-responsive filtration measurements might be slightly higher or lower than 15 °C depending on the environment temperature. However, the 5CS - 0 kA/m, 5CS - 20 kA/m and 5CS - 29 kA/m curves were all obtained within short time interval, so that they are still comparable because of same environment conditions. It is reasonable that 5CS membrane has approximately the same effective barrier pore sizes at 0 kA/m (setting temperature: 15 °C) with AMF filtration setup and at 10 °C in thermo-responsive filtration measurement (cf. also rejection for dextran 500

kDa in Table 4.2), because of uncertainties due to the temperature effect from environment. Because the water flux for 5CS membrane is significantly higher than what would be based on the change of water viscosity at 15 °C compared to 10 °C (cf. Figure 4.4), a larger difference in rejection might have been expected as well. In Figure 4.8b, the differences between the thermo-responsive and the magneto-responsive rejection curves of the 5CL membrane are larger than for 5CS membrane. Because the IONPs in 5CL membranes were not homogeneously distributed while 5CS showed more homogeneously distributed IONPs as discussed in Sections 4.3.2, 4.3.3 and 4.3.4, the temperature and also pore size distribution in the 5CL membrane with the AMF are not ideally behaving. The especially large discrepancy between the magneto-responsive data for 5CL - 0 kA/m (15 °C) and the thermo-responsive data (obtained in another set-up) at 10 °C may also be caused by this larger heterogeneity. The observed differences in rejection (e.g.: 0.93 and 0.63 for dextran 500 kDa at 10 °C and 15 °C, respectively; cf. Table 4.2) could qualitatively be related to the different temperatures leading to different effective pore sizes (cf. above), but the uncertainties due to imperfect isolation evoked for the previous set of experiments are relevant in this case as well.

Overall, the AMF power-induced local heating can be approximated by setting the temperature via conventional heating of the feed when the IONPs are well dispersed and both AMF power and temperature lead to responses in terms of step-wise tunable changes of sieving barrier pore size distribution. The effect of magnetic field through IONPs is not only equivalent with that of direct heat as shown in Figure 4.8a but also shows potential for fast and external control of the size-selective membrane separation performance in nanometer scale.

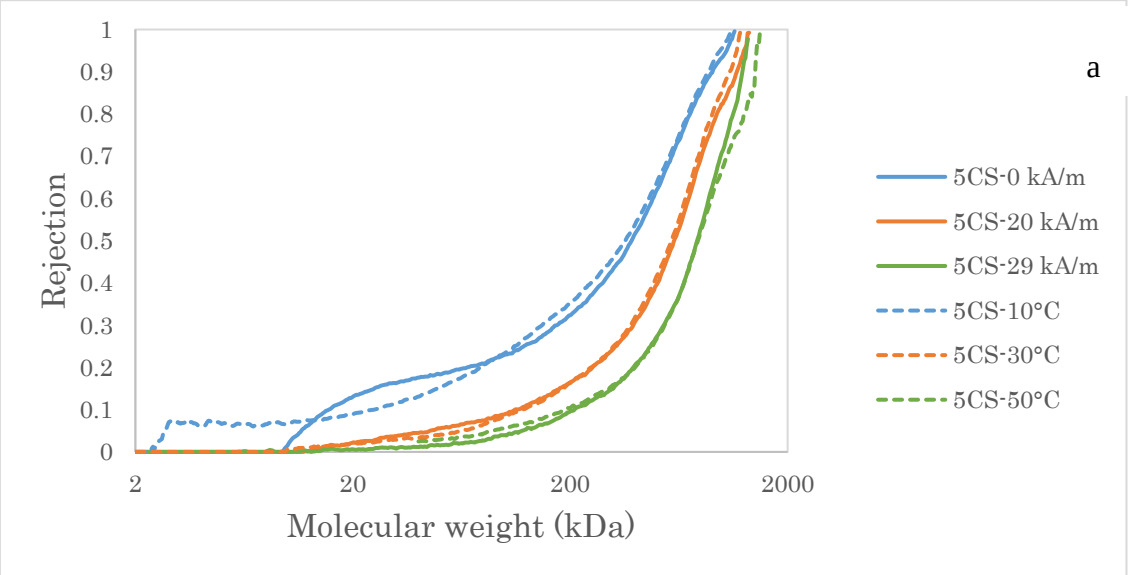

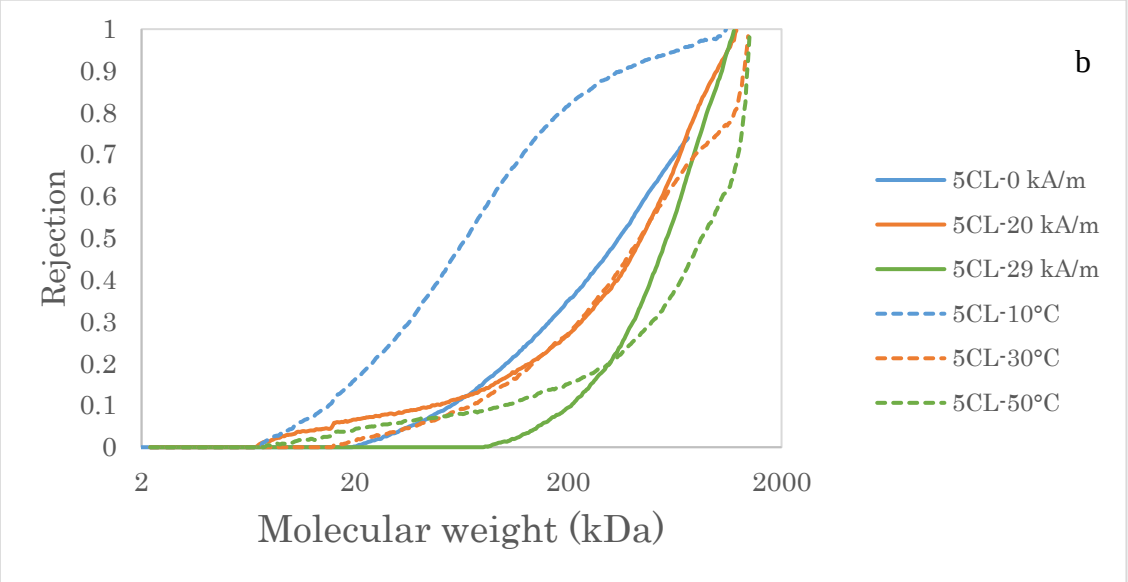

Figure 4.8. Rejection coefficients as a function of dextran molecular weight of (a) the 5CS membranes and (b) the 5CL membrane with AMF at different magnetic field amplitude (0, 20 and 29 kA/m, feed temperature fixed at ~15°C) and at different temperature (10 °C, 30 °C and 50 °C). The aqueous feed solution contained 0.5 g/L of 35 kDa dextran and 0.5 g/L of 2000 kDa dextran.

4.4. CONCLUSIONS

In this study, a novel magneto-responsive mesoporous membrane with remote-controllable, step-wise tunable changes of sieving barrier pore sizes was prepared in a very straightforward way. The membrane polymer $PMEO_{2.2}MA$-b-PS-b-$PMEO_{2.2}MA$ and the nano-heaters, 30 nm oleic acid covered iron oxide nanoparticles, were dissolved/dispersed in solution, and were spun-cast as thin barrier layer on a macroporous PVDF support membrane, followed by introducing the mesopores with the methanol-$scCO_2$ swelling method. With increasing standing times of the solution/dispersion before spin-casting, the size of the IONPs clusters became larger. The embedded IONPs did not change very much the membrane barrier pore size, as demonstrated by the SEM images and the separation curves measured by dextran ultrafiltration. In the presence of AMF, the heat generated by the IONPs increased the temperature within membrane and thus induced the conformational transition of the thermo-responsive $PMEO_{2.2}MA$ blocks on the membrane pore walls, leading to the change of effective membrane pore size, thus altering the water flux and dextran selectivity. The membranes with too low (1 mg/ml in spin-casting solution) or too high (10 mg/ml in spin-casting solution) loading of IONPs did not show a good magneto-responsivity. This is because insufficient specific heat could be provided for local temperature increase in the membranes with low amount of loaded IONPs, and too much loaded IONPs changed the morphology of the pores in the

membrane. The membranes with proper fraction of IONPs (5 mg/ml in spin-casting solution) all exhibited very pronounced magneto-responsive behaviors in water and dextran filtration experiments. However, the membranes with different size of dispersed IONPs clusters (5CS vs. 5CL, made using short or long standing time before film casting) showed different thermo-responsive and magneto-responsive behaviors. The water permeability *P* and its temperature response, $P_{45\,°C}$ / $P_{15\,°C}$, for the membrane with the larger IONPs clusters, 5CL, were the lowest among the three membrane types. Hence, aggregated IONPs strongly affect the membrane permeability and the thermo-responsive properties. However, since larger IONPs clusters could generate much greater local heat around the aggregates in the membrane, the 5CL membrane exhibited higher water flux increase when switching on AMF. Based on the water flux results with different magnetic field amplitudes, both IONPs-containing membranes showed step-wise larger effective pore sizes with step-wise increasing magnetic field strength. The detailed investigation of molecular sieving properties of 5CS and 5CL membranes suggested that the effects of AMF power on local heating can be approximated by temperature adjustment via conventional heating of the feed when the IONPs are well dispersed. The effect of magnetic field through IONPs is not only equivalent with that of direct heating but also shows great potential for fast and external control of the size-selective membrane separation performance in nanometer scale. In conclusion, the established novel remote controllable ultrafiltration membrane with dynamic, finely tunable barrier pore size will expand the possibilities for design and fabrication of "smart" systems for separation, analytical, therapeutic or other applications.

4.5 SUPPORTING INFORMATION

4.5.1. Alternating magnetic field (AMF) amplitude

The relation between the input current and field amplitude was investigated by fixing the measuring site in the centre of the sandwich coils. The pickup probe was fixed in the centre of the sandwich coils with varying input current (*I*), at certain field frequency (395 kHz, 614 kHz, 656 kHz and 745 kHz). The induced peak voltage within the probe was detected by oscilloscope. Magnetic field amplitude (*H*) at the site was calculated according to following equations, derived from Faraday's law of electromagnetic induction:

$$U_{max} = \frac{U_{pp}}{2}$$

$$H = U_{max} \cdot \frac{1}{N} \cdot \frac{1}{f} \left(\frac{2}{\pi^2 \cdot \mu_0 \cdot D^2} \right)$$

Where U_{max} is the peak value of induced voltage, U_{pp} is peak-to-peak voltage given by oscilloscope, *N* is the number of loops of the probe, *D* is the diameter of the loop, μ_o is permeability constant of copper, *f* is the frequency of AMF.

Figure S4.1a shows that magnetic field amplitude was in good linear relationship with input current (higher input current resulted in higher field amplitude), while the field frequency had no influence. The relationship between input current and resulting field amplitude was H = 1.861 * I according to the trend line in Figure S4.1b.

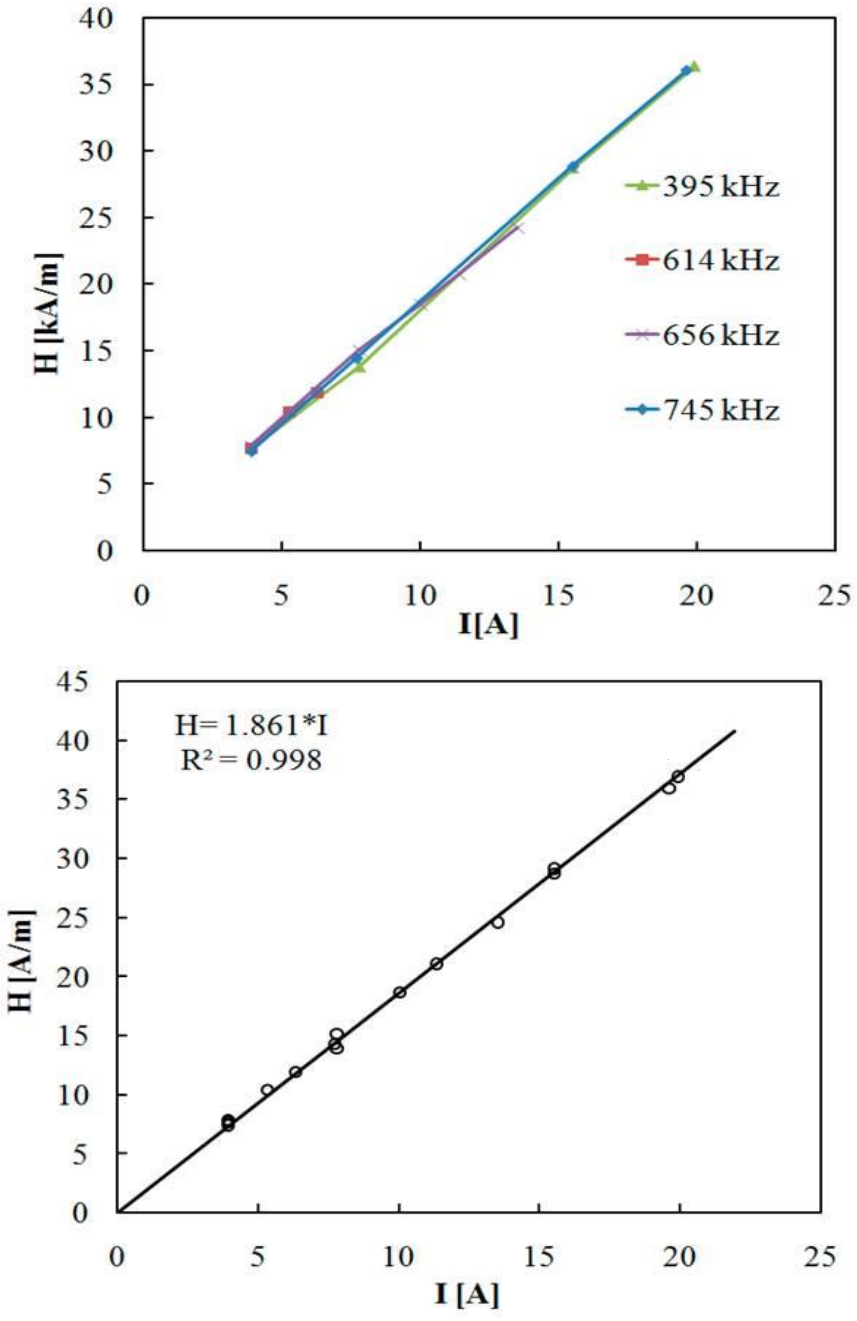

Figure S4.1. (a) Magnetic field amplitude (H) in the centre of sandwich coils with different current (I) and frequency (f); (b) linear relation between field amplitude (H) and input current (I).

4.5.2. Water flux with and without AMF at different initial fluxes

Table S4.1. The water flux measurements for the BM, 1CS and 5CS membranes without and with the AMF performed at low (L), middle (M) and high (H) initial flux (the unit of all the water fluxes is kg▪m^{-2}▪h^{-1}).

Flux level	Low			Middle			High		
Membranes	BM-L	1CS-L	5CS-L	BM-M	1CS-M	5CS-M	BM-H	1CS-H	5CS-H
J_{off}	15.6	15.6	16.6	43.7	44.1	40.8	187.7	190.6	195.3
J_{on}	45.4	35.7	50.1	100.3	97.9	110.6	308.7	301.2	377.0
$\Delta J=J_{on}- J_{off}$	29.8	20.6	33.4	56.6	53.8	69.8	121.0	110.6	181.7
$\Delta J/ J_{off}$	1.9	1.3	2.0	1.3	1.2	1.7	0.6	0.6	0.9
$\Delta J_{XCS}-\Delta J_{BM}$ *	-	-9.8	3.6	-	-2.7	13.2	-	-10.4	60.7

*ΔJ_{XCS} represents ΔJ_{1CS} or ΔJ_{5CS}

Table S4.2. The water flux measurements for the BM, 5CL and 10CL membranes without and with the AMF performed at low (L) and middle (M) initial flux (the unit of all the water fluxes is kg▪m^{-2}▪h^{-1}).

Flux level	Low			Middle		
Membranes	BM-L	5CL-L	10CL-L	BM-M	5CL-M	10CL-M
J_{off}	13.5	16.1	13.5	39.9	40.1	44.6
J_{on}	52.6	89.3	58.1	86.2	199.0	144.5
$\Delta J=J_{on}- J_{off}$	39.1	73.2	44.6	46.3	158.9	99.9

$\Delta J/ J_{off}$	2.9	4.6	3.3	1.2	4.0	2.2
ΔJ_{XCL}-ΔJ_{BM}*	-	34.1	5.5	-	112.6	53.7

*ΔJ_{XCL} represents ΔJ_{5CL} or ΔJ_{10CL}

4.5.3. Magneto-responsive performances of 5CS and 5CL membranes with different magnetic field amplitude (H)

During the filtration, the AMF was kept at OFF state for 15 minutes, then it was switched ON for 30 minutes, and thereafter is war turned OFF. The water fluxes were monitored by weighting filtrates every 5 minutes. The water flux measurement was started at ~190 L▪m^{-2}▪h^{-1} for the BM and 5CS membranes. The initial water flux of the BM and 5CL membrane was ~40 L▪m^{-2}▪h^{-1}. Four different magnetic field amplitudes was chose, they were 15 kA/m, 20 kA/m, 25 kA/m and 29 kA/m. The water flux changes of the BM vs. 5CS membranes and the BM vs. 5CL membranes are shown in Figure S4.2a and S4.2b, respectively.

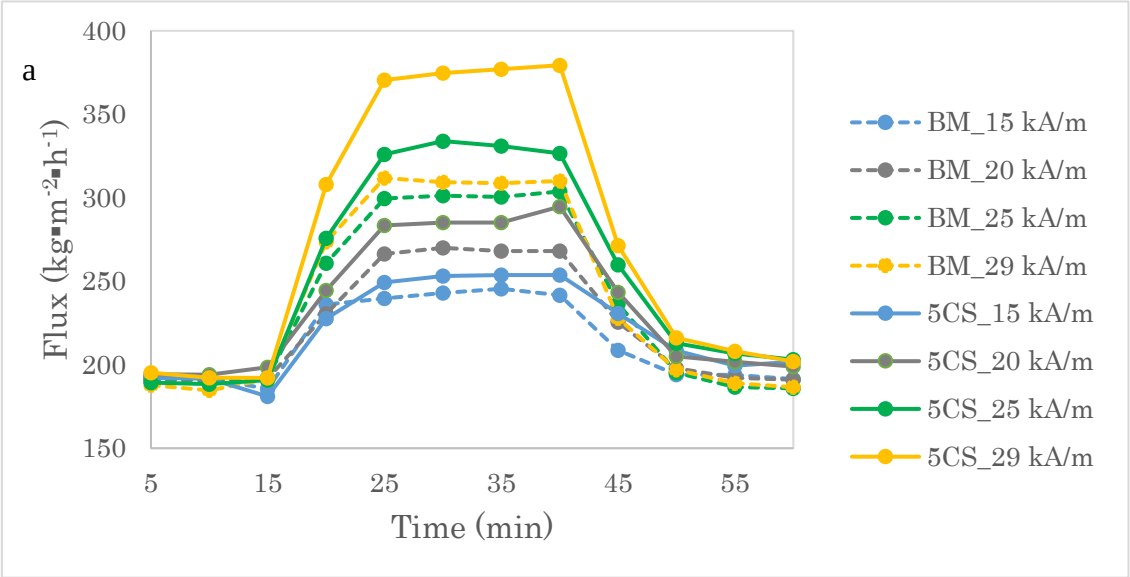

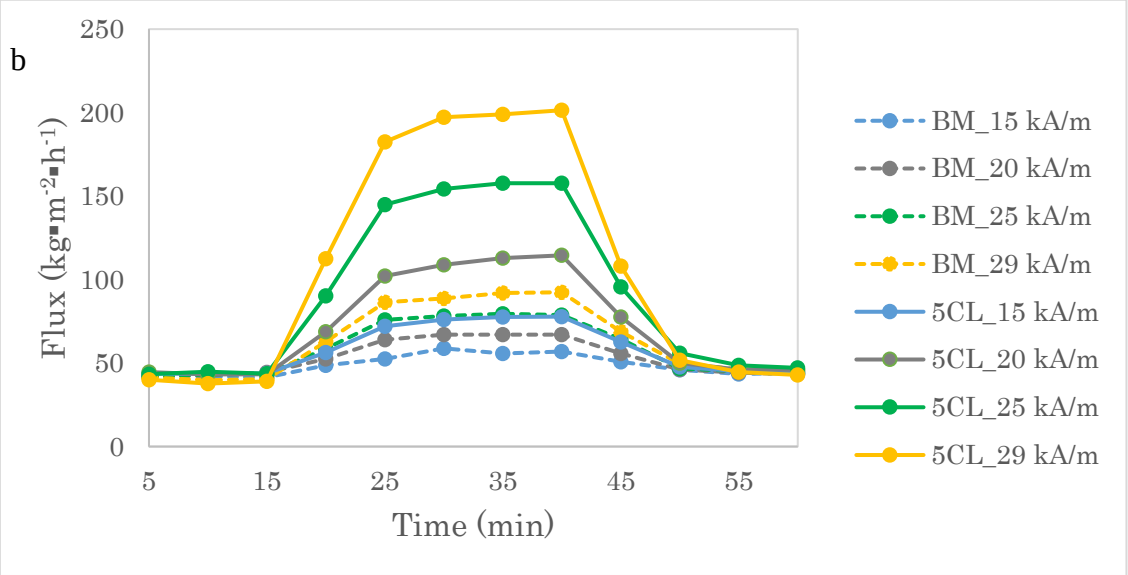

Figure S4.2. Water flux changes in the presence and absence of the AFM for (a) the BM and 5CS membranes with the initial flux at ~190 L▪m^{-2}▪h^{-1} (high) and (b) the BM and 5CL membrane with the initial flux at ~40 L▪m^{-2}▪h^{-1} (middle).

4.5.4. Fluxes measured during dextran sieving experiments

The pure water flux was measured before and after the dextran filtrations (Figure S4.3a,b). The temperature was fixed at ~15 °C all the time. Certain transmembrane pressure for each membrane was decided to ensure the initial flux of the 5CS and 5CL membranes and their reference membranes (the BM and BM' membranes) at same level, and the decided transmembrane pressures were kept during whole experiments. Without AMF, the filtration flux decreased dramatically when the feed changed from water to dextran solution, due to the concentration polarization. The dextran filtration flux of all the membranes increased as the AMF was turned on, but the flux values of membranes with IONPs always kept higher than their reference membranes.

In Figure S4.3b, the 5CL membrane exhibited larger dextran filtration flux with higher magnetic field amplitude. After the dextran filtration experiments, the water flux of all the membranes were measured again. The decreased water flux indicates irremovable fouling of the membranes. Comparing to the BM and 5CS membranes, the BM' and 5CL membranes only had a low extent of fouling effect. The reason might be the lower transmembrane pressures applied on the BM' and 5CL membranes.

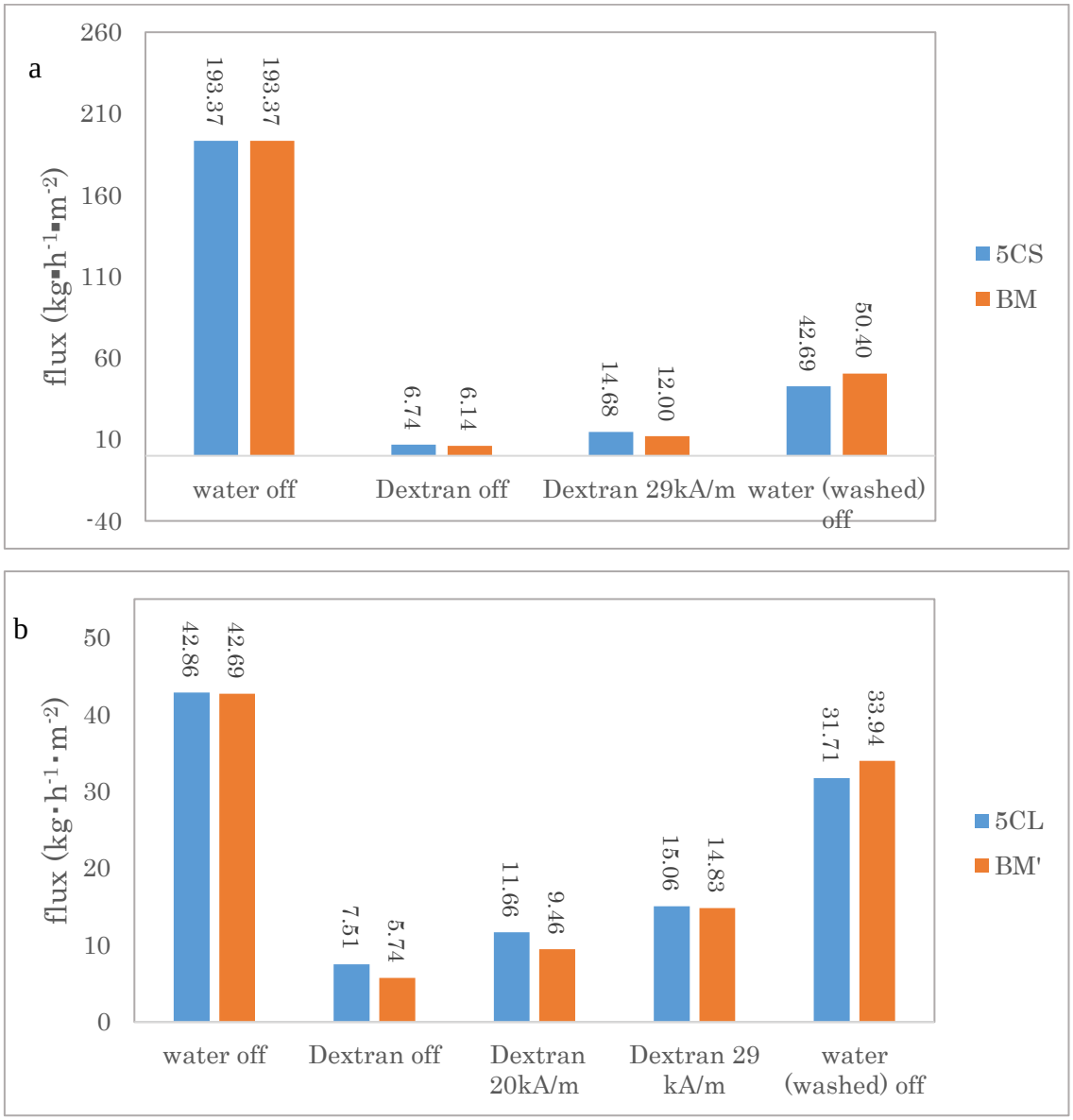

Figure S4.3. Water and dextran filtration flux monitored during the filtration tests. (a) is for the BM and 5CS membranes, and (b) is for the BM' and 5CL membranes.

5. Mesoporous block copolymer membranes with thermo- and pH-responsivities

（この部分は、Journal of Membrane Science に掲載等の形で刊行される予定であるため、学位授与日から 5 年間インターネットでの公表をすることができません。）

6. Summary

In this study, by using amphiphilic block copolymers (BCPs) as templates, three kinds of stimuli-responsive mesoporous membranes with narrow size dispersity have been developed.

The first type is **thermo-responsive mesoporous block copolymer membrane** prepared by introducing nanopores into poly(oligoethylene glycol methyl ether methacrylate)-*b*-polystyrene-*b*-poly(oligoethylene glycol methyl ether methacrylate) ($PMEO_nMA$-*b*-PS-*b*-$PMEO_nMA$) templates via selective swelling the $PMEO_nMA$ domains. The membrane with PS being the mechanical stable part of the matrix and thermo-responsive $PMEO_nMA$ covered the mesopores interiors. The changeable LCST property of $PMEO_nMA$ provided the membranes a tunable responsive temperature, ranging from 25 to 55 °C. These membranes are with narrow pore size distribution, promising for separating nanoparticles with only three times difference. The temperature dependent changes of water permeability and particles permeation all demonstrate the thermos-responsivity of the membranes; however, the open-close transition of the pores was not sudden at the LCSTs but instead occurred gradually over a broad temperature range.

The second type is **magneto-responsive mesoporous block copolymer membrane** constructed by embedding iron oxide nanoparticles (IONPs) as local heaters into the PS matrix of the foresaid porous block copolymer membrane. IONPs and $PMEO_{2.2}MA$-b-PS-b-$PMEO_{2.2}MA$ mixture solutions were spun-cast on PVDF membranes, and then mesopores were introduced into the hydrophilic $PMEO_{2.2}MA$ domains by controlled selective swelling with a mixture of methanol and $scCO_2$. The loaded IONPs aggregated into small clusters (0.1-1 μm) and were finely dispersed in the $PMEO_{2.2}MA$-b-PS-b-$PMEO_{2.2}MA$ mesoporous top layer. No defect was found in the membranes with IONPs based on water and dextran ultrafiltration performances, and scanning electron microscopy (SEM) images showed that their barrier pore sizes were almost identical to those of no IONPs containing membranes. Upon stimulation with alternating magnetic field with different input energy, the water permeability as well as the dextran rejection were tuned into different levels, indicating that the sieving barrier pore size distribution of these thin-film mixed matrix nanocomposite membranes was step-wise adjustable.

The third type is **thermo- and pH-responsive mesoporous block copolymer membrane** fabricated with PDMAEMA-b-$PMEO_2MA$-b-PS and $PMEO_2MA$-b- PDMAEMA-b-PS by selective swelling hydrophilic domains. With permeability measurements with different feed and temperature, we found both tri-block copolymer prepared membranes were with two-step thermo-responsivity. An expanded or collapsed state for each of the individual hydrophilic blocks at different temperature had been known by observing PDMAEMA-b-$PMEO_2MA$ diblock copolymer brushes with neutron reflectometry. However, among those two membranes, only the PDMAEMA-b-$PMEO_2MA$-b-PS membrane had reversibly

changing ultrafiltration properties with independent response to temperature and pH. The reason for it still have not yet been defined, but will be answer with further investigation.

7. Outlook

Stimuli-responsive membranes have many established and potential applications in separation processes, artificial sensors and drug delivery systems, etc., but they are still a new and fast developing field and have many improvement need to be done.

1. The three membranes developed in this thesis are all fabricated by introducing pore into block copolymer templates via methanol-scCO_2 selective swelling method, therefore, the membrane pores exist in bicontinuous structure. The high tortuosity of membrane pores doubtlessly increase the resistance to feed solution during filtration, leading to a lower permeability and further raise the energy consumption. To compensate this drawback, in the study, we decreased the effective barrier layers (BCP layers) thickness into very thin, about 1-2 um, by constructing BCP and macroporous PVDF composite membrane structure. Therefore, the absolute permeabilities of these membranes are in the same level compared to the established ultrafiltration membranes. To increase the membrane porosity is a target of further development.

2. The pore size and porosity of membranes are highly depend on the block copolymer structure and pore making condition. To optimize the membrane properties, like further decrease the pore size dispersity, the detail information on pore making mechanism with methanol-scCO_2 selective swelling method should be thoroughly investigated.

3. For the magneto-responsive membrane, the heat generated by the embedded IONPs can only increase the temperature of membrane instead of the feed solution. Therefore, the temperature difference near the membrane surface may can lead to a thermal convection, and then result in a lower concentration polarization. This IONPs induced concentration polarization reducing may also can be applied in traditional membranes for increasing permeability and decreasing fouling.

4. The multi-responsive membrane (having independent responsivity to each stimuli) is a quite new topic and a lot of challenges need to face. First, the fundamental information for the responsive properties of multi-responsive block copolymers is still missing. Therefore, the investigations on the physicochemical characterization of multi-responsive polymers brushes or hydrogels are need to be done. Second, the multi-responsivity of established multi-responsive membranes are almost realized by using block copolymers consisting two or more types of stimuli-responsive polymer blocks. The drawbacks of this kind of system are (1) exist of interactions of those polymer blocks and (2) uneven responsivity of the block copolymer to different stimuli. Therefore, the preparation strategy should be explored. For example, I am planning to fabricate a thermo- and pH-responsive membrane, with tunable molecular sieving ultrafiltration performance, by blending rotaxane cross-linked (RC) nanogels with common membrane polymer polyethersulfone (PES) and processing the dope solution by NIPS. RC nanogels were recently successfully synthesized using precipitation polymerization and they exhibited a decoupled thermo- and pH-responsive

volume transition (Figure 6.1). The membranes are expected to have anisotropic cross-section morphology with a micrometer-thin dense top layer and a thick macroporous support layer. The RC nanogels will be embedded in the top layer and work as functional gates, as shown in Figure 6.2.

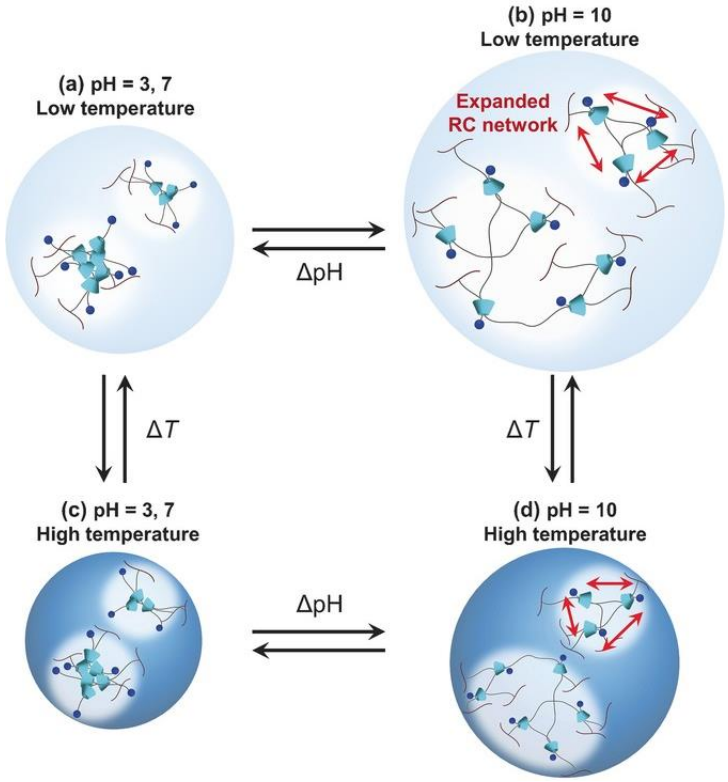

Figure 6.1. Schematic illustration of thermo- and pH-responsivity of the RC nanogels.[220]

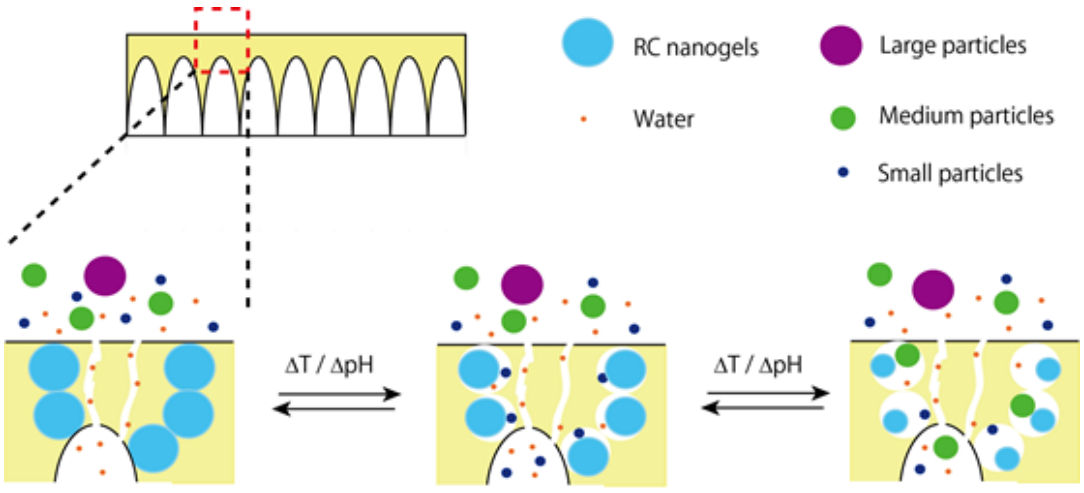

Figure 6.2. Schematic illustration of reversible change of molecular sieving by temperature and pH.

8. Acknowledgements

I wish to express my appreciation to my supervisor, Associate Professor Hideaki Yokoyama. He provided me priceless advices and guides on my research. Thanks to his help as well as moral support during the past 6 years. He have given me a chance to study in the University of Tokyo, a chance to change my life direction.

I would specially like to thank Professor Mathias Ulbricht, my advisor during my exchange study in the University of Duisburg-Essen, Germany. Without his help and guides, I would not finish the preparation of the magneto-responsive membranes (in Chapter 4). Thanks for him to help me open a door to membrane science. Many thanks for his student Dr. Xi Lin who provide me many help and suggestions on membrane preparation.

I would specially like to thank Professor Kohzo Ito. His brilliant comments and suggestions helped me overcome many problems. He is a pioneer who developed slide-ring gel. His passion on research encourages me to become a good researcher in the future.

I would specially like to thank Professor Takashi Ishizone (Tokyo Institute of Technology) and his student Ling Hong. They kindly provided me valuable support on block copolymer synthesis.

I would specially like to thank Assistant Professor Rina Maeda for her valuable guides on block copolymer synthesis and GPC maintenance.

I would specially like to thank Project lecture Koichi Mayumi for teaching me use many instruments. Also he provided us comfortable office room environment.

I praise the enormous amount of help and teaching from the members of Ito-Yokoyama group and Mathias Ulbricht group. They are amazing people in too many ways. Thank you to them for supporting me academically and emotionally through the rough road to finish this thesis. The kindness from them helped me enjoy the life during my Ph.D. courses.

At last, many thanks to my dear parents and all the lovely people I met. They help me become a person who now I am.

9. Published list

Academic Papers

1. **Tang, Y. C.**; Lin, X.; Ito, K.; Hong, L.; Ishizone, T.; Yokoyama, H.; Ulbricht, M., Tunable magneto-responsive mesoporous block copolymer membranes. *Journal of Membrane Science* **2017**, *544 (Supplement C)*, 406-415.
2. **Tang, Y. C.**; Ito, K.; Hong, L.; Ishizone, T.; Yokoyama, H., Tunable Thermoresponsive Mesoporous Block Copolymer Membranes. *Macromolecules* **2016,** *49* (20), 7886-7896.
3. **Tang, Y. C.**; Lu, K.; Cao, X. J.; Li, Y. J., Nanostructured Thermoplastic Vulcanizates by Selectively Cross-Linking a Thermoplastic Blend with Similar Chemical Structures. *Ind Eng Chem Res* **2013,** *52* (35), 12613-12621.

Patent

1. Li, Y. J.; **Tang, Y. C**, A Novel Oil-resistant Thermoplastic Vulcanizate and its fabrication method, Chinese patent, *CN 103059401 B*, **2012**. Assignee: Hangzhou Normal University
2. Ouyang, Y. j.; Tang, L. L.; **Tang, Y. C**, A method of increasing the copper corrosion inhibition in alkaline medium, Chinese patent, *CN 104073807 B*, **2017**. Assignee: College of Huaihua

Book

1. Li, Y. J., **Tang, Y. C**, Chapter title: Thermoplastic Vulcanizates (TPVs) by the Dynamic Vulcanization from Miscible or Highly Compatible Plastic/Rubber Blends, *Reactive Extrusion: Principles and Applications, First Edition* (2017)

10. References

1. Wandera, D.; Wickramasinghe, S. R.; Husson, S. M. Stimuli-responsive membranes. *Journal of Membrane Science* **2010,** 357 (1), 6-35 DOI: https://doi.org/10.1016/j.memsci.2010.03.046.

2. Zhao, B.; Brittain, W. J. Polymer brushes: surface-immobilized macromolecules. *Progress in Polymer Science* **2000,** 25 (5), 677-710 DOI: https://doi.org/10.1016/S0079-6700(00)00012-5.

3. Tang, Y. C.; Ito, K.; Hong, L.; Ishizone, T.; Yokoyama, H. Tunable Thermoresponsive Mesoporous Block Copolymer Membranes. *Macromolecules* **2016,** 49 (20), 7886-7896 DOI: 10.1021/acs.macromol.6b01665.

4. Tang, Y.; Lin, X.; Ito, K.; Hong, L.; Ishizone, T.; Yokoyama, H.; Ulbricht, M. Tunable magneto-responsive mesoporous block copolymer membranes. *Journal of Membrane Science* **2017,** 544 (Supplement C), 406-415 DOI: https://doi.org/10.1016/j.memsci.2017.08.069.

5. Stuart, M. A. C.; Huck, W. T. S.; Genzer, J.; Muller, M.; Ober, C.; Stamm, M.; Sukhorukov, G. B.; Szleifer, I.; Tsukruk, V. V.; Urban, M.; Winnik, F.; Zauscher, S.; Luzinov, I.; Minko, S. Emerging applications of stimuli-responsive polymer materials. *Nat Mater* **2010,** 9 (2), 101-113 DOI: 10.1038/Nmat2614.

6. Soppimath, K. S.; Aminabhavi, T. M.; Dave, A. M.; Kumbar, S. G.; Rudzinski, W. E. Stimulus-responsive "smart" hydrogels as novel drug delivery systems. *Drug Development and Industrial Pharmacy* **2002,** 28 (8), 957-974 DOI: 10.1081/ddc-120006428.

7. Hoffman, A. S. Stimuli-responsive polymers: Biomedical applications and challenges for clinical translation. *Adv Drug Deliver Rev* **2013,** 65 (1), 10-16 DOI: https://doi.org/10.1016/j.addr.2012.11.004.

8. Qiu, Y.; Park, K. Environment-sensitive hydrogels for drug delivery. *Adv Drug Deliver Rev* **2012,** 64, 49-60 DOI: 10.1016/j.addr.2012.09.024.

9. Davis, D. A.; Hamilton, A.; Yang, J. L.; Cremar, L. D.; Van Gough, D.; Potisek, S. L.; Ong, M. T.; Braun, P. V.; Martinez, T. J.; White, S. R.; Moore, J. S.; Sottos, N. R. Force-induced activation of covalent bonds in mechanoresponsive polymeric materials. *Nature* **2009,** 459 (7243), 68-72 DOI: 10.1038/nature07970.

10. Wei, M. L.; Gao, Y. F.; Li, X.; Serpe, M. J. Stimuli-responsive polymers and their applications. *Polymer Chemistry* **2017,** 8 (1), 127-143 DOI: 10.1039/c6py01585a.

11. Thevenot, J.; Oliveira, H.; Sandre, O.; Lecommandoux, S. Magnetic responsive polymer composite materials. *Chem Soc Rev* **2013,** 42 (17), 7099-7116 DOI: 10.1039/c3cs60058k.

12. Schmaljohann, D. Thermo- and pH-responsive polymers in drug delivery. *Adv Drug Deliver Rev* **2006,** 58 (15), 1655-1670 DOI: 10.1016/j.addr.2006.09.020.

13. Michael Rubinstein; Colby, R. H., Thermodynamics of mixing. In *Polymer physics*, Oxford University Press: New York, 2003.

14. Hany B. Eitouni, N. P. B., Thermodynamics of Polymer Blends. In *Physical Properties of Polymers Handbook*, Mark, J. E., Ed. Springer: New York, 2007.

15. Niskanen, J.; Tenhu, H. How to manipulate the upper critical solution temperature (UCST)? *Polymer Chemistry* **2017,** 8 (1), 220-232 DOI: 10.1039/c6py01612j.

16. Seuring, J.; Agarwal, S. Polymers with Upper Critical Solution Temperature in Aqueous Solution. *Macromol Rapid Comm* **2012,** 33 (22), 1898-1920 DOI: 10.1002/marc.201200433.

17. Kim, Y. J.; Matsunaga, Y. T. Thermo-responsive polymers and their application as smart biomaterials. *Journal of Materials Chemistry B* **2017,** 5 (23), 4307-4321 DOI: 10.1039/c7tb00157f.

18. Zhang, Q.; Hoogenboom, R. Polymers with upper critical solution temperature behavior in alcohol/water solvent mixtures. *Progress in Polymer Science* **2015,** 48, 122-142 DOI: https://doi.org/10.1016/j.progpolymsci.2015.02.003.

19. Ougizawa, T.; Inoue, T. UCST AND LCST BEHAVIOR IN POLYMER BLENDS AND ITS THERMODYNAMIC INTERPRETATION. *Polym J* **1986,** 18 (7), 521-527 DOI: 10.1295/polymj.18.521.

20. Schild, H. G. Poly (N-Isopropylacrylamide) - Experiment, Theory and Application. *Progress in Polymer Science* **1992,** 17 (2), 163-249 DOI: Doi 10.1016/0079-6700(92)90023-R.

21. Kubota, K.; Fujishige, S.; Ando, I. SOLUTION PROPERTIES OF POLY(N-ISOPROPYLACRYLAMIDE) IN WATER. *Polym J* **1990,** 22 (1), 15-20 DOI: 10.1295/polymj.22.15.

22. Misra, G. P.; Siegel, R. A. New mode of drug delivery: long term autonomous rhythmic hormone release across a hydrogel membrane. *Journal of Controlled Release* **2002,** 81 (1), 1-6 DOI: https://doi.org/10.1016/S0168-3659(02)00043-3.

23. Li, J. J.; Zhou, Y. N.; Luo, Z. H. Thermo-responsive brush copolymers with structure-tunable LCST and switchable surface wettability. *Polymer* **2014,** 55 (25), 6552-6560 DOI: 10.1016/j.polymer.2014.10.025.

24. Principi, T.; Goh, C. C. E.; Liu, R. C. W.; Winnik, F. M. Solution properties of hydrophobically modified copolymers of N-isopropylacrylamide and N-glycine acrylamide: A study by microcalorimetry and fluorescence spectroscopy. *Macromolecules* **2000,** 33 (8), 2958-2966 DOI: 10.1021/ma9919054.

25. Plummer, R.; Hill, D. J. T.; Whittaker, A. K. Solution properties of star and linear poly(N-isopropylacrylamide). *Macromolecules* **2006,** 39 (24), 8379-8388 DOI: 10.1021/ma0614545.

26. Aoyagi, T.; Ebara, M.; Sakai, K.; Sakurai, Y.; Okano, T. Novel bifunctional polymer with reactivity and temperature sensitivity. *Journal of Biomaterials Science-Polymer Edition* **2000,** 11 (1), 101-110 DOI: 10.1163/156856200743526.

27. Yoshida, T.; Aoyagi, T.; Kokufuta, E.; Okano, T. Newly designed hydrogel with both sensitive thermoresponse and biodegradability. *J Polym Sci Pol Chem* **2003,** 41 (6), 779-787 DOI: 10.1002/pola.10595.

28. Maeda, T.; Yamamoto, K.; Aoyagi, T. Importance of bound water in hydration–dehydration behavior of hydroxylated poly(N-isopropylacrylamide). *Journal of Colloid and Interface Science* **2006,** 302 (2), 467-474 DOI: https://doi.org/10.1016/j.jcis.2006.06.047.

29. CHU, L.-Y., *Smart Membrane Materials and Systems-From Flat Membranes to Microcapsule Membranes*. Springer-Verlag Berlin Heidelberg: Hangzhou, 2011.

30. Sedlacek, O.; Monnery, B. D.; Filippov, S. K.; Hoogenboom, R.; Hruby, M. Poly(2-Oxazoline)s - Are They More Advantageous for Biomedical Applications Than Other Polymers? *Macromol Rapid Comm* **2012,** 33 (19), 1648-1662 DOI: 10.1002/marc.201200453.

31. Hoogenboom, R.; Schlaad, H. Thermoresponsive poly(2-oxazoline)s, polypeptoids, and polypeptides. *Polymer Chemistry* **2017,** 8 (1), 24-40 DOI: 10.1039/c6py01320a.

32. Luxenhofer, R.; Schulz, A.; Bronich, T. K.; Kabanov, A. V.; Jordan, R. Poly(2-oxazoline)s as polymer therapeutics. *Abstr Pap Am Chem S* **2012,** 243.

33. Kricheldorf, H. R. Polypeptides and 100 years of chemistry of alpha-amino acid N-carboxyanhydrides. *Angew Chem Int Edit* **2006,** 45 (35), 5752-5784 DOI: 10.1002/anie.200600693.

34. Uyama, H.; Kobayashi, S. A NOVEL THERMOSENSITIVE POLYMER - POLY(2-ISO-PROPYL-2-OXAZOLINE). *Chemistry Letters* **1992,** (9), 1643-1646 DOI: 10.1246/cl.1992.1643.

35. Park, J. S.; Kataoka, K. Comprehensive and accurate control of thermosensitivity of poly(2-alkyl-2-oxazoline)s via well-defined gradient or random copolymerization. *Macromolecules* **2007,** 40 (10), 3599-3609 DOI: 10.1021/ma0701181.

36. Lin, P. Y.; Clash, C.; Pearce, E. M.; Kwei, T. K.; Aponte, M. A. SOLUBILITY AND MISCIBILITY OF POLY(ETHYL OXAZOLINE). *Journal of Polymer Science Part B-Polymer Physics* **1988,** 26 (3), 603-619 DOI: 10.1002/polb.1988.090260312.

37. Hoogenboom, R. Poly(2-oxazoline)s: A Polymer Class with Numerous Potential Applications. *Angew Chem Int Edit* **2009,** 48 (43), 7978-7994 DOI: 10.1002/anie.200901607.

38. Yamamoto, S. I.; Pietrasik, J.; Matyjaszewski, K. The effect of structure on the thermoresponsive nature of well-defined poly(oligo(ethylene oxide) methacrylates) synthesized by ATRP. *J Polym Sci Pol Chem* **2008,** 46 (1), 194-202 DOI: 10.1002/pola.22371.

39. Lessard, B. H.; Ling, E. J. Y.; Maric, M. Fluorescent, Thermoresponsive Oligo(ethylene glycol) Methacrylate/9-(4-Vinylbenzyl)-9H-carbazole Copolymers Designed with Multiple LCSTs via Nitroxide Mediated Controlled Radical Polymerization. *Macromolecules* **2012,** 45 (4), 1879-1891 DOI: 10.1021/ma202648k.

40. Becer, C. R.; Kokado, K.; Weber, C.; Can, A.; Chujo, Y.; Schubert, U. S. Metal-Free Synthesis of Responsive Polymers: Cloud Point Tuning by Controlled "Click" Reaction. *J Polym Sci Pol Chem* **2010,** 48 (6), 1278-1286 DOI: 10.1002/pola.23872.

41. Hu, Z. B.; Cai, T.; Chi, C. L. Thermoresponsive oligo(ethylene glycol)-methacrylate- based polymers and microgels. *Soft Matter* **2010,** 6 (10), 2115-2123 DOI: 10.1039/b921150k.

42. Lutz, J. F. Thermo-Switchable Materials Prepared Using the OEGMA-Platform. *Adv Mater* **2011,** 23 (19), 2237-2243 DOI: 10.1002/adma.201100597.

43. Lutz, J. F. Polymerization of oligo(ethylene glycol) (meth)acrylates: Toward new generations of smart biocompatible materials. *J Polym Sci Pol Chem* **2008,** 46 (11), 3459-3470 DOI: 10.1002/pola.22706.

44. Ishizone, T.; Han, S.; Okuyama, S.; Nakahama, S. Synthesis of water-soluble polymethacrylates by living anionic polymerization of trialkylsilyl-protected oligo(ethylene glycol) methacrylates. *Macromolecules* **2003,** 36 (1), 42-49 DOI: 10.1021/ma021257f.

45. Ishizone, T.; Han, S.; Hagiwara, M.; Yokoyama, H. Synthesis and surface characterization of well-defined amphiphilic block copolymers containing poly oligo(ethylene glycol) methacrylatel segments. *Macromolecules* **2006,** 39 (3), 962-970 DOI: 10.1021/ma0521699.

46. Lutz, J. F.; Akdemir, O.; Hoth, A. Point by point comparison of two thermosensitive polymers exhibiting a similar LCST: Is the age of poly(NIPAM) over? *J Am Chem Soc* **2006,** 128 (40), 13046-13047 DOI: 10.1021/ja065324n.

47. Lutz, J. F.; Hoth, A. Preparation of ideal PEG analogues with a tunable thermosensitivity by controlled radical copolymerization of 2-(2-methoxyethoxy)ethyl methacrylate and oligo(ethylene glycol) methacrylate. *Macromolecules* **2006,** 39 (2), 893-896 DOI: 10.1021/ma0517042.

48. Yamamoto, S.; Pietrasik, J.; Matyjaszewski, K. ATRP synthesis of thermally responsive molecular brushes from oligo(ethylene oxide) methacrylates. *Macromolecules* **2007,** 40 (26), 9348-9353 DOI: 10.1021/ma701970t.

49. Han, S.; Hagiwara, M.; Ishizone, T. Synthesis of thermally sensitive water-soluble polymethacrylates by living anionic polymerizations of oligo(ethylene glycol) methyl ether methacrylates. *Macromolecules* **2003,** 36 (22), 8312-8319 DOI: 10.1021/ma0347971.

50. Ishizone, T.; Seki, A.; Hagiwara, M.; Han, S.; Yokoyama, H.; Oyane, A.; Deffieux, A.; Carlotti, S. Anionic polymerizations of oligo(ethylene glycol) alkyl ether methacrylates: Effect of side chain length and omega-alkyl group of side chain on cloud point in water. *Macromolecules* **2008,** 41 (8), 2963-2967 DOI: 10.1021/ma702828n.

51. Lutz, J. F.; Borner, H. G.; Weichenhan, K. Combining ATRP and "click" chemistry: a promising platform toward functional biocompatible polymers and polymer bioconjugates. *Macromolecules* **2006,** 39 (19), 6376-6383 DOI: 10.1021/ma061557n.

52. Lutz, J. F.; Weichenhan, K.; Akdemir, O.; Hoth, A. About the phase transitions in aqueous solutions of thermoresponsive copolymers and hydrogels based on 2-(2-methoxyethoxy)ethyl methacrylate and oligo(ethylene glycol) methacrylate. *Macromolecules* **2007,** 40 (7), 2503-2508 DOI: 10.1021/ma062925q.

53. Lutz, J. F.; Ouchi, M.; Liu, D. R.; Sawamoto, M. Sequence-Controlled Polymers. *Science* **2013,** 341 (6146), 628-+ DOI: 10.1126/science.1238149.

54. Vancoillie, G.; Frank, D.; Hoogenboom, R. Thermoresponsive poly(oligo ethylene glycol acrylates). *Progress in Polymer Science* **2014,** 39 (6), 1074-1095 DOI: http://dx.doi.org/10.1016/j.progpolymsci.2014.02.005.

55. Badi, N. Non-linear PEG-based thermoresponsive polymer systems. *Progress in Polymer Science* **2017,** 66, 54-79 DOI: 10.1016/j.progpolymsci.2016.12.006.

56. Jeong, B.; Kim, S. W.; Bae, Y. H. Thermosensitive sol–gel reversible hydrogels. *Adv Drug Deliver Rev* **2002,** 54 (1), 37-51 DOI: https://doi.org/10.1016/S0169-409X(01)00242-3.

57. Takeuchi, Y.; Tsujimoto, T.; Uyama, H. Thermogelation of amphiphilic poly(asparagine) derivatives. *Polym Advan Technol* **2011,** 22 (5), 620-626 DOI: 10.1002/pat.1555.

58. Watanabe, E.; Tomoshige, N.; Uyama, H. New biodegradable and thermoresponsive polymers based on amphiphilic poly(asparagine) derivatives. *Macromolecular Symposia* **2007,** 249, 509-514 DOI: 10.1002/masy.200750428.

59. Kocak, G.; Tuncer, C.; Butun, V. pH-Responsive polymers. *Polymer Chemistry* **2017,** 8 (1), 144-176 DOI: 10.1039/c6py01872f.

60. Hu, J.; Zhang, G.; Ge, Z.; Liu, S. Stimuli-responsive tertiary amine methacrylate-based block copolymers: Synthesis, supramolecular self-assembly and functional applications. *Progress in Polymer Science* **2014,** 39 (6), 1096-1143 DOI: https://doi.org/10.1016/j.progpolymsci.2013.10.006.

61. Karjalainen, E.; Aseyev, V.; Tenhu, H. Influence of Hydrophobic Anion on Solution Properties of PDMAEMA. *Macromolecules* **2014,** 47 (6), 2103-2111 DOI: 10.1021/ma5000706.

62. Plamper, F. A.; Schmalz, A.; Ballauff, M.; Muller, A. H. E. Tuning the thermoresponsiveness of weak polyelectrolytes by pH and light: Lower and upper critical-solution temperature of Poly(N,N-dimethylaminoethyl methacrylate). *J Am Chem Soc* **2007,** 129 (47), 14538-+ DOI: 10.1021/ja074720i.

63. Thavanesan, T.; Herbert, C.; Plamper, F. A. Insight in the Phase Separation Peculiarities of Poly(dialkylaminoethyl methacrylate)s. *Langmuir* **2014,** 30 (19), 5609-5619 DOI: 10.1021/la5007583.

64. Song, Z. F.; Wang, K.; Gao, C. Q.; Wang, S.; Zhang, W. Q. A New Thermo-, pH-, and CO2-Responsive Homopolymer of Poly N- 2-(diethylamino)ethyl acrylamide : Is the Diethylamino Group Underestimated? *Macromolecules* **2016,** 49 (1), 162-171 DOI: 10.1021/acs.macromol.5b02458.

65. Plamper, F. A.; Ruppel, M.; Schmalz, A.; Borisov, O.; Ballauff, M.; Muller, A. H. E. Tuning the thermoresponsive properties of weak polyelectrolytes: Aqueous solutions of star-shaped and linear Poly(N,N-dimethylaminoethyl methacrylate). *Macromolecules* **2007,** 40 (23), 8361-8366 DOI: 10.1021/ma071203bCCC$37.00.

66. Fournier, D.; Hoogenboom, R.; Thijs, H. M. L.; Paulus, R. M.; Schubert, U. S. Tunable pH- and temperature-sensitive copolymer libraries by reversible addition-fragmentation chain transfer copolymerizations of methacrylates. *Macromolecules* **2007,** 40 (4), 915-920 DOI: 10.1021/ma062199r.

67. Bates, F. S.; Fredrickson, G. H. Block Copolymer Thermodynamics - Theory and Experiment. *Annu Rev Phys Chem* **1990,** 41, 525-557 DOI: DOI 10.1146/annurev.pc.41.100190.002521.

68. Hadjichristidis, N.; Pitsikalis, M.; Iatrou, H., Synthesis of Block Copolymers. In *Block Copolymers I,* Abetz, V., Ed. Springer Berlin Heidelberg: Berlin, Heidelberg, 2005; pp 1-124.

69. Nikos Hadjichristidis, S. P., George Floudas, *Block Copolymers: Synthetic Strategies, Physical Properties, and Applications*. John Wiley & Sons, Inc.: New Jersey, 2003.

70. Feng, H. B.; Lu, X. Y.; Wang, W. Y.; Kang, N. G.; Mays, J. W. Block Copolymers: Synthesis, Self-Assembly, and Applications. *Polymers* **2017,** 9 (10), DOI: 10.3390/polym9100494.

71. Segalman, R. A. Patterning with block copolymer thin films. *Materials Science and Engineering: R: Reports* **2005,** 48 (6), 191-226 DOI: 10.1016/j.mser.2004.12.003.

72. Hamley, I. W., *The Physics of Block Copolymers, Oxford University Press*. Oxford University Press: New York, 1998.

73. Bates, F. S.; Fredrickson, G. H. Block copolymers - Designer soft materials. *Phys Today* **1999,** 52 (2), 32-38 DOI: Doi 10.1063/1.882522.

74. Matsen, M. W.; Bates, F. S. Unifying weak- and strong-segregation block copolymer theories. *Macromolecules* **1996,** 29 (4), 1091-1098 DOI: Doi 10.1021/Ma951138i.

75. Baker, R. W., Overview of Membrane Science and Technology. In *Membrane Technology and Applications*, Baker, R. W., Ed. John Wiley & Sons, Ltd: 2012.

76. Werber, J. R.; Osuji, C. O.; Elimelech, M. Materials for next-generation desalination and water purification membranes. *Nat Rev Mater* **2016,** 1 (5), DOI: 10.1038/natrevmats.2016.18.

77. Shannon, M. A.; Bohn, P. W.; Elimelech, M.; Georgiadis, J. G.; Marinas, B. J.; Mayes, A. M. Science and technology for water purification in the coming decades. *Nature* **2008,** 452 (7185), 301-310 DOI: 10.1038/nature06599.

78. Logan, B. E.; Elimelech, M. Membrane-based processes for sustainable power generation using water. *Nature* **2012,** 488 (7411), 313-319 DOI: 10.1038/nature11477.

79. Ulbricht, M. Membrane separations using molecularly imprinted polymers. *J Chromatogr B* **2004,** 804 (1), 113-125 DOI: 10.1016/j.jchromb.2004.02.007.

80. Li, J.; Chase, H. A. Applications of membrane techniques for purification of natural products. *Biotechnol Lett* **2010,** 32 (5), 601-608 DOI: 10.1007/s10529-009-0199-7.

81. Kawakami, H. Polymeric membrane materials for artificial organs. *Journal of Artificial Organs* **2008,** 11 (4), 177-181 DOI: 10.1007/s10047-008-0427-2.

82. Rezakizemi, M.; Sadrzadeh, M.; Matsuura, T. Thermally stable polymers for advanced high-performance gas separation membranes. *Progress in Energy and Combustion Science* **2018,** 66, 1-41 DOI: 10.1016/j.pecs.2017.11.002.

83. Rezakazemi, M.; Khajeh, A.; Mesbah, M. Membrane filtration of wastewater from gas and oil production. *Environmental Chemistry Letters* **2018,** 16 (2), 367-388 DOI: 10.1007/s10311-017-0693-4.

84. Madhura, L.; Kanchi, S.; Sabela, M. I.; Singh, S.; Bisetty, K.; Inamuddin. Membrane technology for water purification. *Environmental Chemistry Letters* **2018,** 16 (2), 343-365 DOI: 10.1007/s10311-017-0699-y.

85. de Jong, J.; Lammertink, R. G. H.; Wessling, M. Membranes and microfluidics: a review. *Lab Chip* **2006,** 6 (9), 1125-1139 DOI: 10.1039/b603275c.

86. Islam, M. R.; Lu, Z.; Li, X.; Sarker, A. K.; Hu, L.; Choi, P.; Li, X.; Hakobyan, N.; Serpe, M. J. Responsive polymers for analytical applications: A review. *Analytica Chimica Acta* **2013,** 789, 17-32 DOI: http://dx.doi.org/10.1016/j.aca.2013.05.009.

87. Liu, Z.; Wang, W.; Xie, R.; Ju, X. J.; Chu, L. Y. Stimuli-responsive smart gating membranes. *Chem Soc Rev* **2016,** 45 (3), 460-474 DOI: 10.1039/c5cs00692a.

88. Gokal, R.; Mallick, N. P. Peritoneal dialysis. *The Lancet* **1999,** 353 (9155), 823-828 DOI: https://doi.org/10.1016/S0140-6736(98)09410-0.

89. Tijing, L. D.; Woo, Y. C.; Choi, J.-S.; Lee, S.; Kim, S.-H.; Shon, H. K. Fouling and its control in membrane distillation—A review. *Journal of Membrane Science* **2015,** 475, 215-244 DOI: https://doi.org/10.1016/j.memsci.2014.09.042.

90. Ito, T.; Hioki, T.; Yamaguchi, T.; Shinbo, T.; Nakao, S.; Kimura, S. Development of a molecular recognition ion gating membrane and estimation of its pore size control. *J Am Chem Soc* **2002,** 124 (26), 7840-7846 DOI: 10.1021/ja012648x.

91. Adrus, N.; Ulbricht, M. Novel hydrogel pore-filled composite membranes with tunable and temperature-responsive size-selectivity. *J Mater Chem* **2012,** 22 (7), 3088-3098 DOI: 10.1039/c2jm15022k.

92. Frost, S.; Ulbricht, M. Thermoresponsive ultrafiltration membranes for the switchable permeation and fractionation of nanoparticles. *Journal of Membrane Science* **2013,** 448, 1-11 DOI: 10.1016/j.memsci.2013.07.036.

93. Wang, Z. G.; Yao, X. P.; Wang, Y. Swelling-induced mesoporous block copolymer membranes with intrinsically active surfaces for size-selective separation. *J Mater Chem* **2012,** 22 (38), 20542-20548 DOI: 10.1039/c2jm34292h.

94. Zhao, C. S.; Nie, S. Q.; Tang, M.; Sun, S. D. Polymeric pH-sensitive membranes-A review. *Progress in Polymer Science* **2011,** 36 (11), 1499-1520 DOI: 10.1016/j.progpolymsci.2011.05.004.

95. Brazel, C. S. Magnetothermally-responsive Nanomaterials: Combining Magnetic Nanostructures and Thermally-Sensitive Polymers for Triggered Drug Release. *Pharm Res-Dord* **2009,** 26 (3), 644-656 DOI: 10.1007/s11095-008-9773-2.

96. Hoare, T.; Timko, B. P.; Santamaria, J.; Goya, G. F.; Irusta, S.; Lau, S.; Stefanescu, C. F.; Lin, D. B.; Langer, R.; Kohane, D. S. Magnetically Triggered Nanocomposite Membranes: A Versatile Platform for Triggered Drug Release. *Nano Lett* **2011,** 11 (3), 1395-1400 DOI: 10.1021/nl200494t.

97. Timko, B. P.; Dvir, T.; Kohane, D. S. Remotely Triggerable Drug Delivery Systems. *Adv Mater* **2010,** 22 (44), 4925-4943 DOI: 10.1002/adma.201002072.

98. Satarkar, N. S.; Biswal, D.; Hilt, J. Z. Hydrogel nanocomposites: a review of applications as remote controlled biomaterials. *Soft Matter* **2010,** 6 (11), 2364-2371 DOI: 10.1039/b925218p.

99. Zhang, R. N.; Liu, Y. N.; He, M. R.; Su, Y. L.; Zhao, X. T.; Elimelech, M.; Jiang, Z. Y. Antifouling membranes for sustainable water purification: strategies and mechanisms. *Chem Soc Rev* **2016,** 45 (21), 5888-5924 DOI: 10.1039/c5cs00579e.

100. Kochkodan, V.; Hilal, N. A comprehensive review on surface modified polymer membranes for biofouling mitigation. *Desalination* **2015,** 356, 187-207 DOI: 10.1016/j.desal.2014.09.015.

101. Miller, D. J.; Dreyer, D. R.; Bielawski, C. W.; Paul, D. R.; Freeman, B. D. Surface Modification of Water Purification Membranes. *Angew Chem Int Edit* **2017,** 56 (17), 4662-4711 DOI: 10.1002/anie.201601509.

102. Yang, Q.; Adrus, N.; Tomicki, F.; Ulbricht, M. Composites of functional polymeric hydrogels and porous membranes. *J Mater Chem* **2011,** 21 (9), 2783-2811 DOI: 10.1039/c0jm02234a.

103. Ulbricht, M. Advanced functional polymer membranes. *Polymer* **2006,** 47 (7), 2217-2262 DOI: 10.1016/j.polymer.2006.01.084.

104. Park, Y. S.; Ito, Y.; Imanishi, Y. Permeation control through porous membranes immobilized with thermosensitive polymer. *Langmuir* **1998,** 14 (4), 910-914 DOI: DOI 10.1021/la970866r.

105. Tripathi, B. P.; Dubey, N. C.; Simon, F.; Stamm, M. Thermo responsive ultrafiltration membranes of grafted poly(N-isopropyl acrylamide) via polydopamine. *Rsc Advances* **2014,** 4 (64), 34073-34083 DOI: 10.1039/c4ra03485f.

106. Wu, C. J.; Xie, R.; Wei, H. B.; Xu, T. T.; Liu, Z.; Wang, W.; Ju, X. J.; Chu, L. Y. Fabrication of a thermo-responsive membrane with cross-linked smart gates via a 'grafting-to' method. *Rsc Advances* **2016,** 6 (51), 45428-45433 DOI: 10.1039/c6ra05192h.

107. Menne, D.; Pitsch, F.; Wong, J. E.; Pich, A.; Wessling, M. Temperature-Modulated Water Filtration Using Microgel-Functionalized Hollow-Fiber Membranes. *Angew Chem Int Edit* **2014,** 53 (22), 5706-5710 DOI: 10.1002/anie.201400316.

108. Hou, Z. Z.; Abbott, N. L.; Stroeve, P. Self-assembled monolayers on electroless gold impart pH-responsive transport of ions in porous membranes. *Langmuir* **2000,** 16 (5), 2401-2404 DOI: DOI 10.1021/la991045k.

109. Nishizawa, M.; Menon, V. P.; Martin, C. R. Metal Nanotubule Membranes with Electrochemically Switchable Ion-Transport Selectivity. *Science* **1995,** 268 (5211), 700-702 DOI: DOI 10.1126/science.268.5211.700.

110. Clodt, J. I.; Filiz, V.; Rangou, S.; Buhr, K.; Abetz, C.; Hoche, D.; Hahn, J.; Jung, A.; Abetz, V. Double Stimuli-Responsive Isoporous Membranes via Post-Modification of pH-Sensitive Self-Assembled Diblock Copolymer Membranes. *Adv Funct Mater* **2013,** 23 (6), 731-738 DOI: 10.1002/adfm.201202015.

111. Guo, H. F.; Ulbricht, M. Preparation of thermo-responsive polypropylene membranes via surface entrapment of poly(N-isopropylacrylamide)-containing macromolecules. *Journal of Membrane Science* **2011,** 372 (1-2), 331-339 DOI: 10.1016/j.memsci.2011.02.018.

112. Yu, S. F.; Lee, S. B.; Martin, C. R. Electrophoretic protein transport in gold nanotube membranes. *Anal Chem* **2003,** 75 (6), 1239-1244 DOI: 10.1021/ac020711a.

113. Clodt, J. I.; Filiz, V.; Rangou, S.; Buhr, K.; Abetz, C.; Hoche, D.; Hahn, J.; Jung, A.; Abetz, V. Double Stimuli-Responsive Isoporous Membranes via Post-Modifi cation of pH-Sensitive Self-Assembled Diblock Copolymer Membranes. *Adv Funct Mater* **2013,** 23 (6), 731-738 DOI: 10.1002/adfm.201202015.

114. Geismann, C.; Ulbricht, M. Photoreactive functionalization of poly(ethylene terephthalate) track-etched pore surfaces with "smart" polymer system's. *Macromolecular Chemistry and Physics* **2005,** 206 (2), 268-281 DOI: 10.1002/macp.200400374.

115. Geismann, C.; Yaroshchuk, A.; Ulbricht, M. Permeability and electrokinetic characterization of poly(ethylene terephthalate) capillary pore membranes with grafted temperature-responsive polymers. *Langmuir* **2007,** 23 (1), 76-83 DOI: 10.1021/la0603774.

116. Ito, Y.; Ochiai, Y.; Park, Y. S.; Imanishi, Y. pH-sensitive gating by conformational change of a polypeptide brush grafted onto a porous polymer membrane. *J Am Chem Soc* **1997,** 119 (7), 1619-1623 DOI: 10.1021/ja963418z.

117. Xie, R.; Chu, L. Y.; Chen, W. M.; Xiao, W.; Wang, H. D.; Qu, J. B. Characterization of microstructure of poly (N-isopropylacrylamide)-grafted polycarbonate track-etched membranes prepared by plasma-graft pore-filling polymerization. *Journal of Membrane Science* **2005,** 258 (1-2), 157-166 DOI: 10.1016/j.memsci.2005.03.012.

118. Alem, H.; Duwez, A. S.; Lussis, P.; Lipnik, P.; Jonas, A. M.; Demoustier-Champagne, S. Microstructure and thermo-responsive behavior of poly (N-isopropylacrylamide) brushes grafted in nanopores of track-etched membranes. *Journal of Membrane Science* **2008,** 308 (1-2), 75-86 DOI: 10.1016/j.memsci.2007.09.036.

119. Hesampour, M.; Huuhilo, T.; Mäkinen, K.; Mänttäri, M.; Nyström, M. Grafting of temperature sensitive PNIPAAm on hydrophilised polysulfone UF membranes. *Journal of Membrane Science* **2008,** 310 (1), 85-92 DOI: https://doi.org/10.1016/j.memsci.2007.10.038.

120. Himstedt, H. H.; Marshall, K. M.; Wickramasinghe, S. R. pH-responsive nanofiltration membranes by surface modification. *Journal of Membrane Science* **2011,** 366 (1), 373-381 DOI: https://doi.org/10.1016/j.memsci.2010.10.027.

121. He, D. M.; Susanto, H.; Ulbricht, M. Photo-irradiation for preparation, modification and stimulation of polymeric membranes. *Progress in Polymer Science* **2009,** 34 (1), 62-98 DOI: 10.1016/j.progpolymsci.2008.08.004.

122. Deng, J. P.; Wang, L. F.; Liu, L. Y.; Yang, W. T. Developments and new applications of UV-induced surface graft polymerizations. *Progress in Polymer Science* **2009,** 34 (2), 156-193 DOI: 10.1016/j.progpolymsci.2008.06.002.

123. Gajda, M.; Ulbricht, M. Capillary pore membranes with grafted diblock copolymers showing reversibly changing ultrafiltration properties with independent response to ions and temperature. *Journal of Membrane Science* **2016,** 514, 510-517 DOI: 10.1016/j.memsci.2016.05.001.

124. Salam, A.; Ulbricht, M. Effect of surface modification on the synthesis of pore-filling polymeric monoliths in microfiltration membranes made from poly(propylene) and poly(ethylene terephthalate). *Macromol Mater Eng* **2007,** 292 (3), 310-318 DOI: 10.1002/mame.200600411.

125. Xi Lin; Rong Huang; Ulbricht, M. Novel magneto-responsive membrane for remote control switchable molecular sieving. *Journal of Materials Chemistry B* **2016,** 4, 867-879.

126. Yoo, S. H.; Kim, J. H.; Jho, J. Y.; Won, J.; Kang, Y. S. Influence of the addition of PVP on the morphology of asymmetric polyimide phase inversion membranes: effect of PVP molecular weight. *Journal of Membrane Science* **2004,** 236 (1), 203-207 DOI: https://doi.org/10.1016/j.memsci.2004.02.017.

127. Peinemann, K. V.; Abetz, V.; Simon, P. F. W. Asymmetric superstructure formed in a block copolymer via phase separation. *Nat Mater* **2007,** 6 (12), 992-996 DOI: 10.1038/nmat2038.

128. Xu, F. J.; Li, J.; Yuan, S. J.; Zhang, Z. X.; Kang, E. T.; Neoh, K. G. Thermo-responsive porous membranes of controllable porous morphology from triblock copolymers of polycaprolactone and Poly(N-isopropylacrylamide) prepared by atom transfer radical polymerization. *Biomacromolecules* **2008,** 9 (1), 331-339 DOI: 10.1021/bm7008922.

129. Hoare, T.; Santamaria, J.; Goya, G. F.; Irusta, S.; Lin, D.; Lau, S.; Padera, R.; Langer, R.; Kohane, D. S. A Magnetically Triggered Composite Membrane for On-Demand Drug Delivery. *Nano Lett* **2009,** 9 (10), 3651-3657 DOI: 10.1021/nl9018935.

130. Schacher, F.; Ulbricht, M.; Muller, A. H. E. Self-Supporting, Double Stimuli-Responsive Porous Membranes From Polystyrene-block-poly (N,N-dimethylaminoethyl methacrylate) Diblock Copolymers. *Adv Funct Mater* **2009,** 19 (7), 1040-1045 DOI: 10.1002/adfm.200801457.

131. Susanto, H.; Ulbricht, M. Characteristics, performance and stability of polyethersulfone ultrafiltration membranes prepared by phase separation method using different macromolecular additives. *Journal of Membrane Science* **2009,** 327 (1-2), 125-135 DOI: 10.1016/j.memsci.2008.11.025.

132. Nunes, S. P.; Behzad, A. R.; Hooghan, B.; Sougrat, R.; Karunakaran, M.; Pradeep, N.; Vainio, U.; Peinemann, K. V. Switchable pH-Responsive Polymeric Membranes Prepared via Block Copolymer Micelle Assembly. *Acs Nano* **2011,** 5 (5), 3516-3522 DOI: 10.1021/nn200484v.

133. Qiu, X. Y.; Yu, H. Z.; Karunakaran, M.; Pradeep, N.; Nunes, S. P.; Peinemann, K. V. Selective Separation of Similarly Sized Proteins with Tunable Nanoporous Block Copolymer Membranes. *Acs Nano* **2013,** 7 (1), 768-776 DOI: 10.1021/nn305073e.

134. Luo, T.; Lin, S.; Xie, R.; Ju, X.-J.; Liu, Z.; Wang, W.; Mou, C.-L.; Zhao, C.; Chen, Q.; Chu, L.-Y. pH-responsive poly(ether sulfone) composite membranes blended with amphiphilic polystyrene-block-poly(acrylic acid) copolymers. *Journal of Membrane Science* **2014,** 450, 162-173 DOI: https://doi.org/10.1016/j.memsci.2013.09.002.

135. Luo, F.; Xie, R.; Liu, Z.; Ju, X. J.; Wang, W.; Lin, S.; Chu, L. Y. Smart gating membranes with in situ self-assembled responsive nanogels as functional gates. *Sci Rep-Uk* **2015,** 5, DOI: 10.1038/srep14708.

136. Lin, X.; Quoc, B. N.; Ulbricht, M. Magnetoresponsive Poly(ether sulfone)-Based Iron Oxide cum Hydrogel Mixed Matrix Composite Membranes for Switchable Molecular Sieving. *Acs Applied Materials & Interfaces* **2016,** 8 (42), 29001-29014 DOI: 10.1021/acsami.6b09369.

137. Cetintas, M.; de Grooth, J.; Hofman, A. H.; van der Kooij, H. M.; Loos, K.; de Vos, W. M.; Kamperman, M. Free-standing thermo-responsive nanoporous membranes from high molecular weight PS-PNIPAM block copolymers synthesized via RAFT polymerization. *Polymer Chemistry* **2017,** 8 (14), 2235-2243 DOI: 10.1039/c7py00023e.

138. Ma, B.; Ju, X. J.; Luo, F.; Liu, Y. Q.; Wang, Y.; Liu, Z.; Wang, W.; Xie, R.; Chu, L. Y. Facile Fabrication of Composite Membranes with Dual Thermo- and pH-Responsive Characteristics. *Acs Applied Materials & Interfaces* **2017,** 9 (16), 14409-14421 DOI: 10.1021/acsami.7b02427.

139. Miao, L.; Tu, Y. Y.; Yang, Y.; Lin, S. D.; Hu, J. W.; Zhang, M.; Li, Y.; Li, F.; Mo, Y. M. Robust Stimuli-Responsive Membranes Prepared from a Blend of Polysulfone and a Graft Copolymer Bearing Binary Side Chains with Thermo-and pH-Responsive Switching Behavior. *Chem-Eur J* **2017,** 23 (32), 7737-7747 DOI: 10.1002/chem.201605263.

140. Loeb, S.; Sourirajan, S., Sea Water Demineralization by Means of an Osmotic Membrane. In *Saline Water Conversion—II*, AMERICAN CHEMICAL SOCIETY: 1963; Vol. 38, pp 117-132.

141. Horenz, C.; Pietsch, C.; Goldmann, A. S.; Barner-Kowollik, C.; Schacher, F. H. Phase Inversion Membranes from Amphiphilic Diblock Terpolymers. *Advanced Materials Interfaces* **2015,** 2 (8), DOI: 10.1002/admi.201500042.

142. Guillen, G. R.; Pan, Y. J.; Li, M. H.; Hoek, E. M. V. Preparation and Characterization of Membranes Formed by Nonsolvent Induced Phase Separation: A Review. *Ind Eng Chem Res* **2011,** 50 (7), 3798-3817 DOI: 10.1021/ie101928r.

143. Mulder, J., *Basic Principles of Membrane Technology*. Springer Netherlands: 1996.

144. Fei, Z. D.; Wan, L. S.; Wang, W. M.; Zhong, M. Q.; Xu, Z. K. Thermo-responsive polyacrylonitrile membranes prepared with poly(acrylonitrile-g-isopropylacrylamide) as an additive. *Journal of Membrane Science* **2013,** 432, 42-49 DOI: 10.1016/j.memsci.2013.01.008.

145. Song, X. L.; Xie, R.; Luo, T.; Ju, X. J.; Wang, W.; Chu, L. Y. Ethanol-Responsive Characteristics of Polyethersulfone Composite Membranes Blended with Poly(N-isopropylacrylamide) Nanogels. *J Appl Polym Sci* **2014,** 131 (21), DOI: ARTN 41032

10.1002/app.41032.

146. Wang, Y.; Li, F. An emerging pore-making strategy: confined swelling-induced pore generation in block copolymer materials. *Advanced materials* **2011,** 23 (19), 2134-48 DOI: 10.1002/adma.201004022.

147. Wang, Y.; He, C. C.; Xing, W. H.; Li, F. B.; Tong, L.; Chen, Z. Q.; Liao, X. Z.; Steinhart, M. Nanoporous Metal Membranes with Bicontinuous Morphology from Recyclable Block-Copolymer Templates. *Adv Mater* **2010,** 22 (18), 2068-+ DOI: 10.1002/adma.200903655.

148. Z., R. Fabrication of Nanoporous Structures in Block Copolymer Using Selective Solvent Assisted with Compressed Carbon Dioxide. *Macromolecules* **2009,** 42, 3559-3564.

149. Keddie, D. J. A guide to the synthesis of block copolymers using reversible-addition fragmentation chain transfer (RAFT) polymerization. *Chem Soc Rev* **2014,** 43 (2), 496-505 DOI: 10.1039/c3cs60290g.

150. Moad, G. RAFT polymerization to form stimuli-responsive polymers. *Polymer Chemistry* **2017,** 8 (1), 177-219 DOI: 10.1039/c6py01849a.

151. Moad, G.; Rizzardo, E.; Thang, S. H. Living radical polymerization by the RAFT process. *Australian Journal of Chemistry* **2005,** 58 (6), 379-410 DOI: 10.1071/ch05072.

152. Moad, G.; Rizzardo, E.; Thang, S. H. Living Radical Polymerization by the RAFT Process - A Third Update. *Australian Journal of Chemistry* **2012,** 65 (8), 985-1076 DOI: 10.1071/ch12295.

153. Keddie, D. J.; Moad, G.; Rizzardo, E.; Thang, S. H. RAFT Agent Design and Synthesis. *Macromolecules* **2012,** 45 (13), 5321-5342 DOI: 10.1021/ma300410v.

154. Foster, J. C.; Radzinski, S. C.; Matson, J. B. Graft Polymer Synthesis by RAFT Transfer-To. *J Polym Sci Pol Chem* **2017,** 55 (18), 2865-2876 DOI: 10.1002/pola.28621.

155. York, A. W.; Kirkland, S. E.; McCormick, C. L. Advances in the synthesis of amphiphilic block copolymers via RAFT polymerization: Stimuli-responsive drug and gene delivery. *Adv Drug Deliver Rev* **2008,** 60 (9), 1018-1036 DOI: 10.1016/j.addr.2008.02.006.

156. Chong, Y. K.; Le, T. P. T.; Moad, G.; Rizzardo, E.; Thang, S. H. A more versatile route to block copolymers and other polymers of complex architecture by living radical polymerization: The RAFT process. *Macromolecules* **1999,** 32 (6), 2071-2074 DOI: 10.1021/ma981472p.

157. Heide, P. v. d., *X-Ray Photoelectron Spectroscopy: An Introduction to Principles and Practices*. John Wiley & Sons: Hoboken, N.J., 2012.

158. Hofmann, S., *Auger- and X-ray photoelectron spectroscopy in materials science : a user-oriented guide*. Springer: Berlin, 2013.

159. Einstein, A. The motion of elements suspended in static liquids as claimed in the molecular kinetic theory of heat. *Annalen Der Physik* **1905,** 17 (8), 549-560.

160. *Handbook of X-ray Photoelectron Spectroscopy*.

161. Zhao, C.; Nie, S.; Tang, M.; Sun, S. Polymeric pH-sensitive membranes—A review. *Progress in Polymer Science* **2011,** 36 (11), 1499-1520 DOI: 10.1016/j.progpolymsci.2011.05.004.

162. Chu, L. Y.; Xie, R.; Ju, X. J. Stimuli-responsive Membranes: Smart Tools for Controllable Mass-transfer and Separation Processes. *Chinese Journal of Chemical Engineering* **2011,** 19 (6), 891-903.

163. Choi, Y. J.; Yamaguchi, T.; Nakao, S. A novel separation system using porous thermosensitive membranes. *Ind Eng Chem Res* **2000,** 39 (7), 2491-2495 DOI: DOI 10.1021/ie9907627.

164. Vertommen, M. A. M. E.; Cornelissen, H. J. L.; Dietz, C. H. J. T.; Hoogenboom, R.; Kemmere, M. F.; Keurentjes, J. T. F. Pore-covered thermoresponsive membranes for repeated on-demand drug release. *Journal of Membrane Science* **2008,** 322 (1), 243-248 DOI: 10.1016/j.memsci.2008.05.044.

165. Wang, W. C.; Tian, X. D.; Feng, Y. P.; Cao, B.; Yang, W. T.; Zhang, L. Q. Thermally On-Off Switching Membranes Prepared by Pore-Filling Poly(N-isopropylacrylamide) Hydrogels. *Ind Eng Chem Res* **2010,** 49 (4), 1684-1690 DOI: 10.1021/ie9008666.

166. Xie, R.; Li, Y.; Chu, L. Y. Preparation of thermo-responsive gating membranes with controllable response temperature. *Journal of Membrane Science* **2007,** 289 (1-2), 76-85 DOI: 10.1016/j.memsci.2006.11.040.

167. Gamys, C. G.; Schumers, J. M.; Mugemana, C.; Fustin, C. A.; Gohy, J. F. Pore-functionalized nanoporous materials derived from block copolymers. *Macromolecular rapid communications* **2013,** 34 (12), 962-82 DOI: 10.1002/marc.201300214.

168. Yokoyama, H.; Li, L.; Nemoto, T.; Sugiyama, K. Tunable nanocellular polymeric monoliths using fluorinated block copolymer templates and supercritical carbon dioxide. *Adv Mater* **2004,** 16 (17), 1542-+ DOI: 10.1002/adma.200400072.

169. Li, L.; Yokoyama, H.; Nemoto, T.; Sugiyama, K. Facile fabrication of nanocellular block copolymer thin films using supercritical carbon dioxide. *Adv Mater* **2004,** 16 (14), 1226-+ DOI: 10.1002/adma.200400264.

170. Yokoyama, H.; Sugiyama, K. Nanocellular structures in block copolymers with CO2-philic blocks using CO2 as a blowing agent: Crossover from micro- to nanocellular structures with depressurization temperature. *Macromolecules* **2005,** 38 (25), 10516-10522 DOI: 10.1021/ma051757j.

171. Li, L.; Yokoyama, H. Nanoscale silica capsules ordered on a substrate: Oxidation of nanocellular thin films of poly(styrene-b-dimethylsiloxane). *Angew Chem Int Edit* **2006,** 45 (38), 6338-6341 DOI: 10.1002/anie.200602274.

172. Li, L.; Nemoto, T.; Sugiyama, K.; Yokoyama, H. CO2 foaming in thin films of block copolymer containing fluorinated blocks. *Macromolecules* **2006,** 39 (14), 4746-4755 DOI: 10.1021/ma060325l.

173. Yokoyama, H.; Li, L.; Dutriez, C.; Iwakura, Y.; Sugiyama, K.; Masunaga, H.; Sasaki, S.; Okuda, H. Horizontally and Vertically Aligned Polymeric Nanosheets: CO2-Induced Morphological Changes of Block Copolymer Thin Films. *Macromolecules* **2008,** 41 (22), 8626-8631 DOI: 10.1021/ma801487a.

174. Zhang, R.; Dutriez, C.; Sugiyama, K.; Ishizone, T.; Yokoyama, H. Thermally robust nanocellular thin films of high-T-g semifluorinated block copolymers foamed with supercritical carbon dioxide. *Soft Matter* **2011,** 7 (8), 4032-4038 DOI: 10.1039/c0sm00736f.

175. Dutriez, C.; Satoh, K.; Kamigaito, M.; Yokoyama, H. Nanocellular foaming of fluorine containing block copolymers in carbon dioxide: the role of glass transition in carbon dioxide. *Rsc Advances* **2012,** 2 (7), 2821-2827 DOI: 10.1039/c2ra01268e.

176. Shinkai, T.; Ito, M.; Sugiyama, K.; Ito, K.; Yokoyama, H. Ordered and foam structures of semifluorinated block copolymers in supercritical carbon dioxide. *Soft Matter* **2012,** 8 (21), 5811-5817 DOI: 10.1039/c2sm07085e.

177. Dutriez, C.; Satoh, K.; Kamigaito, M.; Yokoyama, H. Cross-linked nanocellular polymer films: water- and oil-repellent anti-reflection coating. *Polym J* **2016,** 48 (4), 497-501 DOI: 10.1038/pj.2016.7.

178. Zhang, R.; Yokoyama, H. Fabrication of Nanoporous Structures in Block Copolymer Using Selective Solvent Assisted with Compressed Carbon Dioxide. *Macromolecules* **2009,** 42 (10), 3559-3564 DOI: 10.1021/ma900123e.

179. Lequieu, W.; Shtanko, N. I.; Du Prez, F. E. Track etched membranes with thermo-adjustable porosity and separation properties by surface immobilization of poly(N-vinylcaprolactam). *Journal of Membrane Science* **2005,** 256 (1-2), 64-71 DOI: 10.1016/j.memsci.2005.02.007.

180. Schock, G.; Miquel, A.; Birkenberger, R. Characterization of Ultrafiltration Membranes - Cutoffs Determination by Gel-Permeation Chromatography. *Journal of Membrane Science* **1989,** 41, 55-67 DOI: Doi 10.1016/S0376-7388(00)82391-1.

181. Bakhshayeshi, M.; Kanani, D. M.; Mehta, A.; van Reis, R.; Kuriyel, R.; Jackson, N.; Zydney, A. L. Dextran sieving test for characterization of virus filtration membranes. *Journal of Membrane Science* **2011,** 379 (1-2), 239-248 DOI: 10.1016/j.memsci.2011.05.067.

182. Nobrega, R.; Debalmann, H.; Aimar, P.; Sanchez, V. Transfer of Dextran through Ultrafiltration Membranes - a Study of Rejection Data Analyzed by Gel-Permeation Chromatography. *Journal of Membrane Science* **1989,** 45 (1-2), 17-36 DOI: Doi 10.1016/S0376-7388(00)80842-X.

183. Wang, Y.; He, C.; Xing, W.; Li, F.; Tong, L.; Chen, Z.; Liao, X.; Steinhart, M. Nanoporous metal membranes with bicontinuous morphology from recyclable block-copolymer templates. *Advanced materials* **2010,** 22 (18), 2068-72 DOI: 10.1002/adma.200903655.

184. Gong, J. L.; Zhang, A. J.; Bai, H.; Zhang, Q. K.; Du, C.; Li, L.; Hong, Y. Z.; Li, J. Formation of nanoscale networks: selectively swelling amphiphilic block copolymers with CO2-expanded liquids. *Nanoscale* **2013,** 5 (3), 1195-1204 DOI: 10.1039/c2nr33188h.

185. Lee, Y. M.; Shim, J. K. Preparation of pH/temperature responsive polymer membrane by plasma polymerization and its riboflavin permeation. *Polymer* **1997,** 38 (5), 1227-1232 DOI: Doi 10.1016/S0032-3861(96)00548-4.

186. Shtanko, N. I.; Kabanov, V. Y.; Apel, P. Y.; Yoshida, M. The use of radiation-induced graft polymerization for modification of polymer track membranes. *Nuclear Instruments and Methods in Physics Research Section B: Beam Interactions with Materials and Atoms* **1999,** 151 (1–4), 416-422 DOI: http://dx.doi.org/10.1016/S0168-583X(99)00108-1.

187. Yang, B.; Yang, W. Thermo-sensitive switching membranes regulated by pore-covering polymer brushes. *Journal of Membrane Science* **2003,** 218 (1–2), 247-255 DOI: http://dx.doi.org/10.1016/S0376-7388(03)00182-0.

188. Johnson, S. R.; Evans, S. D.; Mahon, S. W.; Ulman, A. Alkanethiol molecules containing an aromatic moiety self-assembled onto gold clusters. *Langmuir* **1997,** 13 (1), 51-57 DOI: Doi 10.1021/La9607520.

189. Zydney, A. L.; Xenopoulos, A. Improving dextran tests for ultrafiltration membranes: Effect of device format. *Journal of Membrane Science* **2007,** 291 (1-2), 180-190 DOI: DOI 10.1016/j.memsci.2007.01.006.

190. Granath, K. A. Solution properties of branched dextrans. *Journal of Colloid Science* **1958,** 13 (4), 308-328.

191. Satarkar, N. S.; Hilt, J. Z. Magnetic hydrogel nanocomposites for remote controlled pulsatile drug release. *Journal of Controlled Release* **2008,** 130 (3), 246-251 DOI: http://dx.doi.org/10.1016/j.jconrel.2008.06.008.

192. Gebreyohannes, A. Y.; Bilad, M. R.; Verbiest, T.; Courtin, C. M.; Dornez, E.; Giorno, L.; Curcio, E.; Vankelecom, I. F. J. Nanoscale tuning of enzyme localization for enhanced reactor performance in a novel magnetic-responsive biocatalytic membrane reactor. *Journal of Membrane Science* **2015,** 487, 209-220 DOI: http://dx.doi.org/10.1016/j.memsci.2015.03.069.

193. Himstedt, H. H.; Yang, Q.; Qian, X. H.; Wickramasinghe, S. R.; Ulbricht, M. Toward remote-controlled valve functions via magnetically responsive capillary pore membranes. *Journal of Membrane Science* **2012,** 423, 257-266 DOI: 10.1016/j.memsci.2012.08.015.

194. Himstedt, H. H.; Yang, Q.; Dasi, L. P.; Qian, X. H.; Wickramasinghe, S. R.; Ulbricht, M. Magnetically Activated Micromixers for Separation Membranes. *Langmuir* **2011,** 27 (9), 5574-5581 DOI: 10.1021/la200223g.

195. Gajda, A. M.; Ulbricht, M. Magnetic Fe3O4 nanoparticle heaters in smart porous membrane valves. *Journal of Materials Chemistry B* **2014,** 2 (10), 1317-1326 DOI: 10.1039/c3tb21400a.

196. Qian, X. H.; Yang, Q.; Vu, A.; Wickramasinghe, S. R. Localized Heat Generation from Magnetically Responsive Membranes. *Ind Eng Chem Res* **2016,** 55 (33), 9015-9027 DOI: 10.1021/acs.iecr.6b01820.

197. Lin, X. Novel magneto-responsive ultrafiltration membranes for switchable molecular-sieving. PhD thesis, University of Duisburg-Essen, 2016.

198. Gonzales-Weimuller, M.; Zeisberger, M.; Krishnan, K. M. Size-dependant heating rates of iron oxide nanoparticles for magnetic fluid hyperthermia. *Journal of Magnetism and Magnetic Materials* **2009,** 321 (13), 1947-1950 DOI: http://doi.org/10.1016/j.jmmm.2008.12.017.

199. Hergt, R.; Dutz, S.; Muller, R.; Zeisberger, M. Magnetic particle hyperthermia: nanoparticle magnetism and materials development for cancer therapy. *J Phys-Condens Mat* **2006,** 18 (38), S2919-S2934 DOI: 10.1088/0953-8984/18/38/S26.

200. Friebe, A.; Ulbricht, M. Cylindrical Pores Responding to Two Different Stimuli via Surface-Initiated Atom Transfer Radical Polymerization for Synthesis of Grafted Diblock Copolymers. *Macromolecules* **2009,** 42 (6), 1838-1848 DOI: 10.1021/ma802185d.

201. Zhang, Z. B.; Zhu, X. L.; Xu, F. J.; Neoh, K. G.; Kang, E. T. Temperature- and pH-sensitive nylon membranes prepared via consecutive surface-initiated atom transfer radical graft polymerizations. *Journal of Membrane Science* **2009,** 342 (1–2), 300-306 DOI: http://dx.doi.org/10.1016/j.memsci.2009.07.004.

202. Pan, K.; Zhang, X.; Ren, R.; Cao, B. Double stimuli-responsive membranes grafted with block copolymer by ATRP method. *Journal of Membrane Science* **2010,** 356 (1–2), 133-137 DOI: https://doi.org/10.1016/j.memsci.2010.03.044.

203. Choi, J. Y.; Yun, T.; Kwak, S. Y. Two-step thermoresponsive membrane with tunable separation properties and improved cleaning efficiency. *Journal of Membrane Science* **2018,** 554, 117-124 DOI: 10.1016/j.memsci.2018.02.060.

204. Yokoyama, H.; Miyamae, T.; Han, S.; Ishizone, T.; Tanaka, K.; Takahara, A.; Torikai, N. Spontaneously formed hydrophilic surfaces by segregation of block copolymers with water-soluble blocks. *Macromolecules* **2005,** 38 (12), 5180-5189 DOI: 10.1021/ma050473w.

205. Oyane, A.; Ishizone, T.; Uchida, M.; Furukawa, K.; Ushida, T.; Yokoyama, H. Spontaneous formation of blood-compatible surfaces on hydrophobic polymers: Surface enrichment of a block copolymer with a water-soluble block. *Adv Mater* **2005,** 17 (19), 2329-+ DOI: 10.1002/adma.200500945.

206. Higaki, Y.; Inutsuka, Y.; Sakamak, T.; Terayama, Y.; Takenaka, A.; Higaki, K.; Yamada, N. L.; Moriwaki, T.; Ikemoto, Y.; Takahara, A. Effect of Charged Group Spacer Length on Hydration State in Zwitterionic Poly(sulfobetaine) Brushes. *Langmuir* **2017,** 33 (34), 8404-8412 DOI: 10.1021/acs.langmuir.7b01935.

207. Nelson, A. Co-refinement of multiple-contrast neutron/X-ray reflectivity data using MOTOFIT. *Journal of Applied Crystallography* **2006,** 39, 273-276 DOI: 10.1107/s0021889806005073.

208. Kienzle, P., Neutron activation and scattering calculator. NIST: https://www.ncnr.nist.gov/resources/activation/, 2018.

209. Bütün, V.; Armes, S. P.; Billingham, N. C. Synthesis and aqueous solution properties of near-monodisperse tertiary amine methacrylate homopolymers and diblock copolymers. *Polymer* **2001,** 42 (14), 5993-6008 DOI: https://doi.org/10.1016/S0032-3861(01)00066-0.

210. Pietsch, C.; Mansfeld, U.; Guerrero-Sanchez, C.; Hoeppener, S.; Vollrath, A.; Wagner, M.; Hoogenboom, R.; Saubern, S.; Thang, S. H.; Becer, C. R.; Chiefari, J.; Schubert, U. S. Thermo-Induced Self-Assembly of Responsive Poly(DMAEMA-b-DEGMA) Block Copolymers into Multi- and Unilamellar Vesicles. *Macromolecules* **2012,** 45 (23), 9292-9302 DOI: 10.1021/ma301867h.

211. Wagner, M.; Pietsch, C.; Kerth, A.; Traeger, A.; Schubert, U. S. Physicochemical Characterization of the Thermo-Induced Self-Assembly of Thermo-Responsive PDMAEMA-b-PDEGMA Copolymers. *J Polym Sci Pol Chem* **2015,** 53 (7), 924-935 DOI: 10.1002/pola.27520.

212. Yokoyama, H.; Tanaka, K.; Takahara, A.; Kajiyama, T.; Sugiyama, K.; Hirao, A. Surface structure of asymmetric fluorinated block copolymers. *Macromolecules* **2004,** 37 (3), 939-945 DOI: 10.1021/ma035191f.

213. Ashley, J. C. Simple model for electron inelastic mean free paths: Application to condensed organic materials. *Journal of Electron Spectroscopy and Related Phenomena* **1982,** 28 (2), 177-194 DOI: https://doi.org/10.1016/0368-2048(82)85041-X.

214. Gao, X.; Kucerka, N.; Nieh, M. P.; Katsaras, J.; Zhu, S. P.; Brash, J. L.; Sheardown, H. Chain Conformation of a New Class of PEG-Based Thermoresponsive Polymer Brushes Grafted on Silicon as Determined by Neutron Reflectometry. *Langmuir* **2009,** 25 (17), 10271-10278 DOI: 10.1021/la901086e.

215. Reinhardt, M. Functional interfaces. Humboldt-Universität zu Berlin, Mathematisch-Naturwissenschaftliche Fakultät I, 2014.

216. Murdoch, T. J.; Humphreys, B. A.; Willott, J. D.; Gregory, K. P.; Prescott, S. W.; Nelson, A.; Wanless, E. J.; Webber, G. B. Specific Anion Effects on the Internal Structure of a Poly(N-isopropylacrylamide) Brush. *Macromolecules* **2016,** 49 (16), 6050-6060 DOI: 10.1021/acs.macromol.6b01001.

217. Elliott, L. C. C.; Jing, B. X.; Akgun, B.; Zhu, Y. X.; Bohn, P. W.; Fullerton-Shirey, S. K. Loading and Distribution of a Model Small Molecule Drug in Poly(N-isopropylacrylamide) Brushes: a Neutron Reflectometry and AFM Study. *Langmuir* **2013,** 29 (10), 3259-3268 DOI: 10.1021/la305088k.

218. Yim, H.; Kent, M. S.; Satija, S.; Mendez, S.; Balamurugan, S. S.; Balamurugan, S.; Lopez, G. P. Evidence for vertical phase separation in densely grafted, high-molecular-weight poly(N-isopropylacrylamide) brushes in water. *Physical Review E* **2005,** 72 (5), DOI: 10.1103/PhysRevE.72.051801.

219. Troll, K.; Kulkarni, A.; Wang, W.; Darko, C.; Koumba, A. M. B.; Laschewsky, A.; Muller-Buschbaum, P.; Papadakis, C. M. The collapse transition of poly(styrene-b-(N-isopropyl acrylamide)) diblock copolymers in aqueous solution and in thin films. *Colloid and Polymer Science* **2008,** 286 (8-9), 1079-1092 DOI: 10.1007/s00396-008-1871-5.

220. Kureha, T.; Aoki, D.; Hiroshige, S.; Iijima, K.; Aoki, D.; Takata, T.; Suzuki, D. Decoupled Thermo- and pH-Responsive Hydrogel Microspheres Cross-Linked by Rotaxane Networks. *Angew Chem Int Edit* **2017,** 56 (48), 15393-15396 DOI: 10.1002/anie.201709633.